Waves in granular media : from microscopic scale to macroscopic scale.

Kamil Chrząszcz

NNT : 2016SACLC064

THESE DE DOCTORAT
DE
L'UNIVERSITE PARIS-SACLAY
PREPAREE A
CENTRALE SUPELEC

ÉCOLE DOCTORALE N° 579
SCIENCES MECANIQUES ET ENERGETIQUES, MATERIAUX ET GEOSCIENCES - SMEMAG

Spécialité de doctorat : Acoustique

Par

M. Kamil CHRZĄSZCZ

Ondes dans les milieux granulaires : de l'échelle microscopique à l'échelle macroscopique

Thèse présentée et soutenue à Saint Ouen, le 15 septembre 2016 :

Composition du Jury :

M. Olivier DOARÉ	Professeur des universités	Président
M. Nicolas DAUCHEZ	Professeur des universités	Rapporteur
M. Xavier NOBLIN	Chargé de recherche	Rapporteur
M. Noureddine BOUHADDI	Professeur des universités	Examinateur
M. Georgios THEOCHARIS	Chargé de recherche	Examinateur
M. Imad TAWFIQ	Professeur des universités	Directeur de thèse
M. Stéphane JOB	Maître de conférences	Encadrant de thèse

Contents

List of Figures

List of symbols

ρ	Density [kg.m^{-3}]
M	Mass of a sphere [kg]
g	Gravity [m.s^{-2}]
d	Diameter of a sphere [m]
k_B	Boltzmann constant [J.K^{-1}]
T	Temperature [K]
A_h	Hamaker coefficient [J]
r_{0A}	Distance between molecules [m]
U_{el}	Elastic energy [J]
k_H	Hertz contact stiffness [N.m^{-1}]
δ_0	Overlap deformation [m]
R_0, R_1, R_2	Radius of a sphere [m]
R	Effective radius between two spheres [m]
a	Radius of a contact disc [m]
F_0	Static force [N]
E_0, E_1, E_2	Young's modulus of a sphere [Pa]
E	Effective Young's modulus between two spheres [Pa]
ν_0, ν_1, ν_2	Poisson's ratio
σ	Stress [N.m^{-2}]
ε	Strain
u_z	Displacement [m]
r	Radial coordinate [m]
p, p_0, p_1	Pressure [Pa]
σ_Y	Yield Stress: onset of a plasticity [Pa]
F_Y	Maximal static force at yield [N]
μ_s	Coulomb's friction coefficient
δ_y	Tangential deformation [m]
F_t	Tangential force [N]
$k_t,\ k_0$	Tangential stiffness [N.m^{-1}]
G_0, G_1, G_2	Shear modulus of a sphere [Pa]
ρ_c, ρ_s	Density of a cylindrical supports [kg.m^{-3}]
E_c, E_s	Young's modulus of a cylindrical support [Pa]

R_c, R_s	Radius of a cylindrical support [m]
ν_c, ν_s	Poisson's ratio of a cylindrical support
G_c, G_s	Shear modulus of a cylindrical support [Pa]
G_r	Effective shear modulus between a sphere and a cylinder [Pa]
E_r	Effective Young's modulus between a sphere and a cylinder [Pa]
R_r	Effective radius between a sphere and a cylinder [m]
L	Length [m]
U_{surf}	Surface energy [J]
A	Surface area [m^2]
γ_s	Surface tension of a solid [$N.m^{-1}$]
F_{adh}	Force of a adhesion [N]
U_{tot}	Total energy [J]
F_{adh}^{DMT}	DMT's force of adhesion [N]
F_{adh}^{JKR}	JKR's force of adhesion [N]
γ_f	Surface tension of a fluid [$N.m^{-1}$]
Δp	Laplace pressure [Pa]
r_0	Radius of a curvature of a capillary bridge [m]
F_{cap}	Capillary force [N]
μ	Fluid's viscosity [Pa.s]
V_{in}	Initial velocity [$m.s^{-1}$]
V_{out}	Rebound velocity [$m.s^{-1}$]
e	Restitution coefficient
St	Stokes number
St_c	Critical Stokes number
h_0, h, D	Fluid's thickness [m]
$\dot{h}, v_z$	Fluid's axial velocity [$m.s^{-1}$]
v_r	Fluid's radial velocity [$m.s^{-1}$]
a_w	Typical extent of fluid's hydrodynamic field [m]
S_w	Typical area of a wet contact [m^2]
$\dot{\gamma}_s$	Shear rate [s^{-1}]
τ	Shear stress [Pa]
$\kappa_w, k_w, Z_\omega(D)$	Mechanical impedance [$N.m^{-1}$]
h_{0A}	Amplitude of a sphere oscillation [m]
f	Frequency [Hz]
ω	Angular frequency [$rad.s^{-1}$]
u	Deflection [m]
D_c	Critical distance [m]
k	Stiffness [$N.m^{-1}$]
λ	Damping [$N.m^{-1}.s^{-1}$]
$\Re$	Real part
$\Im$	Imaginary part
y_n	Relative displacement [m]

ω_{cut}	Angular cutoff frequency [rad.s^{-1}]
q, q_{th}, q_w, q_d, q_0	Wave number [rad.m^{-1}]
$\lambda, \lambda_d, \lambda_w$	Wave length [m]
c_g, c_Φ	Group and phase velocity [m.s^{-1}]
c_d, c_w	Dry and wet wave velocity [m.s^{-1}]
c, c_0	Wave speed [m.s^{-1}]
l_a	Attenuation length [m]
P	Confinement pressure [Pa]
F_m	Amplitude of a dynamic force [N]
V_p	EMT's longitudinal wave speed [m.s^{-1}]
V_s	EMT's shear wave speed [m.s^{-1}]
K_e, K_{ew}	EMT's Effective bulk modulus [Pa]
μ_e, μ_{ew}	EMT's Effective shear modulus [Pa]
ρ_e	EMT's Effective density [kg.m^{-3}]
ϕ	Volume fraction
Z	Coordination number
e	Thickness of a sample [m]
u_{in}	Reference signal [V]
u_{out}	Signal measured with sample [V]
ω_c	Angular central frequency [rad.s^{-1}]
H, H_{th}	Transfer function
Φ	Phase of a transfer function [rad]
c_L	Longitudinal wave speed [m.s^{-1}]
c_S	Shear wave speed [m.s^{-1}]
δ	Loss angle [rad]
u_n	Displacement [m]
C_i	Fourier transform of an input signal
C_0	Fourier transform of an output signal
C_i^*	Complex conjugate of a C_i
C_0^*	Complex conjugate of a C_0
C_{ii}, C_{00}	Auto-correlation of C_i and C_0
C_{i0}	Cross-correlation between C_0 and C_i
coh	Coherence between input and output signal
F_r	Radial component of a static force [N]
U_p	Potential energy [J]
U_k	Kinetic energy [J]
$\lvert\widetilde{F}(n)\rvert$	Amplitude of a dynamic perturbations [N]
l_f	Attenuation length due to a friction [m]
$F_{in}, F(x=0,t)$	Input force [N]
$F_{out}, F(x=L,t)$	Output force [N]
t, t_0	time [s]
γ	Acceleration [m.s^{-2}]

z_b	Displacement [m]
I	Second moment of a inertia [m^4]
q_b	Wave number of a bending mode [$rad.m^{-1}$]
c_b	Wave speed of a bending mode [$m.s^{-1}$]
ω_n	Resonance angular frequency [$rad.s^{-1}$]
γ_r	Radial acceleration of a support [$m.s^{-2}$]
ω_0	Low cutoff angular frequency [$rad.^{-1}$]
f_{min}	Minimal frequency [Hz]
f_{max}	Maximal frequency [Hz]
F_y	Component in y-axis of a static force [N]
Δ	Clearance [m]
η, η_d, η_w	Loss factor
τ_a	Relaxation time [s]
η_f	Loss factor due to friction
$F_{pulse}(x,t)$	Wave packet
F_{pulse}^{env}	Envelope of a wave packet
FT_t	Fourier transform over time
FT_x	Fourier transform over space
FT_{xt}	Fourier transform over space and time
τ_g	Group delay [s]
$H(x,\omega)$	Transfer function measured as a function of space and angular frequency
$K(\Re(q),\omega)$	Dispersion relation
a_d	Typical extent of a dry contact [m]
κ_t	Mechanical impedance [$N.m^{-1}$]
V_p	Theoretical wave speed in dry case [$m.s^{-1}$]
V_w	Theoretical wave speed in wet case [$m.s^{-1}$]
σ_T	Scattering cross section [m^2]
n	Number of a scatterers
l_s, l_s^{th}	Attenuation length due to scattering [m]
l_H, l_H^{th}	Attenuation length in the dry case [m]
l_{EHD}, l_{EHD}^{th}	Attenuation length in the wet case [m]
l_d, l_d^{th}	Total attenuation length in the dry case [m]
l_w, l_w^{th}	Total attenuation length in the wet case [m]
D_s	Diameter of a sphere [m]
R_c	Radius of a container [m]
φ	Volume fraction

Chapter 1

Context and content of the manuscript

Context and summary

Granular materials such as the sand, for instance, are intriguing by nature: they can behave as solids when the particles are under compression or as liquids or gases when they flow or when submitted to external vibrations [1, 2]. The acoustic waves which propagates via the contact networks between grains, along force chains, can serve to probe non-intrusively these materials [3–6]. In contrast with continuous media, in which the wave speed depends on the intrinsic elasticity and the density of the material, the wave speed in granular media depends on the contact stiffness between particles, on their mass, on the number of contact per grain (the coordination number), on their compacity and on the static compression applied on the sample [7–9]. In wet sand, for instance when a fluid settles in between grains thanks to capillary forces, the acoustic properties (wave speed, attenuation) can be dramatically and non-trivially affected. The effect of an interstitial fluid has been shown in experiment concerning wave propagation in the dry and wet granular media [10], where the authors observed two antagonist effects. On one hand, by considering fluids with different surface tensions but same viscosity, it was observed a decrease of the wave speed in respect to the dry case. This observation was related to a decrease of the coordination number. On the other hand, considering fluids with same surface tension but different viscosities allowed to evidence an increase of the wave speed, attributed to an increase of the contact stiffness related to an increase of the contact area between rough particles, when lubrication occurs. One possible strategy to dissociate both these effects consists in considering a granular medium whose coordination number is known and constant [11]: this is the case for one-dimensional (1D) granular media, in which each particle is in contact with two neighbors. This is the approach which we adopted in this work: we consider alignments of spherical particles, as the analogs of the force chains in three-dimensional (3D) granular media, in order to

focus our attention on the dynamics of the interaction between the interstitial fluid and the particles.

Since a decade, the 1D granular media bring the attention of many research groups [12–24] due to very rich nonlinear features and a broad range of potential applications they allow one to envisage. Motivated by these facts, we examine in this thesis, the details of the dynamics of dry and wet alignments of particles. On purpose, we first probe the reference case of dry chains of particles. Here we observe that the elasto-frictional coupling between the grains and a substrate (the supports on which stand the particles) induces an on-site potential, which in turn, induces a zero frequency band gap: the transmission of low frequency vibrations is impeded. Next, we probe the propagation of waves in wet granular chains. In this case, we show that an elastohydrodynamic model combined with Hertz potential accurately describes all our experimental observations. Finally, we extrapolate these observations to 3D granular packing. We here show that the effective medium theory combined with an elastohydrodynamic description fairly reproduces the features of the transmitted waves. Our experimental findings likely contribute to a better understanding of wave propagation in real wet granular media. In the following, we present a detailed summary of the PhD thesis.

In the chapter two, we present the main characteristics and the different mechanisms at play in granular media. In particular, we focus specifically on the description of dry and wet contact dynamics. Then, we expose some preliminary experimental observations concerning the propagation of waves in dry and wet granular media. At the end of the chapter, we detail the challenges of an accurate description of wave propagation in wet granular media.

In the chapter three, we perform a detailed experimental study on dry granular chains. Firstly, from ultrasonic experiments, we measure the intrinsic bulk characteristic of our spheres (Young modulus, Poisson's coefficient and density). Then, we measure the transfer function of waves transmitted through an alignment of particles. These measures show the existence of a cutoff frequency below which waves propagate and above which waves are evanescent. An alignment of spheres indeed corresponds to a phononic crystal and the observation of the cutoff frequency relies with the existence of forbidden band for wavelengths shorter than the particles size. Our measures also reveal two phenomena which are however not predicted. The first one concerns resonance peaks at low frequency and the second one deals with the occurrence of a band gap at low frequency. Our analysis and additional measurements allows identifying that the peaks at low frequency are caused by the presence of bending modes of the supports. Next, the quantification of the behavior of the low frequency cutoff as a function of the axial static load and for different combinations of spheres and supports materials, allows to infer that the band gap at low frequency relies on the occurrence of an elastic on-site potential between the spheres and the supports: the low frequency cutoff ω_0 is related to a local stiffness k_0.

In the chapter four, we focus on the experimental determination of the dispersion relation in dry media and on its analysis. A model including on on-site elastic potential, via a tangential deformation of the spheres on their supports, recovers the trend of both

the low and the high cutoff frequency as a function of relevant parameters. At the stage of the study, we quantify the characteristics of waves, such as the phase and the group velocity and the associated attenuation lengths inside the propagative band of the phononic crystal. On this purpose, we use a non-intrusive sensor embedded in a sphere to access and track the evolution of acoustic perturbations as they propagate through the alignment of particles; the protocol allows reconstructing the full dispersion relation of any sample. The experiment is performed in an alignment of polyacetal spheres clamped between steel cylindrical supports and submitted to a static load of either 20 N or 40 N. The experimental results clearly show the generation of two forbidden bands, at low and high frequency, separated by a propagative band; our measures additionally reveal a trace of the dispersion relation of bending waves that propagates inside the supports. At 20 N, the low and the high cutoff frequency are about 1450 Hz and 4100 Hz, respectively, whereas the theoretical estimation provided 1440 Hz and 4120 Hz, respectively. At 40 N static load, we find 1800 Hz and 4700 Hz in experiments and 1620 Hz and 4620 Hz in theory. Qualitatively and quantitatively, the measured dispersion relation matches the theoretical description within a fair accuracy. The results presented in this chapter constitute a robust framework and the description of dry media serves as a reliable reference for the rest of the study.

In the chapter five, we focus on wave propagation in wet granular alignments; we here set a small drop of viscous fluid between each spheres; the spheres are made of polyacetal and they are supported by four steel rods. We perform experiments over a wide range of static loads, viscosities and frequencies. In each case, we quantify both the group velocity and the attenuation. Our results show that the dynamics of our samples depends on the interplay between the elastic particles via the viscous fluid. We model the mechanical impedance between two particles as the contribution of two effects. The first one comes from an elastic term described by the Hertz potential, which relies on the behavior of the central part of the contacts under static load. The stiffness related to the region has the form $k_H \propto ER(P/E)^{1/3}$, where R is the radius of the spheres, E is their Young modulus and P is the confinement pressure. The second effect comes from the contribution of the viscous fluid at the periphery of the elastic contact. A careful analysis of the wave speed shows that this contribution induces an additional mechanical impedance of the form $\kappa_w \propto ER\,(\omega\mu/E)^{1/3}$, where μ is the fluid's viscosity and ω is the angular frequency. This expression render an elastohydrodynamic behavior, well described in the literature [25–28, 28], in which the fluid deforms the solid owing to the extreme shear rates, viscous stresses and consequently hydrodynamic pressure generated near the geometrical singularity of the elastic contact. The model we propose qualitatively and quantitatively explains our measurement of the wave speed; the agreement for the loss factor is qualitative and predicts a fair and satisfactory order of magnitude of the dissipation.

In the sixth and last chapter, we focus on longitudinal ultrasonic waves transmission through dry and wet 3D granular media. Our samples are made of few layers of millimetric particles. These experiments are performed with polyacetal spheres, under a

5 kPa confinement pressure and with a fluid with viscosity equal to 5 Pa. We analyze the propagation of waves in the low frequency region, in the long wavelength approximation and at different driving magnitude. The speed of longitudinal waves measured in the dry configuration is fairly predicted by the effective medium theory [8,9]. The wet configuration is obtained by mixing a small quantity of fluid with the particles. In this case, our measurements and our analysis show that a correction of the effective medium theory that take into account for the elastohydrodynamic behavior of the wet contacts, such as deduced from the measurements in 1D media, fairly reproduces both the measured wave speed and the attenuation at low frequencies. We also present experiments at higher frequencies; here, the wavelength tends to the size of the particles and the attenuation due to multiple scattering of the waves becomes dominant.

Contexte et résumé

Les matériaux granulaires, comme par exemple le sable, sont intriguant par nature: ils peuvent se comporter comme des solides lorsque le paquet de grains est sous pression ou se comportent comme des liquides ou des gaz lorsqu'on les fait couler ou lorsqu'ils sont vibrés [1, 2]. Les ondes acoustiques qui se propagent via les contacts entre grains dans les milieux granulaires, le long des chaînes de force, peuvent servir à sonder de manière non-intrusive ces matériaux [3–6]. Contrairement aux milieux continus, où la vitesse des ondes dépend de l'élasticité et de la densité intrinsèque du matériau, la vitesse des ondes dans les milieux granulaires dépend de la raideur des contact entre grains, de leur masse, mais également du nombre de contacts par grain (le nombre de coordinance), de leur compacité et de la précontrainte statique qui leur est appliquée [7–9]. Dans le sable humide, par exemple lorsque du fluide s'immisce entre les grains grâce aux forces capillaires, les propriétés acoustiques (vitesse, atténuation) peuvent être influencées de manière spectaculaire et non triviale. L'effet d'un fluide interstitiel a été montrée par des expériences concernant la propagation d'ondes dans les milieux granulaires secs et humides [10], où les auteurs ont observé deux effets antagonistes. D'une part, en utilisant des fluides de tension de surfaces différentes et de même viscosité, il a été observé une diminution de la vitesse de l'onde par rapport au sec. Ce fait est associé à une diminution du nombre de coordinance. D'autre part, l'utilisation du fluide de même tension de surface et de viscosités différentes, a permis de mettre en évidence une augmentation de la vitesse de propagation, attribuée à une augmentation de la raideur de contact due à une augmentation de la surface de contact entre particules rugueuses, lorsque celles-ci sont lubrifiées. Une stratégie pour dissocier ces deux effets antagoniste consiste à étudier un milieu granulaire dont le nombre de coordinance est parfaitement connu et constant [11] : c'est le cas des milieux granulaires unidimensionnels (1D), où chaque particule est en contact avec deux voisines. C'est l'approche que nous adoptons dans ce travail : nous considérons des alignements de sphères, comme analogue des chaînes de force dans les milieux granulaires tridimensionnels (3D), pour nous focaliser notre attention sur la dynamique de l'interaction entre le fluide et les particules.

Depuis une dizaine d'année, les milieux granulaires 1D suscitent l'intérêt de nombreux groupes de recherche [12–24] par la richesse des propriétés non-linéaires qui les régissent et par les applications potentielles qu'ils permettent d'envisager. Motivé par ces faits, nous avons examiné en détail, dans cette thèse, la dynamique d'alignements de particules sèches et humides. Pour cela, nous sondons tout d'abord le cas de référence, des chaînes de sphères sèches. Ici, nous observons que le couplage élasto-frictionnel entre les grains et un substrat (les supports sur lesquels sont posés les grains) induit un potentiel local, qui à son tour provoque une bande interdite à fréquence nulle: la transmission des vibrations à basses fréquences sont filtrées. Ensuite nous sondons la propagation d'ondes dans des alignements granulaires humides. Dans ce cas, nous montrons qu'une description élastohydrodynamique combinée au potentiel de Hertz décrit avec précision toutes nos observations expérimentales. In fine, nous extrapolons ces observations à des

milieux granulaires 3D. Nous montrons ici que la théorie du milieu effectif combinée à la description élasto-hydrodynamique du contact entre grains reproduit fidèlement les caractéristiques des ondes transmises. Nos résultats contribuent donc à une meilleure compréhension de la propagation des ondes dans les milieux granulaires humides réels. Nous présentons dans la suite un résumé détaillé de la thèse de doctorat.

Dans le chapitre deux, nous présentons les principales caractéristiques et les différents mécanismes qui régissent les milieux granulaires. Nous nous attachons en particulier à décrire la dynamique des contacts entre grains secs et humides. Ensuite, nous exposons des résultats expérimentaux préliminaires concernant la propagation des ondes dans les milieux granulaires secs et humides. A la fin du chapitre, nous exposons les défis que soulève la description fine de la propagation des ondes dans un milieu granulaire humide.

Dans le chapitre trois, nous menons une étude expérimentale détaillée dans des chaînes granulaires de sphères sèches. Premièrement, à partir de mesures ultrasonores, nous mesurons les caractéristiques intrinsèques des matériaux dont sont constituées nos sphères (module d'Young, coefficient de Poisson et densité). Ensuite, nous effectuons une mesure de la fonction de transfert en transmission au travers d'un alignement de particules. Ces mesures montrent la présence d'une fréquence de coupure en dessous de laquelle des ondes se propagent et au-dessus de laquelle ne subsistent que des ondes évanescentes. L'alignement de sphères correspond en effet à un cristal phononique et l'observation de la fréquence de coupure est compatible avec l'existence d'une bande interdite aux longueurs d'ondes inférieures à la taille de la maille élémentaire du réseau. Nos mesures mettent également en évidence deux phénomènes qui ne sont en revanche pas prédits. Le premier concerne des pics de résonance à basses fréquences et le deuxième montre l'existence d'une bande interdite à basse fréquence. Notre analyse et des mesures complémentaires permettent d'identifier que les pics à basse fréquence sont provoqués par la présence d'un mode de flexion des supports. Ensuite, la quantification de l'évolution de la fréquence de coupure basse en fonction de la charge statique appliquée sur l'alignement et pour différentes combinaisons de sphères et de supports, permet de déduire que la bande interdite à fréquence nulle repose sur l'existence d'un potentiel élastique locale (on-site potential) entre les sphères et les supports : la fréquence de coupure basse ω_0 est liée à une raideur k_0 locale.

Dans le chapitre quatre, nous nous concentrons sur la mesure de la relation de dispersion expérimentale dans des chaines granulaires secs et sur son analyse détaillée. Un modèle incluant un potentiel élastique local, par l'intermédiaire d'une déformation en cisaillement des sphères sur leurs supports, décrit fidèlement à la fois de la basse et la haute fréquence de coupure en fonction des paramètres du modèle. A ce stade de l'étude, nous mesurons alors les caractéristiques des ondes, telles que la vitesse de phase, la vitesse de groupe et les longueurs d'atténuation associées au sein de la bande passante du réseau phononique. Pour cela, nous utilisons un capteur non intrusif embarqué dans une bille pour accéder à l'évolution de perturbations acoustiques qui se propage le long d'un alignement de particules; ce protocole nous permet de reconstruire l'intégralité de la relation de dispersion dans la bande passante. L'expérience est réalisée dans un

alignement de sphères en polyacétal posées sur des supports en acier et soumis à une charge statique de 20 N ou de 40 N. Les résultats expérimentaux montrent clairement la génération de deux bandes interdites, à basse et haute fréquences, séparées par une bande passante; ces mesures révèlent également une trace de la relation de dispersion des ondes de flexion qui se propagent dans les supports. A 20 N, les fréquences de coupure haute et basse sont d'environ 1450 Hz et 4100 Hz, respectivement, alors que l'estimation théorique indique des valeurs de 1440 Hz et 4120 Hz, respectivement. A 40 N, nous trouvons des fréquences de coupure de 1800 Hz et 4700 Hz expérimentalement et de 1620 Hz et 4620 Hz en théorie. Qualitativement et quantitativement, la relation de dispersion mesurée correspond donc bien à la description théorique, avec une grande précision. Les résultats présentés dans ce chapitre constituent donc un cadre solide et la description des milieux secs sert de référence fiable pour le reste de l'étude.

Dans le chapitre cinq, nous nous intéressons à la propagation des ondes dans un milieu granulaire 1D mouillé; on place une goutte de fluide visqueux entre chaque sphère; les sphères sont en polyacétal et elles sont disposée entre quatre tiges d'acier. Nous effectuons des expériences pour une large gamme de charge statique, de viscosité et de fréquence. Dans chaque cas, nous quantifions à la fois la vitesse de groupe et l'atténuation. Nos résultats montrent que le comportement dynamique de nos échantillons dépend de l'interaction entre les particules élastiques via le fluide visqueux. Nous modélisons l'impédance mécanique entre deux particules comme la contribution de deux effets. Le premier vient d'une contribution élastique décrit par le potentiel de Hertz qui provient de la partie centrale des contacts sous précontrainte statique. La rigidité de cette région est de la forme $k_H \propto ER(P/E)^{1/3}$, où R est le rayon des sphères, E est le module d'Young et P est la pression de confinement. Le deuxième effet provient de la contribution du fluide visqueux à la périphérie du contact élastique. Une analyse attentive de la vitesse des ondes montre que cette contribution additionnelle engendre une impédance mécanique supplémentaire de la forme $\kappa_w \propto ER\left(\omega\mu/E\right)^{1/3}$, où μ est la viscosité du fluide et ω est la fréquence angulaire. Cette expression rend compte d'un comportement élasto-hydrodynamique, bien décrit dans la littérature [25–28, 28], dans lequel le fluide déforme le solide en raison de taux de cisaillement, de contraintes visqueuses et donc de pression hydrodynamique extrêmes générés à proximité de la singularité géométrique de la zone de contact. Le modèle que nous proposons explique qualitativement et quantitativement nos mesures de vitesse de propagation; l'accord sur le facteur de perte reste qualitatif et le modèle prévoit un ordre de grandeur satisfaisant de la dissipation.

Dans le sixième et dernier chapitre, nous nous intéressons à la transmission d'ondes ultrasonores longitudinales au travers d'empilements 3D aléatoires compacts secs ou mouillés. Nos échantillons sont composés de quelques couches de particules millimétriques. Ces expériences préliminaires sont réalisées avec des particules en polyacétal, sous une pression de confinement de 5 kPa et avec un fluide de viscosité 5 Pa.s. Nous analysons la propagation d'ondes dans la gamme des basses fréquences, dans l'approximation des grandes longueurs d'ondes, et pour différentes amplitudes d'excitation. La vitesse de propagation des ondes de compression que nous mesurons dans le cas sec est en accord

avec les prédictions données par le modèle de milieu effectif [8,9]. La configuration mouillée est obtenue en mélangeant une petite quantité de fluide aux grains. Dans ce cas, nos mesures et notre analyse montre qu'une correction du modèle de milieu effectif prenant en compte le comportement élasto-hydrodynamique des contacts mouillés, tel que déduit des mesures dans un milieu granulaire 1D, reproduit fidèlement à la fois la vitesse de l'onde mesurée et l'atténuation à basses fréquences. Nous présentons également des expériences à plus hautes fréquences; ici la longueur d'onde atteint la taille des particules et l'atténuation due à la diffusion multiple des ondes devient dominant.

Chapter 2

The Physics of granular media: state of the art

Contents

In this introductory chapter we present at first the main characteristic of a granular media. In the next sections we focus on the contact dynamics between dry and wet grains. Finally we treat existing experimental and analytic study on wave propagation in dry and wet granular media.

2.1 Granular media: from phononic crystals to metamaterials

Photonic crystals, phononic crystals and metamaterials are composite structures which tailor wave dispersion as to achieve given spectral and phase properties [29]. Owing to Bragg's scattering in the case of photonic and phononic crystals and to local resonances in the case of metamaterials, these composite materials produce so called band gap in transmitted spectra, where the wave propagation is strongly attenuated.

A photonic crystal is a periodic structure which affects and control electromagnetic wave. The band gap in this type of material can inhibit spontaneous emission [30, 31] which plays a crucial role in limiting the performance of semiconductor laser junctions, bipolar transistors and solar cells. It is worth mentioning that photonic crystals can also facilitate the localization of light [32,33]. These materials are also important for quantum Optics and few specific systems or devices, including the black body radiation and single mode light emitting diode [34].

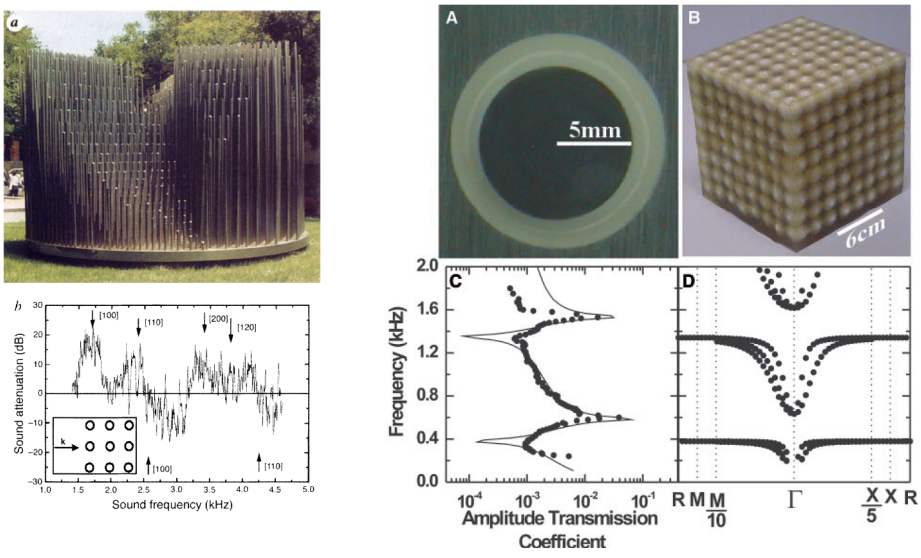

Figure 2.1: Left: (a) Phononic crystal made of steel tubes [35]. (b) Sound attenuation as a function of frequency, the arrow in the inset represents the direction of wave propagation. Right: [36] (A) elementary cell of metamaterial presented in (B). Transmission in (C) and dispersion relation (D) as a function of frequency, where circles are measured data and lines represent the theoretical estimations.

When one increases the wavelength, up to the range of elastic waves, one deals with phononic crystals, which affect the propagation of vibrational waves. The first one-dimensional phononic crystal able to tailor elastic wave propagation was reported in 1979 by Narayanamurti [37]. In the following decade, Sigalas showed the existence of band gaps in two-dimensional phononic structures [38] and in three-dimensional phononic crystals [35, 39]. These materials attenuate ultrasonic frequencies [40], surface acoustic waves [41] and act as filters [42]. The band gaps in photonic and phononic crystal relies on the Bragg scattering, when the periodicity of the crystal is comparable with the wavelength.

A third type of structures able to tailor wave dispersion are the metamaterials [36]. Here, the band gaps stem from locally resonant structures. In contradiction to phononic and photonic crystals, the band gaps are here created at wavelengths which may be few orders of magnitude larger than the characteristic periodicity of the crystal. Upon specific and intriguing features, this kind of materials can be designed to exhibit negative elastic modulus for instance.

Ordered granular media are one of these materials: they are periodic and have been shown to behave as phononic crystals. These specific assemblies of particles brought the attention of many scientific groups, both from their inherently rich and intriguing Physics and from the industrial applications they imply. Among potential applications, they have been proved reliable to absorb shocks [12–14], to localize and trap waves [15–19], or to design acoustic diodes [20] and acoustic lenses [21], from very low vibrational frequencies to the MHz frequency range when using micrometric particles [22–24].

2.2 The complexity of granular media

A granular material is an assembly of individual macroscopic and heterogeneous solid particles [43, 44]. They are omnipresent in nature as the sand in deserts, seeds, pile of rocks and even rings on Saturn. Granular materials are the second-most used material in industry after water [45, 46]. Grains are found in mining activity while extracting minerals, in civil engineering and in pharmaceutical industry for the manipulation of pills [47]. Granular media are also very important in geophysics to understand the mechanisms of avalanches, earthquakes, sediments transport and erosion of rocks [7].

Grains thus exist in nature at very different sizes, from dust to rocks. One distinguishes typical sizes depending on the relative contribution of the thermal energy, the van der Waals electrostatic attractive forces and the gravitational potential energy Mgd (where $M \sim \rho d^3$ is the mass of a grain, d its diameter, ρ its density and g the gravity). For grains larger than $d \gg (k_B T/\rho g)^{1/4} \sim 1$ μm (where k_B is the Boltzman constant and T is temperature), the thermal energy $k_B T$ is negligible compared to the potential energy: in this limit, granular media consist in athermal systems. For grains larger than $d \gg (A_h/r_{0A}\rho g)^{1/3} \sim 100$ μm [47] (where $A_h \sim 10^{-19}$ J is the Hamaker coefficient and $r_{0A} \sim 10^{-10}$ m is the typical distance between molecules), the van der Waals in-

teractions become negligible compared to the gravitational energy: the grains are non cohesive. Typically, grains in granular media are larger then 100 μm [43, 44].

Despite industrial applications and a long history of theoretical research pioneered by Coulomb, Reynolds and Faraday [1], the Physics of granular media is not yet fully described [47]. At present, a theory quantifying all the phenomena in granular media is lacking [47], even in the ideal case where granular media are constituted by identical spherical particles interacting only through elastic contacts [47].

Despite their complexity and specific nature, heterogeneous granular media possess the features of the continuous matter like fluids, solids and gases. One can take water as an example [48]: water at ambient temperature is liquid. When the temperature rises, it turns into a gas, and when the temperature decreases, the water freezes and becomes a solid. Each of these states has specific features. In the liquid state, the water has no definite shape, but has definite volume; additionally, liquids as opposed to solids present no resistance to shear. In the solid state, it has definite shape and volume. Finally in the gaseous state, the water has neither definite shape nor definite volume. The experiment of Forterre [2], as shown in Fig. 2.2, illustrates the three states of matter [48] in granular media, by simply pouring grains on a inclined plane. One can clearly distinguish three regions: a solid state where grains do not move, a liquid state where grains flow and a gaseous state where grains bounce in every directions.

There are few noticeable exceptions compared to the mechanical phases in continuous matter. In a granular solid there is no attractive force between the particles. In a granular liquid the grains interact via frictional contact. Finally in a granular gas the grains interact mainly via inelastic collision: granular media are athermal and the only source of fluctuations is external, for instance if one inclines or vibrates a pile of grains.

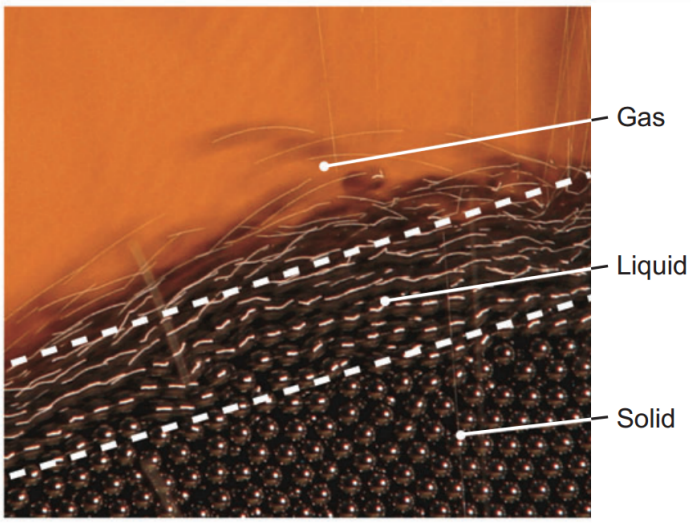

Figure 2.2: The tree states of granular media: gas, liquid and solid obtained by pouring granular material on an inclined plane [2].

Andreotti et al. [47] listed all the obstacles imparting the description of the Physics of granular media:

- Granular media generally contains large numbers of particles which are beyond simulations limits. For example, a spoon of sugar of 1 cm^3, with sugar grains of approximately 100 μm in diameter, contains a million of particles. In this case the aim of any theoretical description is to provide average quantities modeling the set of particles rather than following the dynamics of every particles in a pile.

- The separation between the microscopic and macroscopic scales is vague in granular media. For example, the flow shown in Fig. 2.2 is few grains deep only. This raises an issue, concerning the validity of a continuous description and the definition of elementary volumes.

- The interactions between grains are complex: typical mechanisms in dry media include for instance nonlinear contact dynamics, solid friction and inelastic collisions.

- When grains are immersed in fluid, hydrodynamics and adhesive forces have to be taken into account.

In the following sections we aim at providing all the details of the interactions occurring in dry and wet granular media. These are the elementary mechanisms that will serve throughout the manuscript to describe and analyze our findings.

2.3 Microscopic scale: dry contact mechanics

In the first place, we focus on the microscopic scale, at the level of the contacts between dry particles. The elastic energy of interaction between two bodies pressed against each other is quantified by their contact stiffness k_H, $U_{el} = k_H \delta_0^2/2$ where δ_0 is the overlap deformation. Here, we aim at deriving an expression for the stiffness k_H between two elastic spheres, first from a geometrical approximation, then from the exact derivation of the equations of elasticity. We then recall the features of the onset of plastic deformation in a third section, as the limit above which the linear Hookean elasticity does not hold anymore. Further, we consider the solid friction between bodies, which introduces shear deformations of the grains that can be accounted by the so-called Hertz-Mindlin model. Finally, we provide some details on the estimation of the adhesive force, related to the surface energy, between dry particles.

2.3.1 Hertz contact between two spheres: geometrical derivation

We consider two identical spheres with radius R_0 and Young's modulus E_0 compressed one against the other, as seen in Fig. 2.3. When the normal force F_0 increases, the overlap δ_0 increases: the distance between the centers decreases from $2R_0$ to $2R_0 - \delta_0$. As a consequence, the spheres flatten, creating a disk of contact with radius a.

The deformation of the contact induces a deformation inside the spheres, near the contact; the typical depth of the deformation matches approximately the radius a of the disc of contact [49]. The relation between a and δ_0 is given by the law of Pythagoras,

$$R_0^2 = \left(R_0 - \frac{\delta_0}{2}\right)^2 + a^2. \tag{2.1}$$

Within small deformation, $\delta_0 \ll R_0$, one obtains the approximation,

$$a \simeq \sqrt{R_0 \delta_0}. \tag{2.2}$$

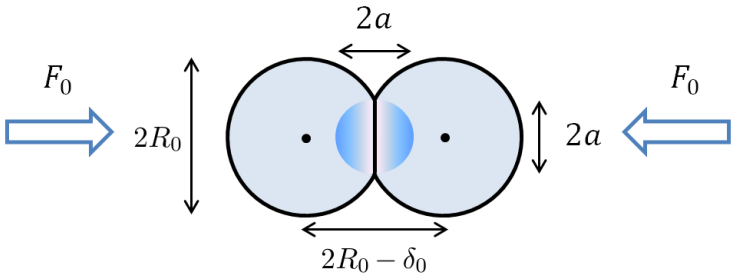

Figure 2.3: Two spheres with radius R_0 compressed with a static force F_0.

In the following, we then consider a Hookean solid; for sake of simplicity, we assume a zero Poisson ratio, $\nu_0 = 0$,

$$\sigma = E_0 \epsilon, \tag{2.3}$$

where σ is the stress,

$$\sigma \simeq \frac{F_0}{\pi a^2}, \tag{2.4}$$

and ϵ is the strain,

$$\epsilon \simeq \frac{\delta_0}{a}. \tag{2.5}$$

By combining Eq. 2.2, Eq. 2.4 and Eq. 2.5 in Eq. 2.3, one obtains a relation between the applied static force F_0 and the overlap distance δ_0,

$$F_0 \propto E_0 R_0^2 \left(\frac{\delta_0}{R_0}\right)^{3/2}. \tag{2.6}$$

The contact stiffness is the derivative of the force with the deformation, $k_H = \partial F_0 / \partial \delta_0$,

$$k_H \propto E_0 R_0 \left(\frac{\delta_0}{R_0}\right)^{1/2} \propto E_0 R_0 \left(\frac{F_0}{E_0 R_0^2}\right)^{1/3}. \tag{2.7}$$

The stiffness thus increases nonlinearly with the overlap or the static force; this is consistent with the fact that the contact region between solids widens when the overlap

increases, see Eq. 2.2.

2.3.2 Hertz contact between two spheres: exact derivation

The rigorous and exact derivation of Hertz contact is detailed in most of the reliable textbooks [49–51]. Here, we summarize the calculations derived by Popov [51].

In this approach, one considers an elastic medium that fills an infinitely large half-space. Under the influence of force F_0, the medium is deformed. This deformation acts in the xy plane, as shown in Fig. 2.4(a). From a force acting at the origin in the positive z-direction, one obtains the displacement u_z in the form [49],

$$u_z = \frac{1}{\pi E} \int \int p(x', y') \frac{dx'dy'}{r}, \tag{2.8}$$

where r is the radial coordinate, $r = \sqrt{(x - x')^2 + (y - y')^2}$, $E = E_0/(1 - \nu_0^2)$ with ν_0 the Poisson ratio, and p stands for the continuous distribution of normal pressure. Here, p is the Hertz pressure distribution,

$$p = p_0 \left(1 - \frac{r^2}{a^2}\right)^{1/2}, \tag{2.9}$$

where p_0 is the maximum pressure at the center of contact and a is the radius of the contact disc. One estimates the static force from Eq. 2.9 as

$$F_0 = \int_0^a p(r) 2\pi r dr = \frac{2}{3} p_0 \pi a^2. \tag{2.10}$$

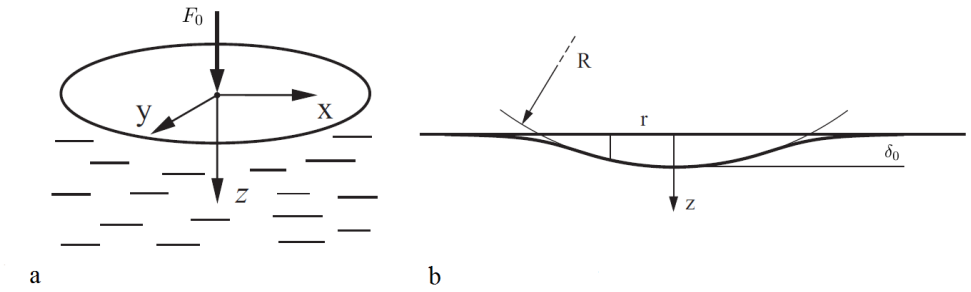

Figure 2.4: (a) Static force F_0 applied on an elastic half space, (b) rigid sphere pushed against an elastic half space [51].

Inserting Eq. 2.9 into Eq. 2.8 gives the displacement of the surface $r \leqslant a$,

$$u_z = \frac{\pi p_0}{4Ea}(2a^2 - r^2). \tag{2.11}$$

In parallel, if one regards the indentation of the sphere (with radius R) in the plane, as shown in Fig. 2.4(b), the displacement u_z of the surface can be set in the following

form

$$u_z = \delta_0 - r^2/2R. \tag{2.12}$$

The comparison of Eq. 2.11 and Eq. 2.12 yields

$$\frac{\pi p_0}{4Ea}\left(2a^2 - r^2\right) = \delta_0 - r^2/2R, \tag{2.13}$$

from which one identifies a and δ_0 as,

$$a = \frac{\pi p_0 R}{2E}, \tag{2.14}$$

$$\delta_0 = \frac{\pi a p_0}{2E}. \tag{2.15}$$

The substitution of Eq. 2.14 into Eq. 2.15 gives the maximum pressure,

$$p_0 = \frac{2}{\pi} E \left(\frac{\delta_0}{R}\right)^{1/2}, \tag{2.16}$$

and the radius of the contact disc,

$$a = \sqrt{R\delta_0}. \tag{2.17}$$

The relation between δ_0 and F_0 is obtained by inserting Eq. 2.16 and Eq. 2.17 into Eq. 2.10,

$$F_0 = \frac{4}{3} E R^2 \left(\frac{\delta_0}{R}\right)^{3/2}, \tag{2.18}$$

from which one obtains

$$a = \left(\frac{3FR}{4E}\right)^{1/3}. \tag{2.19}$$

The contact stiffness, $k_H = \partial F_0/\partial\delta_0$, finally becomes

$$k_H = ER\left(\frac{4\delta_0}{R}\right)^{1/2} = ER\left(\frac{6F_0}{ER^2}\right)^{1/3}. \tag{2.20}$$

It is worth mentioning that the contact stiffness between two spheres (radius R_1 and R_2, Young's moduli E_1 and E_2 and Poisson ratio ν_1 and ν_2) is obtained by replacing in Eqs. 2.8-2.20 the radius R by the effective radius,

$$R = 1/(1/R_1 + 1/R_2), \tag{2.21}$$

and by replacing the elastic modulus E by the effective value,

$$E = 1/[(1-\nu_1^2)/E_1 + (1-\nu_2^2)/E_2]. \tag{2.22}$$

In Eq. 2.20, as in Eq. 2.7, the contact stiffness depends on bulk characteristics of the spheres and increases with the static force. In fact, the geometrical derivation Eq. 2.7

yet provided a fair qualitative estimation of k_H.

2.3.3 Onset of plastic deformation

The combination of Eq. 2.16 and Eq. 2.18 provides a relation between the force and maximum pressure,

$$p_0 = \left(\frac{6F_0E^2}{\pi^3R^2}\right)^{1/3}. \tag{2.23}$$

Eq. 2.23 serves for the estimation of the onset of plastic deformation, according to von Miss criteria [50],

$$\sigma_Y = 1.6p_0, \tag{2.24}$$

where σ_Y is the yield strength characteristic for each material, indicating the maximal compression force F_Y at which a plastic deformation occurs inside the contact area,

$$F_Y = \frac{\pi R^3}{6E^2(1.6\sigma_Y)^3}. \tag{2.25}$$

2.3.4 Hertz-Mindlin contact between two spheres

As in subsections 2.3.1-2.3.2, here we consider two identical spheres with radius R_0, Young's modulus E_0 and Poisson ratio ν_0 compressed one against the other with F_0, as seen in Fig. 2.5. In this case, in addition to F_0, one exerts a tangential force F_t [50] producing a tangential deformation δ_y in the y-axis direction.

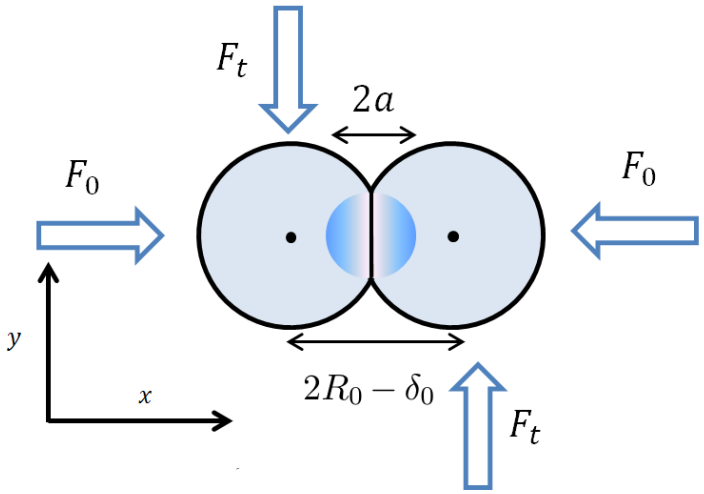

Figure 2.5: Two spheres with radius R_0 pushed against each other with a static force F_0; an additional tangential force F_t is applied causing micro displacement or shearing in y-axis.

Depending on the magnitude of F_t in respect to the friction force threshold $\mu_s F_0$, where μ_s is the friction coefficient, one distinguishes two cases. If the tangential force

exceeds the friction threshold $F_t > \mu_s F_0$, micro slips occur and the sphere slides onto the other. In the opposite, if $F_t < \mu_s F_0$, the spheres stick and shear deformations occurs. In the stick regime, the shear displacement δ_y reads [7, 8]

$$\delta_y = \frac{F_t}{8a}\left(\frac{2-\nu_0}{G_0}\right), \tag{2.26}$$

where a is the radius of the disc of contact defined by Eq. 2.19 and G_0 is elastic shear modulus, $G_0 = E_0/2(1+\nu_0)$.

The transverse contact stiffness k_t is the derivative of the tangential force with the tangential deformation, $k_t = \partial F_t/\partial\delta_y$,

$$k_t = \frac{8aG_0}{2-\nu_0}. \tag{2.27}$$

If one estimates k_t between spheres (radius R_1 and R_2, Young's moduli E_1 and E_2, Poisson ratio ν_1 and ν_2 and shear moduli G_1 and G_2), the equations Eq. 2.21 and Eq. 2.22 should be taken into account while estimating a by Eq. 2.19. Additionally Eq. 2.27 takes the form

$$k_t = 4a\left(\frac{G_1}{2-\nu_1} + \frac{G_2}{2-\nu_2}\right). \tag{2.28}$$

Similarly to the normal stiffness given in Eq. 2.20, the transverse stiffness k_t increases nonlinearly with the overlap or the static force: the tangential stiffness depends on the radius of the contact disc and the bulk characteristic of the spheres.

2.3.5 Contact between a sphere and a cylinder

Here, we consider a sphere with Young's modulus E_0, Poisson ratio ν_0 and shear modulus $G_0 = E_0/2(1+\nu_0)$ compressed with static force F_0 against a straight cylinder with radius R_c, Young's modulus E_c, Poisson ratio ν_c and shear modulus $G_c = E_c/2(1+\nu_c)$. The cylinder corresponds to one of the supporting rod used to align the spheres in our setup, as detailed in the next chapter. The curvature of the two bodies makes the rigorous treatment difficult to derive. However, such a configuration is equivalent in first approximation to the contact between a plane and a curved cylinder, which has been derived by Popov [51]. In the presence of a tangential force F_t, the tangential contact stiffness k_0 reads [51]

$$k_0 = 2G_r a, \tag{2.29}$$

where G_r is the reduced shear modulus $G_r = 1/[(2-\nu_0)/4G_0 + (2-\nu_c)/4G_c]$, $a = \sqrt{R_r\delta_0}$ and R_r is the effective radius given by

$$R_r = \sqrt{R_0 R_c}. \tag{2.30}$$

While estimating the contact radius a by Eq. 2.19 one should take into account

effective Young's modulus defined by

$$E_r = 1/[(1-\nu_0^2)/E_0 + (1-\nu_c^2)/E_c]. \tag{2.31}$$

It is worth mentioning that k_0 depends on the contact radius, giving the same non-linear dependency with the normal static force as in Eq 2.28.

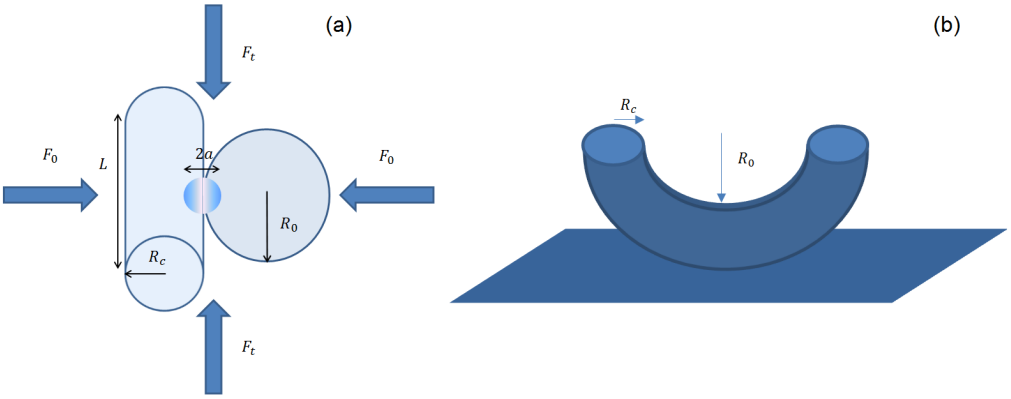

Figure 2.6: The contact between a sphere and a cylinder is equivalent to a contact between a plane and a curved cylinder.

2.3.6 Adhesive contact models between dry surfaces

Next, we consider the contact between two compressed bodies, where the surface tension γ_s is taken into account. Due to the presence of γ_s, one has an adhesive contribution F_{adh} [47] to the net force. In this subsection we derive an expression for F_{adh}, first in a qualitative way then from an exact derivation of adhesive contact model.

In both cases, the surface tension γ_s is defined [47,51] as the work per unit area done by an external force to pull two bodies apart and create two surfaces. Half of the energy required to create one surface is the surface tension γ_s.

Qualitative derivation

When two spheres with radius R_0 are pulled one from the other, the overlap distance δ_0 and so the radius a of the contact region changes as a function of time, which in turn provokes the change of contact area A,

$$dA = d(\pi a^2), \tag{2.32}$$

and consequently, the variation of the surface energy is

$$dU_{surf} = 2\gamma_s d(\pi a^2), \tag{2.33}$$

and is equal to the work done by the force of adhesion,

$$2F_{adh}d\delta_0 = dU_{surf}. \tag{2.34}$$

Combining $a = \sqrt{2\delta_0 R_0}$ with Eq. 2.33 and Eq. 2.34, the force of adhesion reads

$$F_{adh} \propto \gamma_s R_0. \tag{2.35}$$

The adhesive force does not depend on the compression nor on the elastic characteristics of the spheres.

Exact model

There exists two main adhesive contact models. The first one is the JKR model [52], which considers the pressure distribution and the adhesion inside the contact region. The second one is the DMT [53] model, which considers a Herztian contact with additional adhesive part outside the contact region.

Both these models are valid but within different conditions [54]. The JKR model is used for spheres with small Young's modulus and high surface energy. The DMT is more suited for rigid spheres with low surface energy.

In this subsection, we remind the detailed and rigorous derivation of F_{adh} in the frame of the JKR model as presented in [51]. Here, we attempt to derive an expression for the force of adhesion between a sphere (with Young's modulus E and radius R) and a plane: the displacement u_z of the surface is calculated [51] in the half-space (as in Fig. 2.4 and reads

$$u_z = \frac{1}{\pi E}\int\int p(x',y')\frac{dx'dy'}{r}, \tag{2.36}$$

where $r = \sqrt{(x-x')^2+(y-y')^2}$ and $E = \frac{E_0}{1-\nu_0^2}$.

The expression for the displacement is the same as for the Hertz model derivation, Eq 2.8. However in the JKR model [51], the pressure distribution p is equal to

$$p = p_0\left(1-r^2/a^2\right)^{-1/2} + p_1\left(1-r^2/a^2\right)^{1/2}. \tag{2.37}$$

By inserting Eq. 2.37 in Eq. 2.36, one obtains the displacement in the form

$$u_z = \frac{\pi a}{E}\left[p_0 + \frac{1}{2}p_1\left(1-\frac{r^2}{2a^2}\right)\right]. \tag{2.38}$$

In parallel, the displacement u_z of the surface is

$$u_z = \delta_0 - r^2/2R, \tag{2.39}$$

where δ_0 is the overlap deformation. By comparing Eq. 2.38 and Eq. 2.39, one obtains,

$$p_1 = \frac{2Ea}{\pi R}, \tag{2.40}$$

$$p_0 = \frac{E}{\pi}\left(\frac{\delta_0}{a} - \frac{a}{R}\right), \tag{2.41}$$

and so far, one has three unknowns p_0, p_1 and a (for the given penetration depth δ_0) and two equations, Eq. 2.40 and Eq. 2.41. A third constrain is thus required [51], which states that the total energy U_{tot} of the system should be minimum at equilibrium a,

$$\frac{\partial U_{tot}}{\partial a} = 0. \tag{2.42}$$

The total energy comes from both the elastic deformation and the adhesion,

$$U_{tot} = U_{el} - \gamma_s \pi a^2, \tag{2.43}$$

where the elastic part of the total energy is defined as

$$U_{el} = \frac{1}{2}\int p(\mathbf{x},\mathbf{y}) u_z(\mathbf{x},\mathbf{y}) dxdy. \tag{2.44}$$

The substitution of Eq. 2.37 and Eq. 2.39 into Eq. 2.44 gives

$$U_{el} = E\left[\delta_0^2 a - \frac{2}{3}\frac{\delta_0 a^3}{R} + \frac{a^5}{5R^2}\right], \tag{2.45}$$

and the total energy Eq. 2.43 becomes

$$U_{tot} = E\left[\delta_0^2 a - \frac{2}{3}\frac{\delta_0 a^3}{R} + \frac{a^5}{5R^2}\right] - \gamma_s \pi a^2. \tag{2.46}$$

Next, by combining Eq. 2.42 and Eq. 2.46, one obtains the overlap deformation,

$$\delta_0 = \frac{a^2}{R} \pm \sqrt{\frac{2\gamma_s \pi a}{E}}. \tag{2.47}$$

The force acting on the sphere is the derivative of U_{tot} with respect to δ_0,

$$F = -\frac{\partial U_{tot}}{\partial \delta_0} = E\left[2\delta_0 a - \frac{2}{3}\frac{a^3}{R}\right], \tag{2.48}$$

then inserting Eq. 2.47 into Eq. 2.48 one has

$$F = E\left[\frac{4}{3}\frac{a^3}{R} - \left(\frac{8\gamma_s \pi a^3}{E}\right)^{1/2}\right], \tag{2.49}$$

the maximum negative value of Eq. 2.49 is reached when

$$a = a_{crit} = \left(\frac{9}{8}\frac{\gamma_s \pi R^2}{E}\right)^{1/3}, \tag{2.50}$$

and is equal to the adhesive force,

$$F_{adh}^{JKR} = -\frac{3}{2}\pi\gamma_s R, \tag{2.51}$$

where F_{adh}^{JKR} denote the adhesive force estimated by JKR model.

It is worth mentioning that in the DMT model, the pressure distribution in Eq. 2.37 corresponds to the Hertz potential given by Eq. 2.9 but with an additional attractive contribution exerted at the periphery of the solid contact,

$$F_{adh}^{DMT} = -4\pi\gamma_s R. \tag{2.52}$$

When one considers the contact between two spheres (with radius R_1 and R_2), the radius of curvature should be replaced in Eq. 2.51 and in Eq. 2.52 by the effective radius,

$$R = 1/[1/R_1 + 1/R_2]. \tag{2.53}$$

In accordance with Eq. 2.35, the adhesive force does not depend on the compression nor on elastic characteristics of the sphere (E, ν_0), but instead increases linearly with the radius of the spheres. We will se in the next chapters that this type of adhesion remains negligible and does not show up in our experiments: dry spheres are non-cohesive.

2.4 Microscopic scale: wet contact mechanics

In this section, we consider the contact dynamics between wet bodies: thanks to capillary forces, the presence of a small quantity of fluid forms a liquid meniscus near the singular point of contact between bodies. Here, we aim at deriving the mechanical impedance κ_ω (the mechanical impedance is the ratio between the force and the deformation) between two spheres with an interstitial fluid. First of all, we briefly remind the description of capillary forces (the Laplace force) that give birth to an interstitial meniscus of fluid in between non-conformal solids. Then, we point out few aspects of a seminal theoretical and numerical work concerning the normal collision of a sphere on a thin layer of viscous fluid. Next, in the third section, we provide details on the hydrodynamic field generated in a viscous fluid collided by a perfectly rigid sphere: this is a classical limit of the lubrication theory. In the fourth part, we remind the exact derivation of κ_ω obtained from an elastohydrodynamic description at very small fluid thickness. Finally, in the last part we mention a more qualitative derivation of κ_ω at rather large fluid thicknesses, which asymptotically matches the lubrication limit.

2.4.1 Capillary forces in liquid bridges

Here, we derive qualitatively the expression for the capillary force F_{cap} between a sphere with radius R and a plane, see the Fig. 2.7. Due to the Laplace pressure Δp, the liquid forms a capillary bridge [51]. The pressure difference Δp depends on the surface tension

of fluid γ_f and on the radius of curvature of the capillary bridge r_0,

$$\Delta p = -\frac{2\gamma_f}{r_0}. \tag{2.54}$$

The height h of the capillary bridge is given by

$$h \simeq \frac{r^2}{2R}. \tag{2.55}$$

For a given radius of curvature $r_0 \simeq h$ and under the condition $r_0 \ll r$, Eq 2.54 becomes

$$\Delta p = -\frac{4\gamma_f R}{r^2}, \tag{2.56}$$

and the capillary force finally takes the form

$$F_{cap} = A\Delta p = -4\pi\gamma_f R, \tag{2.57}$$

where $A = \pi r^2$ is the area of the capillary bridge.

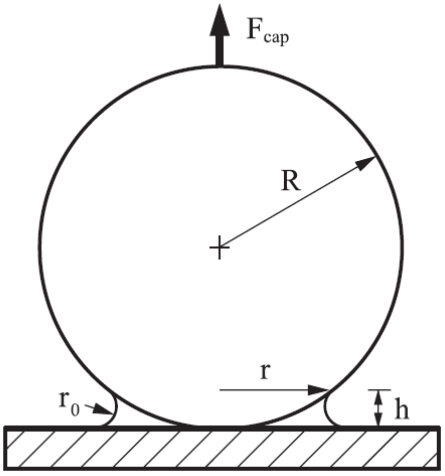

Figure 2.7: Capillary bridge formed at the contact between a sphere and a plane [51].

As for the force of adhesion between dry spheres (see Eq. 2.35, Eq. 2.51 and Eq. 2.52), the capillary force depends on the radius of curvature of the solid and is independent on the compression. If one regards the contact between two spheres with radius R_1 and R_2 the radius R should be replaced by its effective value $R = 1/(1/R_1 + 1/R_2)$.

2.4.2 A seminal work on the collision between wet spheres

The dynamics of collisions between wet bodies has attracted some attention since a decades. It is essential to understand the behavior of fluid coated spheres [55, 56] and immersed collisions [57–64] for instance. In contrast to a dry collision where particles

inertia dominates, the kinetic energy in liquid is dissipated by viscous stresses, in addition to inelasticity of the solids. When an elastic body collides a wet surface, the dissipation of energy can be quantified through the restitution coefficient e, which is the ratio of rebound velocity V_{out} to the incident velocity V_{in}, $e = V_{out}/V_{in}$. In a seminal publication, Davis, Serayssol and Hinch [65] identified two important parameters in this type of experiments. The first one is the Stokes number, which measures the inertia of the particles relatively to the viscous forces, $St \propto (\rho d V_{in})/\mu$, where d is the sphere diameter, ρ is the sphere density and μ is the fluid viscosity. The second one is the elasticity parameter $\epsilon \propto \mu V_{in} R^{3/2}/E h_0^{5/2}$, where h_0 is the minimal separation distance and E is the Young's modulus. The parameter ϵ indicates the tendency of the solid to deform elastically. For large values of ϵ, a significant deformation occurs during the collision. In contrast, rigid spheres provides small ϵ and no significant deformations of the elastic bodies occur. Davis et al. [65] analyzed in details the correlations of the two parameters St and ϵ with the restitution coefficient e of a sphere bouncing on a thin film of viscous fluid.

Through the careful analysis of the restitution coefficient of a sphere bouncing on a film of fluid, they reported that part of the kinetic energy is converted into elastic strain, enabling the spheres to rebound. This mechanism relies on the Stokes number: at low stokes number, the viscous dissipation is predominant and no rebound occurs. At large stokes number, the inertia contribution is predominant and enables the rebound of the sphere. As the viscosity of the fluid increases, the critical Stokes number above which the rebound is possible, decreases. According to [65] and [55], the experimental critical Stokes number St_c can be fitted by

$$St_c \simeq 0.54 ln\,(1/\epsilon) - 1.25. \tag{2.58}$$

Above St_c, the spheres are deformed elastically due to the hydrodynamic pressure exerted by the viscous fluid and a rebound is observed. The ansatz shows for instance that soft spheres (i.e. large ϵ) requires smaller Stokes number (i.e. smaller impact velocity) than hard spheres to rebound.

The interplay between elastic and viscous contributions is quantified in the elastohydrodynamic (EHD) model presented in more details in the following sections.

2.4.3 Reynolds force between a rigid sphere and a rigid plane

At first we consider the classical case of a rigid sphere impacting a flat rigid wall, as shown in Fig. 2.8: here, no elastic deformation occurs during the collision. The two bodies are separated by a layer of an incompressible fluid with thickness h and viscosity μ [11]. When the sphere with radius R is displaced against the wall with relative velocity $v_z < 0$ in the normal (axial) direction, the fluid is thinned, $\dot{h} = v_z < 0$, and squeezed out at velocity $v_r > 0$ in the radial direction. In this condition, the viscosity of the fluid induces a hydrodynamic pressure opposed to the displacement, which may induce in turn

the deformation of the bead [66] if the elasticity would be taken into account. Within the assumption of the absence of elastic deformation, the pressure is given by the Reynolds equation [66],

$$\frac{\partial}{\partial r}\left[\frac{rh^3(r,t)}{12\mu}\frac{\partial p(r,t)}{\partial r}\right] = r\dot{h}(r,t) = -rv_z(t), \tag{2.59}$$

where the fluid thickness is $h(r,t) = h_0(t)+r^2/2R = h_0\left[1+r^2/2Rh_0\right] = h_0\left[1+r^2/a_w^2\right]$. Here, $a_w = \sqrt{2Rh_0}$ is a characteristic extent of the hydrodynamic field and $h_0(t)$ is the separation distance between the sphere and the plane. The integration of Eq. 2.59 gives the hydrodynamic pressure in the form

$$p(r,t) = \frac{3\mu R v_z(t)}{h^2(r,t)}, \tag{2.60}$$

thus by integration of Eq. 2.60, one obtains the Reynolds force (i.e. the repulsive lubrication force),

$$F(t) = \frac{6\pi\mu R^2 v_z(t)}{h_0(t)}. \tag{2.61}$$

By combining Eq. 2.60 and Eq. 2.61, one finds a typical area S_w,

$$S_w = |F(t)/p(0,t)| \simeq 2\pi R h_0 \simeq \pi a_w^2, \tag{2.62}$$

which confirms that the typical extent of the hydrodynamic field is about $a_w = \sqrt{2Rh_0}$.

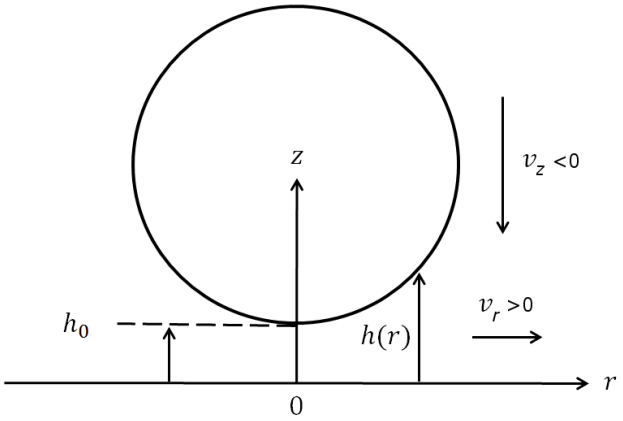

Figure 2.8: A rigid sphere and a rigid plane separated by a viscous fluid. The fluid is squeezed out radially when the sphere approaches the plane.

In turn, the Stokes equation allows relating the pressure distribution $p(r,t)$, see Eq. 2.60, with the radial velocity v_r or the shear rate $\dot{\gamma}_s = \partial v_r/\partial z$ in the fluid,

$$\frac{\partial p}{\partial r} = \mu\frac{\partial^2 v_r}{\partial z^2} = \mu\frac{\partial \dot{\gamma}_s}{\partial z}, \tag{2.63}$$

such that with no slip conditions at the interfaces between the solids and the fluid,

$v_r(r, z = 0, t) = v_r(r, z = h, t) = 0$,

$$v_r(r, z, t) = \left(\frac{3rv_z}{h}\right)\left(\frac{z}{h}\right)\left(1 - \frac{z}{h}\right), \tag{2.64}$$

and

$$\dot{\gamma_s}(r, z) = \left(\frac{3rv_z}{h^2}\right)\left(1 - \frac{2z}{h}\right). \tag{2.65}$$

We plot in Fig. 2.9 the radial velocity, the shear rate and the hydrodynamic pressure distributions as a function of the radial coordinate. One clearly observes that both the radial velocity $v_r(r, z = h_0/2)$ and the shear rate $\dot{\gamma_s}(r, z = 0)$ of the fluid are zero at $r = 0$, for symmetry reasons: the fluid does not flows near the central part of the contact. In addition, both these quantities are maximal near $r = a_w$, see Fig. 2.9(a) and (b). In particular, the shear stress $\tau = \mu\dot{\gamma_s}(r = a_w, z = 0)$ is maximal in a ring of radius a_w centered on $r = 0$, which impedes the flow accordingly. As far as the bodies get close to contact, at small fluid thickness $h_0 \to 0$, the fluid's shear rate and stress diverge and the fluid may ultimately gets clamped by its viscosity. In turn, the hydrodynamic pressure is maximal at the center $r = 0$ and has a typical extent of the order of a_w, see Fig. 2.9(c): the stress is thus mostly transmitted through the central part of the fluid, where it essentially does not flow. We will see in the sections that all these features are crucial and reminiscent of the specific behavior of a more complex elastohydrodynamic description.

Indeed, when the fluid thickness h_0 tends to zero, the hydrodynamic pressure diverges and will likely deform the elastic solids. However, the hydrodynamic pressure distribution given by Eq. 2.60 significantly differs from the Hertzian distribution in a dry contact, see for instance Eq. 2.9. In such a harsh condition, the relation between the repulsive force and the relative displacement of the bodies must significantly differs from the Hertz potential Eq. 2.18 and from the classical result Eq. 2.61 obtained in lubrication limit. This latter finally results in a rather complex elastohydrodynamic mechanism: we provide a detailed analysis and description of such an interplay in the following sections.

2.4.4 Mechanical impedance of a wet contact at small fluid thickness

Here, we aim at presenting the description of the elastohydrodynamic (EHD) interplay that occurs when two elastic bodies interact via a thin layer of viscous fluid. The EHD mechanism is observed at very different scales [56, 67–71], from nano object [72], through lubricated solids [73] and up to geophysical faults [74]. The seminal work of Davis, Serayssol and Hinch [65] showed, via detailed numerical study, that the close interplay between the hydrodynamic field in the layer of fluid and the elasticity of the solids fairly renders the dynamics of wet collisions. Only recently, over the last decade, the group of Charlaix [26, 27, 75–82] achieved breakthroughs in the description, the modeling, the characterization and the understanding of elastohydrodynamic interactions. Here and in

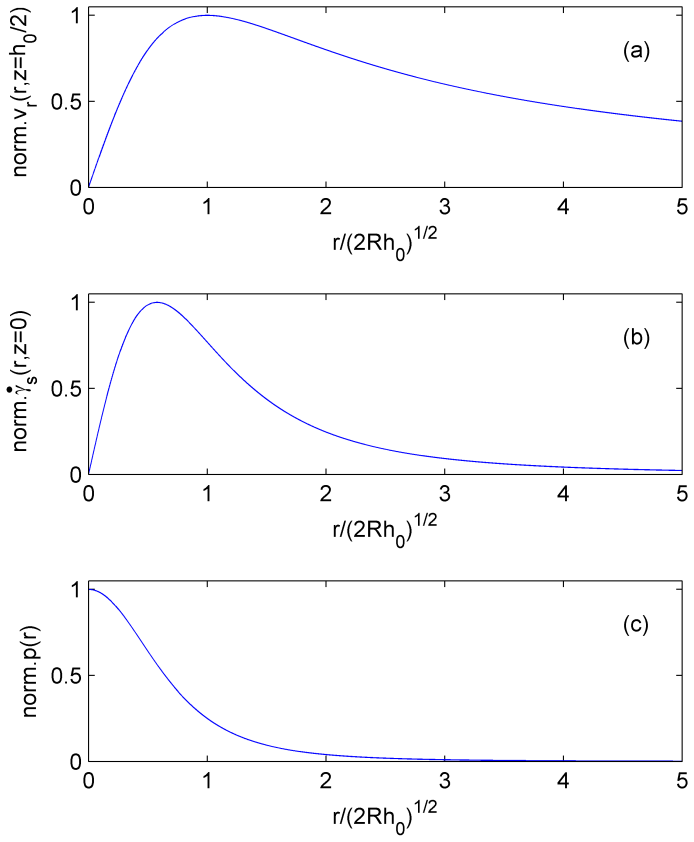

Figure 2.9: (a) Normalized radial velocity, (b) normalized shear rate and (c) normalized hydrodynamic pressure distribution as a function of the normalized radial coordinate $r/\sqrt{2Rh_0}$. Here, h_0 is the minimal distance between the sphere and the plane and R is the radius of the sphere.

the next section, we mainly summarize the work done by Leroy and Charlaix [26] and by Villey et al. [81]. In both these studies, a spherical probe oscillates in a viscous fluid at frequency ω near an elastic substrate. The sphere has a radius R about few millimeters and the fluid thickness D lies in between few nanometers to few micrometers. A typical setup is shown in Fig. 2.10 and constitutes a dynamic surface force apparatus [82]. In these publications, the derivations provide an expression of the mechanical impedance $\kappa_\omega(D)$ (the ratio between the force and the deformation) which directly quantifies the rheology of the wet contact as a function of the relevant parameters.

As shown in Fig. 2.10, the separation distance $D(t)$ between the sphere and the substrate is given by

$$D(t) = D + h_{0A}cos(\omega t), \tag{2.66}$$

where h_{0A} is the amplitude of oscillation and D is average distance between sphere and

the plane; the experiments and analysis have been performed in the linear regime of small deformation, $h_{0A} << D$.

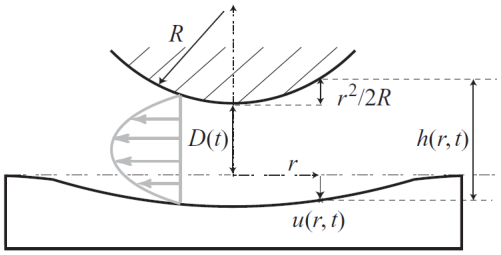

Figure 2.10: Elastic sphere oscillating in front of an elastic substrate, both are separated by an interstitial viscous fluid [26].

According to [26], the mechanical impedance $\kappa_\omega(D)$ is defined as the ratio of the complex amplitude F_ω of the dynamic force $F(t) = \Re[F_\omega e^{i\omega t}]$, acting on the plane at the excitation frequency ω, to the amplitude h_{0A} of the sphere oscillations $h_{0A}\cos(\omega t)$,

$$\kappa_\omega(D) = \frac{F_\omega}{h_{0A}}. \tag{2.67}$$

As to obtain the mechanical impedance in the lubrication regime $D << R$, one considers at first the Reynolds equation, which describes the drainage of the fluid between the sphere and the plane [66],

$$\frac{\partial}{\partial t}[h(r,t)] = \frac{1}{12\mu r}\frac{\partial}{\partial r}\left[rh^3(r,t)\frac{\partial p(r,t)}{\partial r}\right], \tag{2.68}$$

where r is the radial coordinate, $p(r,t)$ is the hydrodynamic pressure and $h(r,t)$ is the fluid thickness. Taking into account the deflection of the elastic plane $u(r,t)$, the fluid thickness is

$$h(r,t) = D + h_{0A}cos(\omega t) + \frac{r^2}{2R} + u(r,t). \tag{2.69}$$

In the linear regime, $h_{0A} << D$, the time-dependent quantities are harmonic functions of the time at the driving frequency. In this case, the relation between the deflection $u(r,t) = \Re[u(r)e^{i\omega t}]$ and the pressure $p(r,t) = P_0 + \Re[\delta p e^{i\omega t}]$ is obtained by linearizing the Eq. 2.68 at first order in h_{0A}, u and δp,

$$i\omega r[h_{0A} + u(r)] = \frac{\partial}{\partial r}\left[\frac{r}{12\mu}\left(D + \frac{r^2}{2R}\right)^3\frac{\partial \delta p(r)}{\partial r}\right], \tag{2.70}$$

where P_0 is the atmospheric pressure, $u(r)$ and $\delta p(r)$ are complex amplitudes.

Within mathematical manipulations [26], one can derive the mechanical impedance in the form

$$\kappa_\omega(D) = \frac{6\pi\mu R^2\omega}{D_c}g_k(D/D_c), \tag{2.71}$$

where

$$D_c = 8R\,(\mu\omega/E)^{2/3} \tag{2.72}$$

is a critical distance above which the elasticity of the sphere is involved (see below in Sec. 2.4.5) and $g_k(D/D_c)$ is a non dimensional function estimated semi-analytically [26].

In the regime where the separation is larger than the critical distance, $D >> D_c$, the Eq 2.71 takes the form

$$\kappa_\omega(D) = \frac{6\pi\mu R^2\omega}{D_c}\left[\frac{9\pi^2}{512}\left(\frac{D_c}{D}\right)^{5/2} + i\left(\frac{D_c}{D}\right)\right]. \tag{2.73}$$

The comparison between the classical lubrication force, Eq. 2.61, and the expression of the mechanical impedance, Eq. 2.73, shows that including an elastic deformation in the Reynolds equation, see Eqs. 2.68 and 2.69, provides a non trivial and nonlinear contribution of the force which is in phase with the deformation, see the first term in brackets in Eq. 2.73. The second term in Eq. 2.73 stands for the classical limit given by Eq. 2.61, in which no elasticity is involved.

When the distance between bodies is smaller than the critical distance, $D \ll D_c$, both the out-of-phase damping contribution (the imaginary part) and the in-phase contribution (the real part) in Eq. 2.71 saturate toward constant values; in this case Eq. 2.71 becomes [26]

$$\kappa_\omega \simeq 1.163(\sqrt{3} + i)\frac{6\pi\mu R^2\omega}{D_c}. \tag{2.74}$$

The asymptotic limits, Eqs. 2.73 and 2.74, have been verified experimentally [81]. The results are summarized in Fig. 2.11: the mechanical impedance describing the elastohydrodynamic interaction depends on the interplay between the elastic characteristics of the sphere (E, R) and the viscosity of the fluid μ.

It is worth mentioning that the mechanical impedance given by Eq. 2.71 can be generalized straightforwardly to the interaction between two spheres (radius R_1 and R_2, Young's moduli E_1 and E_2 and Poisson ratio ν_1 and ν_2), by simply replacing the radius R by its effective value

$$R = 1/(1/R_1 + 1/R_2), \tag{2.75}$$

and the elastic modulus E by

$$E = 1/[(1-\nu_1^2)/E_1 + (1-\nu_2^2)/E_2]. \tag{2.76}$$

2.4.5 Mechanical impedance of a wet contact at large fluid thickness

In this subsection we present a more qualitative derivation of the mechanical impedance κ_ω between the sphere and the substrate, as detailed in [26]. Here, when the fluid's thickness is larger than the critical value, $D \gg D_c$, the hydrodynamic pressure, see Eq. 2.60,

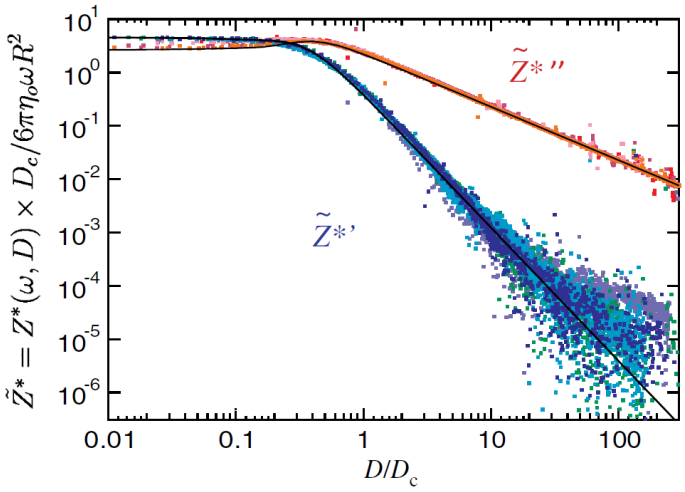

Figure 2.11: Normalized mechanical impedance Z (κ_ω in our notations) as a function of the normalized separation distance D. The elastic part is shown in blue and the viscous part is shown in red [81]. D_c is the critical distance, ω is the angular frequency, R is the radius of sphere and η is the viscosity.

and consequently the elastic deformation can be assumed low enough to decouple the hydrodynamic problem from the elastic problem. For sake of simplicity, one can additionally assume the mechanical response of the substrate as the one of a flat punch [26] of radius $a_w = \sqrt{2RD}$, see for instance Eqs. 2.60 and 2.62. Within these frames, the force exerted by the fluid on the plane being $F = 6\pi\mu\omega h_0 R^2/D$ in this viscous regime, see Eqs. 2.61, the resulting indentation δ_0 becomes,

$$\left(\frac{F}{\pi a_w^2}\right) \propto E\left(\frac{\delta_0}{a_w}\right) \rightarrow \delta_0 \propto \frac{F}{E\sqrt{RD}}. \tag{2.77}$$

One can thus model κ_ω as a spring and dashpot in series to account for the presence of the layer of viscous fluid on top of the elastic substrate,

$$\kappa_\omega \propto \left(\frac{1}{k} + \frac{1}{i\omega\lambda}\right)^{-1}, \tag{2.78}$$

where k is a stiffness,

$$k \propto \frac{F}{\delta_0} \propto E\sqrt{RD}, \tag{2.79}$$

and the strength of the dashpot λ is

$$\lambda \propto \frac{F}{h_0\omega} \propto \frac{\mu R^2}{D}. \tag{2.80}$$

It clearly appears from Eq. 2.78 that a crossover occurs as long as the deformation of the fluid equals the elastic deformation of the solid. This crossover happens at $(\omega\lambda/k) \propto (\delta_0/h_0) \propto (D_c/D)^{3/2} = 1$ where $D_c \propto R(\mu\omega/E)^{2/3}$, see Eq. 2.72. The critical thickness

D_c thus separates a regime where the viscosity prevails, at $D \gg D_c$, and a regime where the elasticity is involved, at $D \ll D_c$.

In the viscous regime, for which $(\omega\lambda/k) \ll 1$, the Eq 2.78 becomes

$$\kappa_\omega(D \gg D_c) \propto i\omega\lambda\left(1 - i\frac{i\omega\lambda}{k}\right) \propto \frac{\mu\omega R^2}{D}\left[i + \left(\frac{D_c}{D}\right)^{3/2}\right]. \tag{2.81}$$

which qualitatively matches the asymptotic limit given by Eq. 2.73 or given by the classical expression of the Reynolds force without elasticity Eq. 2.61, that is

$$\kappa_\omega \propto \frac{i\mu\omega R^2}{D}. \tag{2.82}$$

It is worth mentioning that in agreement with the initial assumption, the elastic deformation remains negligible compared to the imposed motion in the viscous regime, at $D \gg D_c$: $(\delta_0/h_0) \propto (\omega\lambda/k) \ll 1$. On the opposite, when the thickness is well below the critical value, $D \ll D_c$, the mechanical impedance is such that the ratio of its real an imaginary parts tends to a constant, see Eq. 2.74,

$$\Re(\kappa_\omega)/\Im(\kappa_\omega) = \sqrt{3}, \tag{2.83}$$

and so is the ratio between the elastic deformation δ_0 to the imposed motion h_0: $(\delta_0/h_0) \propto (\omega\lambda/k) \sim 1$. Interestingly, this last result demonstrates that the imposed motion is totally accommodated by the elastic deformation of the sphere and the substrate and, consequently, the fluid does not deform anymore. In the regime of very small fluid thickness, the fluid is clamped by its viscosity due to the intense shear rate and shear stress, see Eq. 2.65; this ultimately leads to an elastic confinement of the fluid [81].

2.5 Macroscopic scale: waves in dry and wet granular media

After having analyzed the contact dynamic between dry and wet grains at the microscopic scale, we now focus our attention on the description of the macroscopic scale, well above the size of the particles. Our aim being the description of wave propagation in granular media, the natural macroscopic scale is the wavelength; most of the descriptions given in this section refer to the long wavelength approximation. In this section, we first present a set of experiments which prove that in compressed media, the static force is distributed along heterogeneous paths, the so-called force chains. The waves mainly propagate along these paths. Next, we report on wave propagation in dry granular media, from both the theoretical and the experimental point of view. In particular, we show the ability of waves to probe the microscopic scale of the contact between grains. Lastly, we report on recent experiments concerning wave propagation in wet granular media.

2.5.1 Force distribution in granular media

The first set of experiment concerns three-dimensional granular media. As shown in Fig. 2.12, Mueth [83] measured the normal force distribution in a granular packing under static compression. In this experiment, the static uni-axial force is exerted on random packing of monodisperse glass spheres enclosed in a cylinder. At the bottom of the cylinder the beads under compression leave marks on a carbon paper, whose darkness and area is proportional to the exerted force. Mueth thus demonstrated experimentally that the force acts locally, as shown in Fig. 2.12(a): the marks on the carbon paper are distributed heterogeneously. The statistical analysis shows that the force distribution is nearly uniform for forces below the average force, while it follows an exponential decay for forces larger than the mean, see Fig. 2.12(b). According to their data, such a distribution depends neither on the boundary condition nor on the preparation history of the samples.

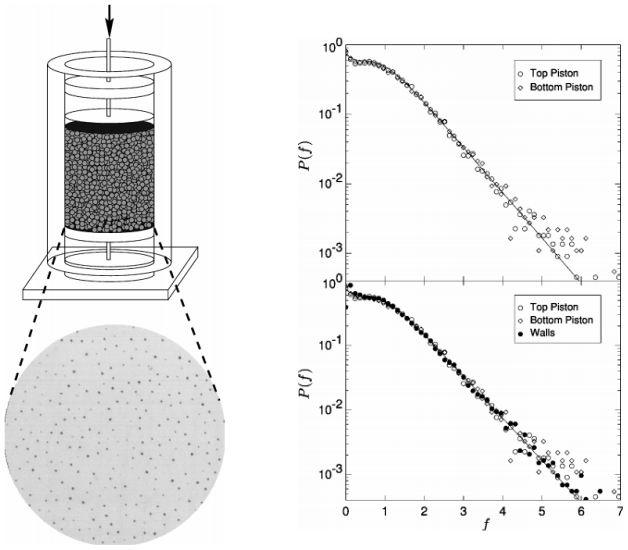

(a) Experimental setup (b) Force distribution

Figure 2.12: (a) The experimental setup where a granular medium is enclosed in a cylinder and compressed by an upper piston. By analyzing the marks on a carbon paper, one can determines the force distribution. By placing a double stick tape on the upper piston and by estimating the net weight supported by the tow walls, (b) one measures the force distribution $P(f)$ in the lower piston, upper piston and in the wall of the cylinder [83]; here f is the normalized force.

The photoelastic technique [84, 85] is also a powerful tool to reveal the intimate nature of the force distribution in two-dimensional granular media. Photoelasticity is based on the property of birefringence [86] and results from refractive indexes that depend on the local mechanical stress. When the light passes through a birefringent photoelastic material, it experiences two refractive indexes, along each of the principal stress directions. This leads to a phase delay between the component of light in these directions and the lag is directly proportional to the stress difference. The phase lag thus affects the

polarization of light. When a photoelastic sample is placed between two perpendicular light polarizers, the whole system is opaque if no stress is applied on the sample. On the opposite, light is transmitted locally, where a stress exists: the map of transmitted light thus reveals the stress distribution in the sample.

For instance, the photoelastic experiments done by Howell [87] in two-dimensional granular media, made of a pile of photoelastic disc, directly shows that the force is distributed along heterogeneous paths, see Fig. 2.13. These force chains are also revealed from the numerical simulations performed by Radjai [88], as shown in Fig. 2.13(c).

These quasi one-dimensional alignments of most compressed and most stiff particles are privileged paths for the propagation of mechanical waves.

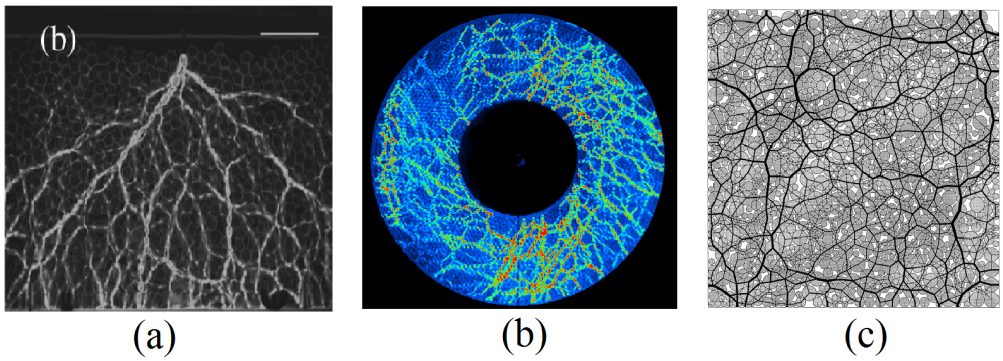

Figure 2.13: Photoelastic pictures of the heterogeneous force chains which support most of the load in compressed granular media. (a) The media is either submitted to a point force [89] or (b) under shear stress [87]. (c) Numerical simulations showing the network of normal forces in polydisperes granular media [88].

2.5.2 Waves as a non intrusive probe of the microscopic scale

As for waves in continuous media, where the wave speed for instance closely relies on the elasticity and the density of the matter, the waves propagating in granular media and through force chains can serve as a non invasive probe of the features at the scale of the grains. Analyzing how waves propagate in a granular medium would likely give an insight into the contact dynamics between grains, revealing the intimate nature of the microscopic scale.

In the seminal works of Liu et al. [3–5] and Jia et al. [6], authors probed the wave propagation in granular media. In Fig. 2.14, we show the experimental setup of Liu [3–5] where a loudspeaker source (S) and an accelerometer detector (D) are placed in a granular medium. One observes that, as the distance increases, the first peak (presumably the ballistic wave that propagates straight from the source to the detector) arrives with a delay and is attenuated. As long as the magnitude of this wave sufficiently decreases, it reveals the presence of late signals. A close inspection demonstrated that reflections on the sides of the container are not responsible for this coda: according to Liu [3–5] the late signal relies on the different paths the sound travels through. The proof comes from

one of their experiment [3], see Fig. 2.14: a heater, which raises the local temperature by only 0.8 K, is embedded in the granular media. The heater dilates when its temperature is increased; it thus exerts local stress and strain in the sample which in turn provokes an abrupt change in the amplitude received on the detector A_d. This observation thus demonstrated that local rearrangements of the grains influence the sound propagation [3]. This interpretation, as well as other results presented in this subsection, is consistent with the fact that wave is carried out along specific paths, the so-called force chains, in granular media [3–5].

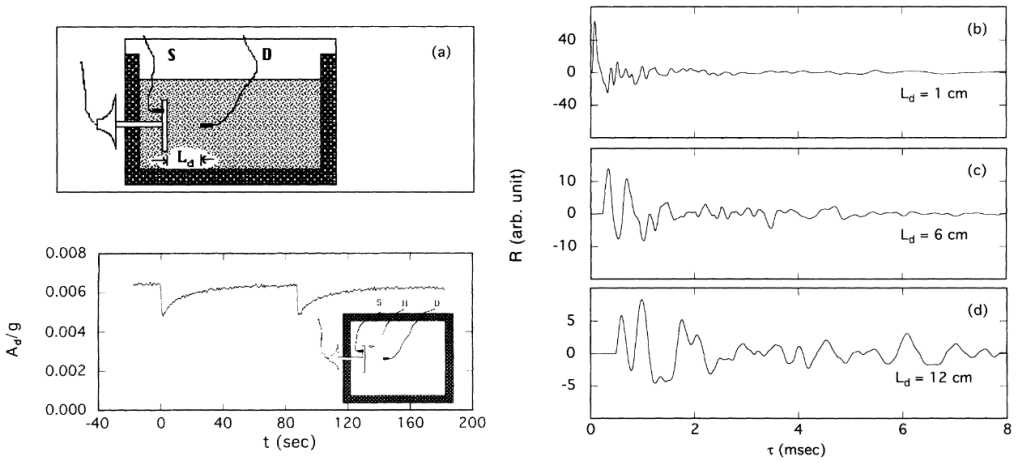

Figure 2.14: (top-left) Experimental setup used to study wave propagation in granular media where S is the source (a loudspeaker), D is the detector (an accelerometer) and L_d is the distance between S and D [3–5]. (right) Response of the samples as a function of time τ for different distance L_d between the source and the detector [3]. (bottom-left) A compact heater H is placed inside the granular media [3], in between the source and the detector: it expands when its temperature is increased. The magnitude A_d of the transmitted acceleration is closely related to the cycles of temperature of the heater: the dilation of the heater generates additional force chains and consequently, a stronger coupling between the source and the detector.

The experimental study of Jia et al. [6] sheds additional light on the intimate nature of wave propagation in granular packing. In [6], Jia et al probed experimentally the wave propagation in glass beads. They observed that the received signal is composed of two distinct parts, see Fig. 2.15. First is a well-defined short pulse E which corresponds to the ballistic pulse. This part is the coherent and reproducible contribution of the signal. It weakly depends on the local arrangements of the grains and in average, it propagates straight from the source to the detector, as through a continuous medium. The ballistic contribution is followed by an incoherent speckle (a coda) which spreads over a long interval of late time; according to Jia. [6], this contribution comes from the multiple scattering of waves, on every particle. The incoherent contribution becomes significant when the wavelength of the incident pulse becomes comparable with the size of the scatterers. This part of the signal is strongly affected by the arrangements of the particles and by the configurations of the force chains.

The analysis of the speckle coming from the multiple scattering of the wave on every grain provides a very rich information and allows reaching a deeper understanding of many mechanisms at the microscopic scale. The coda wave for instance gives information on the nonlinearity of granular media [90] and reveals phenomena such as aging, compaction and even slipping of the microscopic asperities of the grains [91–94].

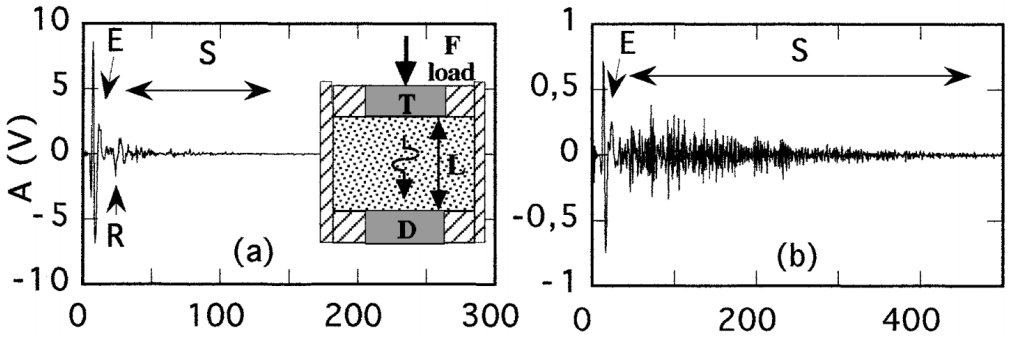

Figure 2.15: Inset (a), an experimental setup [6] for probing wave propagation in granular media made of glass beads. (a,b) The detected signals where one sees the coherent part E and the multiply scattered part S of the signal. Results for glass bead packing with diameter $d = 0.2 - 0.3$ mm (a) and with diameter $d = 0.4 - 0.5$ mm (b), R is the reflected signal and A is the amplitude.

2.5.3 Wave propagation in dry granular media

In this subsection, we report on theoretical and experimental analysis of wave propagation in dry granular media, with the aim to verify how waves are related to the contact dynamics between particles. We start from one-dimensional granular media and we then switch to the case of three-dimensional granular packing.

Waves in one-dimensional dry granular media

Here at first, we consider a one-dimensional chain of spheres under static compression. Under the action of a static force F_0, the spheres deform and approach one to the other by a distance δ_0. The overlap δ_0 between two spheres is strongly confined in a narrow region near the point of contact. This allows to model the system as an alignment of point masses $M \propto \rho R_0^3$ connected by springs whose stiffness $k_H \propto [E_0/(1-\nu_0)]R_0(\delta_0/R_0)^{1/2}$ is given by Hertz potential. Here, ρ is the density, R_0 is the radius, E_0 is the elastic modulus and ν_0 is the Poisson ratio of the spheres. The propagation of a longitudinal plane wave in the chain causes the n^{th} particle to translate by a distance y_n from its equilibrium position. By applying Newton's second law of motion to each of the spheres and by taking into account for a nonlinear Hertz potential interaction between closest neighbors, one obtains [95]

$$M\ddot{y}_n = \kappa\left(\delta_0 + y_{n-1} - y_n\right)^{3/2} - \kappa\left(\delta_0 + y_n - y_{n+1}\right)^{3/2}, \tag{2.84}$$

where $\kappa = E_0(2R_0)^{1/2}/[3(1-\nu_0^2)]$ and $\dot{y}_n$ denotes the derivative in time. In the linear regime, where the dynamic perturbation is smaller than the static overlap,

$$\frac{y_{n-1} - y_n}{\delta_0} \ll 1, \tag{2.85}$$

the Taylor expansion of Eq. 2.84 gives

$$M\ddot{y}_n \simeq (3/2)\kappa\delta_0^{1/2}(y_{n+1} + y_{n-1} - 2y_n). \tag{2.86}$$

Now replacing the displacements by the Taylor expansions $y_{n\pm1} = y_n \pm (2R_0)y_n^{'} + (2R_0)^2 y_n^{''}$ in Eq. 2.86, where $y_n^{'}$ denotes the derivative in space, one finally finds the following equation of propagation

$$M\ddot{y}_n \simeq (2R_0)^2 k_H y_n^{''}. \tag{2.87}$$

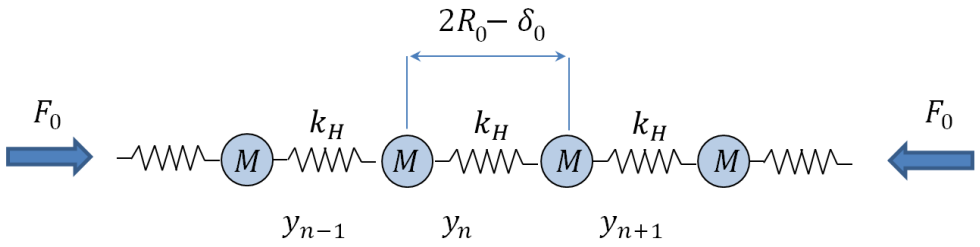

Figure 2.16: One-dimensional force chain of spheres with radius R_0 connected by springs k_H under static compression F_0.

Looking for a harmonic wave solution $y_n(t) = e^{j(\omega t - qx)}$ of Eq. 2.87, where $q = \omega/c_\phi$ is the wavenumber and c_ϕ is the phase velocity, one finds the dispersion relation in the long wave length approximations,

$$c_\phi \simeq (2R_0)\left(\frac{k_H}{M}\right)^{1/2} \propto \left(\frac{E_0}{\rho}\right)^{1/2}\left(\frac{F_0}{E_0 R_0^2}\right)^{1/6} \propto c_0\left(\frac{P}{E_0}\right)^{1/6}. \tag{2.88}$$

As observed in Eq. 2.88, the wave speed c_ϕ nonlinearly depends on the confinement pressure $P = F_0/\pi R_0^2 \propto E_0(\delta_0/R)^{3/2}$ and on the characteristics of the material of the spheres, $c_0 \simeq (E_0/\rho)^{1/2}$, where c_0 stands for the longitudinal wave speed in the bulk material of the spheres. The equation 2.88 clearly shows that the wave speed provides a direct information on the contact dynamics between the grains, quantified by the Hertz stiffness k_H. Measuring the wave speed thus provides a measure of the interaction potential between particles.

The nonlinear power law dependence of the wave speed versus the confinement pressure, Eq. 2.88, has been experimentally probed by Coste et al. [96], where they measured the wave speed as a function of the static force applied in one-dimensional alignments of spheres. As to verify the validity of the Hertz prediction, Eq. 2.88, over a large range of

parameters, they considered several elastic, elasto-plastic or brittle materials with very different surface roughness. In addition to the Hertz potential, their measurements thus allowed the close check of assumptions devoted to explain the few discrepancies observed with waves in real sand; for instance, the incremental bulk modulus of a pile of sand increases as a power law of the confinement pressure, but with a slightly different exponent [9]. The first extension of the Hertz model is due to De Gennes, who proposed two different approaches. The first one accounts for a soft external layer, that may be due to an oxidation of the surface and which may affect Hertz potential [97]. In turn, Goddard intended to account for the effect of the surface roughness as an assembly of microscopic cones [98]; the indentation of a cone significantly differing from the indentation of a sphere. The second extension of De Gennes deals with local plastic deformations at microscopic contacts [99]; a non-Hookean behavior may lead to a different rheology of the contact. However, the main conclusion of Coste et al. is that the Hertz potential fairly predicts the acoustic behavior given by Eq. 2.88 in one-dimensional media, for most materials and independently of the surface roughness of the spheres. Coste et al. found a noticeable exception with brass beads: at large static compression, the wave speed increases faster than the prediction, $c_\phi \propto (P/E_0)^{1/4.5}$. The latter reveals the onset of permanent plastic deformation of the contacts, according to the assumption of De Gennes [99].

Coste et al. also probed the dynamical response of one-dimensional alignments in the nonlinear regime [96,100], without restriction imposed by Eq. 2.85. In this case, the particles are barely touching one to the other, without any static compression. In this regime, the linear wave speed tends to zero: this corresponds to a sonic vacuum [95], in which any perturbation only propagates via nonlinearity. As predicted by Nesterenko [95], nonlinear solitary waves can propagate in such a system. The relation between the wave speed c and the amplitude of the dynamic force F_m of these specific waves follows the Hertz potential prediction, $c \propto F_m^{1/6}$ [95]. The experimental observations conducted in [96,100] at low static compression and high dynamic amplitude provided the same trends as in the linear regime: below the onset of plastic deformation, no significant discrepancies is observable from the prediction given by Hertz potential.

At this point, one can complete the description of wave propagation in dry alignments of particles by addressing the effect of dispersion at high frequency, when the wavelength tends to the size of the particles. The dispersion relation can be found by considering a harmonic plane wave,

$$y_n(t) = y(x = 2nR_0, t) = \exp\left[i(\omega t - qx)\right], \tag{2.89}$$

where $\omega = 2\pi f$ is the angular frequency, $q = \omega/c_\phi - i/l_{att}$ is the wavenumber, c_ϕ is the phase velocity and l_{att} is the attenuation length. Introducing Eq. 2.89 in Eq. 2.86 gives

$$-M\omega^2 \simeq 2k_H[\cos(2qR_0) - 1], \tag{2.90}$$

such that the dispersion relation finally reads

$$q(\omega) = \frac{1}{R_0}\text{asin}\left(\frac{\omega}{\omega_{cut}}\right), \tag{2.91}$$

where

$$\omega_{cut} = 2\sqrt{k_H/M} = c_\phi(\omega = 0)/R_0 \propto c_0/R_0(P/E)^{1/6}, \tag{2.92}$$

is a cutoff frequency. The wave number given by Eq. 2.91 is thus purely real below the cutoff frequency, $\omega \leq \omega_{cut}$, and so are the phase velocity $c_\phi = \omega/\Re(q)$ and the group velocity $c_g = \partial\omega/\partial\Re(q)$: elastic waves propagate and the dispersion relation indeed shows that $c_\phi(\omega) \neq c_g(\omega)$. However, waves are not dispersive in the asymptotic limit $\omega \ll \omega_{cut}$, for which the Eq. 2.91 indicates $c_\phi(\omega = 0) = c_g(\omega = 0) = R_0\omega_{cut}$. The latter exactly matches the result given by Eq. 2.88 and corresponds to the long wavelength approximation: $\lambda = 2\pi/\Re(q) \simeq R_0(\omega_{cut}/\omega) \gg R_0$. In turn, the higher frequency region $\omega \geq \omega_{cut}$ corresponds to a forbidden band, in which the wavenumber becomes purely imaginary, $q = -i/l_{att}$. In the forbidden band, elastic waves do not propagate and any dynamic perturbation generates an evanescent wave.

Waves in three-dimensional dry granular media

From now on, we focus on three-dimensional granular packing. The theory concerning wave propagation in three-dimensional granular media is based on an effective medium in the long wavelength approximation. The effective medium theory (EMT) [101–105] relies on the Hertz-Mindlin [50] contact dynamics. The contact model takes into account for the Hertz potential in the normal direction, via the normal stiffness k_H, and for the tangential stiffness k_t given in Eq. 2.27. The passage from the microscopic scale, at the level of the contacts, to the macroscopic scale, in the long wavelength approximation, provides an estimate of both the longitudinal speed V_p and the shear wave speed V_s from an effective bulk modulus K_e, an effective shear modulus μ_e and an effective density ρ_e. Under the long wavelength approximation, the longitudinal and shear wave speeds are [7–9],

$$V_p = \sqrt{\frac{K_e + 4/3\mu_e}{\rho_e}}, \tag{2.93}$$

$$V_s = \sqrt{\frac{\mu_e}{\rho_e}}, \tag{2.94}$$

where ρ_e is defined as $\rho_e = \rho \times \Phi$, here ρ is the density of the material of the grains and Φ is the compacity, defined as the ratio of volume occupied by the grains to the total volume of the sample. In turn, the effective moduli K_e and μ_e are closely related to the normal and the tangential contact stiffness between spheres, k_H and k_t, on the compacity Φ and on the coordination number Z, which characterizes the average number

of contacts per particles. The bulk modulus reads

$$K_e = \frac{Z\Phi}{12\pi R_0} k_H, \tag{2.95}$$

while the shear modulus is

$$\mu_e = \frac{Z\Phi}{20\pi R_0}(k_H + 3/2k_t). \tag{2.96}$$

In the case of frictionless spheres, the tangential stiffness is zero, $k_t = 0$. The fact that μ_e is non zero with frictionless particles results from the geometrical arrangement of the grains: the normal repulsion between grains indeed induces by itself a shear resistance in a granular sample. Still, it is worth mentioning that the relation between the static force F_0 between grains and the confinement pressure is given by

$$F_0 = \frac{4\pi R_0^2 P}{Z\Phi}, \tag{2.97}$$

and the radius of the contact disc a between two spheres is [7], in terms of the effective parameters,

$$a = R_0 \left[\frac{3\pi(1-\nu_0)}{2Z\Phi G_0} P\right]^{1/3}, \tag{2.98}$$

where R_0 is radius of the spheres, ν_0 the Poisson ratio and G_0 the shear modulus, $G_0 = E_0/2(1+\nu_0)$. As in one-dimensional alignments of spheres, the EMT predicts a nonlinear power law between the confinement pressure P and the wave speed , $V_{p,s} \propto P^{1/6}$, and the wave speed is proportional to the longitudinal wave speed c_0 in the bulk material of the spheres,

$$V_{p,s} \propto \frac{\Phi^{1/3}}{Z^{1/6}} \times c_0 \left(\frac{P}{E}\right)^{1/6}. \tag{2.99}$$

Not surprisingly, the expression given in Eq. 2.99 matches the result obtained in the one-dimensional case, see Eq. 2.88, corrected by the effective values of the compacity Φ and the coordination number Z.

Up to certain extent, the EMT satisfactorily describes the experimental observations under the long wavelength approximation. Makse et al. [8] indeed measured both the longitudinal and the shear wave speed in granular packing as a function of the confinement pressure; the knowledge of V_p and V_s provides a measure of the bulk and the shear moduli. They also performed direct molecular dynamics simulations of these moduli. The confrontation of these measurements, see for instance the Fig. 2.17(a), and the simulations to the EMT show that the prediction given by Eq. 2.93 and Eq. 2.94 reliably renders a nonlinear scaling of the longitudinal and shear velocities as a function of the confinement pressure, $K_e = A_K P^{n_K}$ and $\mu_e A_\mu P^{n_\mu}$. A close inspection of these results demonstrates that both the magnitude A_K and the exponent $n_K \simeq 1/3$ are closely predicted by Eq. 2.95 at low confinement pressure. At larger pressure, weak but noticeable discrepancies arise: the order magnitude of the bulk modulus matches but increases slightly faster that EMT

prediction with the confinement pressure, $n_K > 1/3$. Makse related this discrepancy to an increase of the coordination number [8], i.e. an increase of the overall number of contact, at strong confinement pressure. Things are different for the shear modulus: first, the EMT largely overestimates the magnitude A_μ of the shear modulus and second, it significantly underestimate the exponent n_μ: the shear modulus increases with the confinement pressure faster than predicted. For instance, molecular dynamic simulations shows that $n_\mu \simeq 2/3$ with frictionless particles at very low confinement pressure. The failure of the EMT relies on the nonaffine motion of the grains under shear, due to relaxation mechanisms related to structural disorder, see Fig. 2.17(b). The breakdown becomes dramatic near the unjamming point [106], where a granular medium lose any rigidity and below which the sample would start to flow at infinitely small confinement pressure.

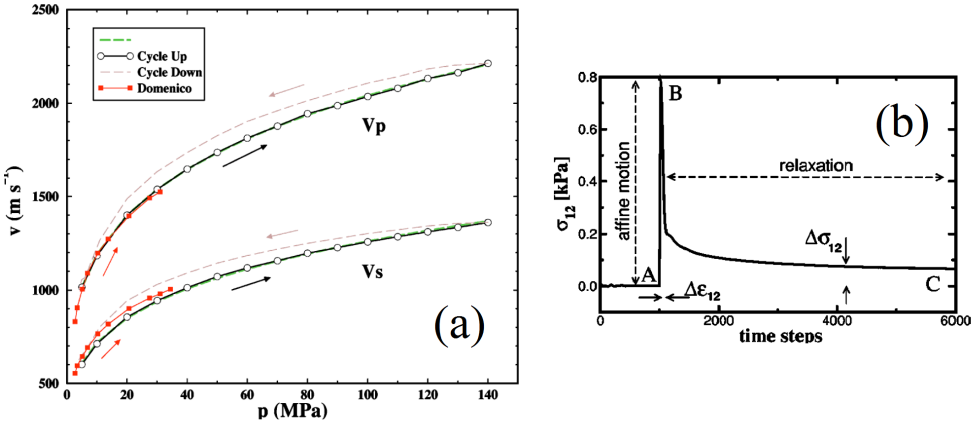

Figure 2.17: (a) Evolution of the longitudinal wave speed V_p speed as a function of the confinement pressure P. (b) The relaxation of the shear stress σ_{12}: the path from points A to B indicates an affine motion while the relaxation takes place B to C.

2.5.4 Wave propagation in wet granular media

There are two type of experiments which quantifies experimentally the wave propagation in wet granular media. The first type of experiments is due to Brunet [10] and later to Griffiths et al. [107]. They both focused on wave propagation in three-dimensional granular media made of polydisperse beads and they closely compared the wave speed measured in dry and wet configurations, as shown in Fig. 2.18. Brunet observed two antagonist effects. One one hand, using fluids with same viscosity but different surface tensions, they observed a slower wave speed in presence of an interstitial fluid, compared to the dry case. This decrease is more pronounced with surfactant with higher surface tensions: they explained this observation by the decrease of the coordination number Z, induced by the capillary cohesion between the grains. On the other hand, using fluids with different viscosities, they observed that the waves in wet granular media are faster

than in the dry configuration. One explanation given by Brunet relies with the increase of the contact stiffness: the presence of a fluid facilitates micro slips of the contacts, which in turn enables a better conformation of the surfaces in contact and an increase of the contact area between grains; the latter would thus increases the contact stiffness.

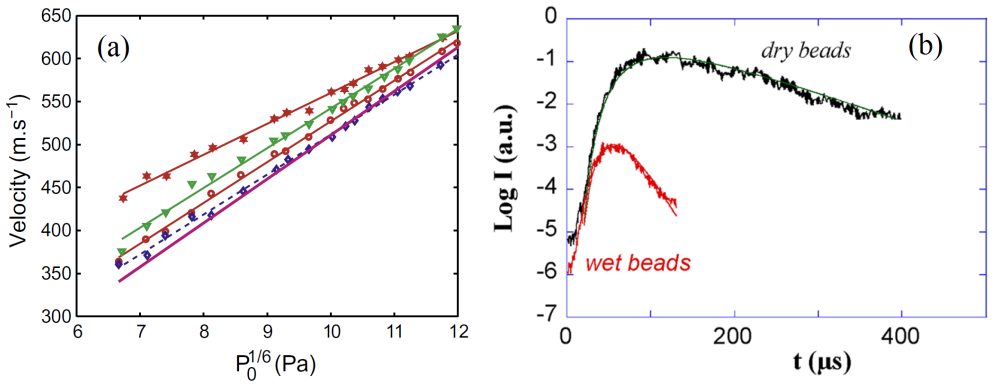

Figure 2.18: (a) Wave speed as a function of confinement pressure: in purple is the Hertz-Mindlin model, in red ∘ a dry configuration, in blue ◊ with water, in green ▽ with an oil with viscosity 50 mPas and in red ⋆ with a fluid with viscosity 10 Pas [107]. (b) Averaged intensity I in dry and wet granular packings: the solid lines stands for fitted models [108].

The second type of experiments concerns the wave propagation in one-dimensional alignments of spheres done by Job et al. [11]. One of the advantage of this type of experiments relies on the known and constant coordination number, $Z = 2$ in one-dimensional media. Here, Job et al. first characterized the dry configuration as a reference case. Next, by adding a very small amount of viscous fluid, they observed the acoustical response of wet granular media. By comparing these two cases, they found that the wave speed could be increased by more than 50% in the presence of very narrow drop of interstitial fluid. Here and contrarily to [10, 107], the increase of the wave speed is solely related to a modification of the contact dynamics between particles. One of the reason invoked to explain such a noticeable increase is related to the occurrence of an elastohydrodynamic interaction [65] between grains, as described in Sec. 2.4. Among other features, this assumption in particular, that we aim to probe in this manuscript.

In any of these cases, the effect of adhesion due to the Laplace force in liquid bridges is not responsible for an overall increase of the confinement pressure at the level of the contacts. Denoting the adhesive force contribution as F_A, see Eq. 2.57, the experiments of Job et al. [11] have been conducted with fluids with a surface tension at about $\gamma_f \sim 20$ mN.m^{-1} and spheres with radius 13 mm: the adhesive contribution, $F_A = 4\pi\gamma_f R \simeq 0.0015$ N (R is effective radius), is negligible compared to the characteristic amplitude of the dynamic perturbations, $F_{ex} \simeq 10$ N. In the experiment of Brunet [10] the fluids with have a surface tension at about $\gamma_f \sim 70$ mN.m^{-1} and the mean radius of the spheres is $R_0 \simeq 350$ μm. In this case, the force of adhesion is again negligible compared to the

static force supported by each bead, $F_0/F_A \sim 500$.

Chapter 3

One-dimensional experimental setup

Contents

In this chapter, we focus on the design and the calibration of the experimental setup. Here, the granular medium consists in a one-dimensional chain of spheres under compression; the alignment is constrained within four rods. The chapter is divided in five parts. In first place, we present our experimental setup. Then, we detail the careful characterization of the elastic properties of the spheres from ultrasonic measurements. Next, we focus on the apparatus used to apply the static compression, in order to check its reliability and stability. Later, we present a set of preliminary experimental results, which reveal the main features of the wave propagation in one-dimensional granular media. Finally, we analyze the experimental frequency response of granular chain, paying a special attention to the limits and the possible pitfalls of our setup.

3.1 Presentation of the experimental setup

The one-dimensional granular media under study consist in alignments of spheres made of either polyacetal or steel, see Fig. 3.1. An alignment of spheres is supported by four rods; these rods are made of either plexiglas or steel. The granular chain is compressed with a static force F_0. From one side, the system is clamped by a piezoelectric actuator, see Fig. 3.2(a), mounted on a massive and rigid piece of steel; the actuator sends dynamic perturbations. From the other side of the chain, the static force F_0 is exerted by a heavy, 5 kg or so, translatable tray shown in Fig. 3.2(b): by translating the tray, one changes the static force applied on the alignment.

Two dynamic force sensors are placed at each extremity of the chain, in contact with the first and the last bead respectively. The first one, on the input side, consists in a light and thin piezoelectric ceramic (used in conjunction with a charge amplifier) glued in front of the piezoelectric actuator and set in contact with the first sphere of the alignment, see Fig. 3.2(a). The second force sensor, on the output side, is a commercial sensor (*Bruel & Kjaer 8230-001*) placed in front of the static force apparatus and in contact with the last sphere, see Fig. 3.2(b). In addition, a static force sensor (*TME F-442*) is placed on the output side, in between the dynamic force sensor and the tray, see Fig. 3.2(b): it provides the direct reading of the static force applied on the chain.

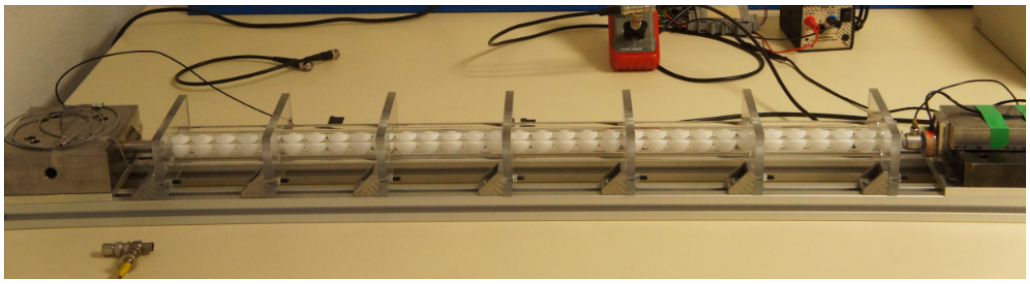

Figure 3.1: Experimental setup, here consisting of 32 identical polyacetal spheres aligned on four plexiglas rods.

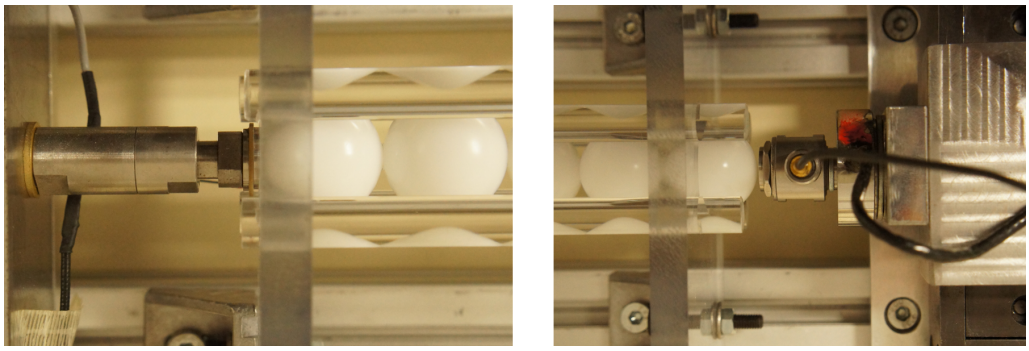

Figure 3.2: Experimental setup: at the left end of the chain, the piezoelectric actuator sends dynamic perturbations which are sensed by a specially designed light force sensor glued in front of it. At the right end of the chain, one sees the dynamic force sensor screwed in front of the static force sensor and the translatable tray.

3.2 Estimation of the characteristics of the spheres

3.2.1 Elastic properties of the spheres

As predicted by Eq. 2.88 the wave speed in a one-dimensional granular medium depends on the radius of the spheres, their mass, their Young's modulus, their Poisson ratio and on the applied static force. The radius and the density of the spheres are easily measurable ($R_0 = 12.5$ mm and $\rho = 1385 \pm 20$ kg.m^{-3} for polyacetal and $\rho = 7785$ kg.m^{-3} for steel) while one probes directly the static force F_0 in our setup. As to determine the Young's modulus E_0 and the Poisson ratio ν_0 of the sphere, we performed ultrasonic measurements in the bulk of their material. On purpose, we cut a flat slab of material from an original sphere in order to achieve these measurements.

These experiments are performed in transmission mode using longitudinal ultrasonic pairs of emitter and receiver centered at 1 MHz (*Panametrics A103S-RB*), 2.25 MHz (*Panametrics V306-SU*), 5 MHz (*Panametrics A109S-RB*) and a pair of shear transducers centered at 0.5 MHz (*Panametrics V151-RM*). The experiments consist in measuring the

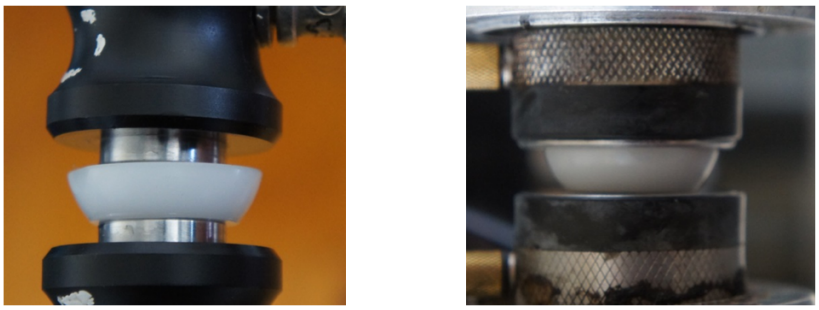

Figure 3.3: Ultrasonic measurements in a slabs of material cut from an original polyacetal sphere placed between two longitudinal transducers (left) or between two shear transducers (right). Both experiments are performed in transmission mode.

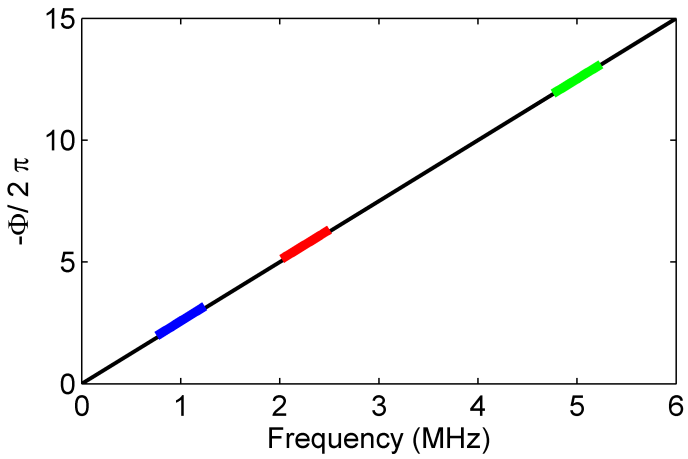

Figure 3.4: Phase delay Φ of the transfer function as a function of frequency for longitudinal waves centered at 1 MHz (blue), 2.25 MHz (red) and 5 MHz (green). The black curve is a guide line showing the linear regression $\Phi = \omega e/c_L$.

phase delay and the attenuation between a reference signal u_{in}, acquired when the emitter is in direct contact with the receiver and a signal u_{out} propagated through a sample of material. The phase delays provide the measure of both the longitudinal and shear phase velocity. The Fig. 3.3 shows a slab of thickness e, cut from an original polyacetal sphere and placed between two transducers.

The longitudinal wave speed c_L and the shear wave speed c_S are estimated from the transfer function between the input and output signals u_{in} and u_{out}, $H = u_{out}/u_{in}$. The phase $\Phi(\omega_c)$ of H near the central angular frequency of the transducers $\omega_c = 2\pi f_c$ serves for the estimation of the wave speed,

$$c_{L,S} = \frac{\omega_c e}{-\Phi(\omega_c)}. \tag{3.1}$$

The estimation of Poisson ratio ν_0 of the spheres is thus obtained as,

$$\nu_0 = \frac{c_L^2 - 2c_S^2}{2(c_L^2 - c_S^2)}, \tag{3.2}$$

and the Young's modulus E_0 is

$$E_0 = \frac{c_L^2 \rho (1+\nu_0)(1-2\nu_0)}{1-\nu_0}. \tag{3.3}$$

We find that polyacetal spheres have a Poisson ratio $\nu_0 = 0.38 \pm 0.02$ and a Young's modulus $E_0 = 4.25 \pm 0.25$ GPa, while steel beads are such that $\nu_0 = 0.29 \pm 0.009$ and $E_0 = 203 \pm 0.46$ GPa.

The bulk attenuation in the spheres is quantified by the loss angle δ; it corresponds to the phase lag between the strain and the stress and is taken into account as a complex Young's modulus $E_\star = E_0 e^{i\delta}$. Assuming weak dissipation, $\delta \ll 1$, the loss angle can be

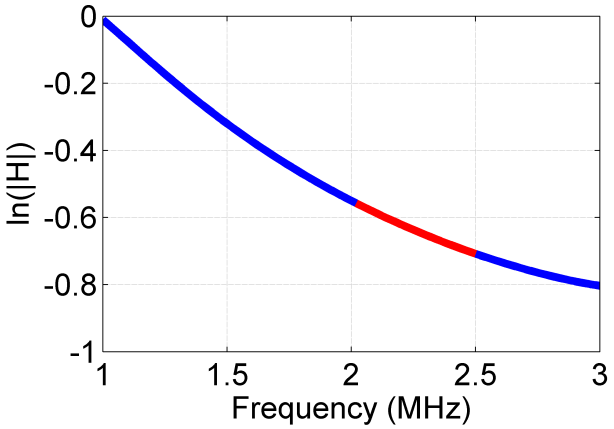

Figure 3.5: Natural logarithm of the modulus of the transfer function versus frequency. The loss angle estimated from Eq. 3.8 near the central frequency (here around 2.25 MHz) of the transducer is shown in red.

estimated from the expression of the longitudinal wave speed,

$$c_L = \sqrt{\frac{E_\star}{\rho}} \simeq \sqrt{\frac{E_0}{\rho}}(1 + i\delta/2) \simeq c_L(1 + i\delta/2). \tag{3.4}$$

According to Eq. 3.4, the longitudinal wavenumber $q = \omega/c_L$ becomes

$$q = \frac{\omega}{c_L}(1 - i\frac{\delta}{2}), \tag{3.5}$$

which, inserted into the expression of a harmonic plane wave for the displacement, $u(x,t) = \exp[i(\omega t - qx)]$, gives

$$u_n(t,x) = \exp\left[i\omega\left(t - \frac{x}{c_L}\right)\right] \times \exp\left(-\frac{\omega\delta}{2c_L}x\right). \tag{3.6}$$

The modulus of the transfer function being

$$|H| = \left|\frac{u_n(x=e)}{u_n(x=0)}\right|, \tag{3.7}$$

the loss angle thus becomes, from Eq. 3.6 and Eq. 3.7,

$$\delta = -ln(|H|)\frac{2c_L}{\omega e}. \tag{3.8}$$

We estimate δ as the mean value of Eq. 3.8 over the central frequency of transducer, see Fig. 3.5: we find $\delta = 0.053 \pm 0.02$ rad for polyacetal and $\delta = 0.023 \pm 0.0074$ rad for steel.

The estimation of the transfer function H between an input signal u_{in} and an output signal u_{out} is performed as follows. First we estimate the Fourier transform of the signals

over the time t, $C_i = \mathrm{FT}_t(u_{in})$ and $C_o = \mathrm{FT}_t(u_{out})$. Then, the transfer function is estimated as the ratio of the average (over multiple repetitions) cross correlation $C_{io} =< C_i^* C_o >$ and the average auto correlation $C_{ii} =< C_i^* C_i > C_{oo} =< C_o^* C_o >$, where C_i^* denotes the complex conjugate of C_i. Thus H read

$$H = \frac{C_{io}}{C_{ii}}. \tag{3.9}$$

and the coherence [109] is defined as,

$$coh = \frac{|C_{io}|^2}{C_{ii} C_{oo}}. \tag{3.10}$$

The coherence shows the similitude between two signals in the frequency domain. When signals are not correlated, for instance if the signal to noise ratio is low, then the coherence falls; in the opposite, the coherence between signals well correlated is close to one. The coherence is used to determine the region of frequency where the measurement of the transfer function is reliable and accurate.

3.2.2 Effect of the solid friction on wave attenuation

In addition to the dissipation of energy due to the deformation of the contacts, see Sec. 3.2.1, the solid Coulombic friction of the particles on their support may participate to the overall attenuation of dynamic perturbation propagating along the alignment. Here, we intend to provide an order of magnitude of the dissipation due to the solid friction.

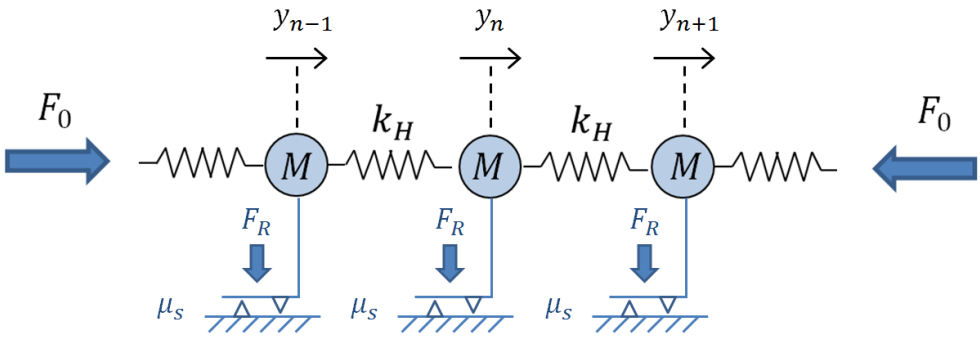

Figure 3.6: An alignment of particles with mass M and radius R_0 interacting via an elastic potential with stiffness k_H. The particles are pressed against the ground with a force F_R, for instance the weight of each particle, and interact with the ground via a Coulomb's coefficient of friction μ_s.

We consider a chain of particles with mass M and radius R_0 interacting via an elastic potential, with stiffness k_H. Every particles slide on a ground surface an we define a solid friction coefficient μ_s. We assume that a radial force F_R is exerted between the particles

and the ground (for instance due to the weight of the particles, or due to the buckling of the alignment when the particles are compressed in the axial direction, see below). Now let's assume that a perturbation comes from the left side in Fig. 3.6: the dynamic force at contact n is $\widetilde{F}(n) = k_H(y_n - y_{n+1})$, the potential energy is $U_P(n) = k_H(y_n - y_{n+1})^2/2$ and the kinetic energy of particle n is $U_K(n) = M\dot{y}_n^2/2$. Since the interaction potential between particles is elastic, then the total energy is $U_{tot}(n) = U_P(n)+U_K(n) = 2U_P(n) \simeq |\widetilde{F}(n)|^2/k_H$, where $|\widetilde{F}(n)|$ is the magnitude of the force. As long as the magnitude of the dynamic force is smaller than the Coulomb's force of friction, $|\widetilde{F}(n)| \leq \mu_s F_R$, then the particle n sticks to the ground. As soon as the perturbation exceeds the frictional force $|\widetilde{F}(n)| > \mu_s F_R$, then the particle n slips and loose part of the incident energy and momentum. In the latter case, for a perturbation going from left to right in Fig. 3.6, the decay of the total energy from sites $n-1$ to n is equal to the work done by the frictional force at particle n,

$$U_{tot}(n) - U_{tot}(n-1) = -\mu_s F_R y_n, \tag{3.11}$$

or else, from the difference between three particles,

$$U_{tot}(n+1) + U_{tot}(n-1) - 2U_{tot}(n) = \mu_s F_R(y_n - y_{n+1}), \tag{3.12}$$

which can be rewritten in term of the magnitude of the traveling force,

$$|\widetilde{F}(n+1)|^2 + |\widetilde{F}(n-1)|^2 - 2|\widetilde{F}(n)|^2 \simeq \mu_s F_R|\widetilde{F}(n)|. \tag{3.13}$$

Introducing an attenuation length l_f such that $|\widetilde{F}(n+1)|/|\widetilde{F}(n)| = e^{-2R_0/l_f}$, then the Eq. 3.13 gives

$$e^{-4R_0/l_f} + e^{+4R_0/l_f} - 2 = 2\sinh^2\left(\frac{2R_0}{l_f}\right) \simeq \frac{\mu_s F_R}{|\widetilde{F}(n)|}, \tag{3.14}$$

which, assuming weak frictional dissipation $l_f \gg 2R_0$, finally gives

$$\frac{l_f}{2R_0} \simeq \sqrt{\frac{2|\widetilde{F}(n)|}{\mu_s F_R}}. \tag{3.15}$$

From the practical point of view, if $F_R = Mg$ corresponds to the weight of a polyacetal sphere, $M \simeq 10.9$ g, and assuming a perturbation with amplitude $|\widetilde{F}(n)| \sim 0.5$ N and a coefficient of solid friction $\mu_s \sim 0.1$, one finds a rough estimation for the attenuation length due to friction

$$\frac{l_f}{2R_0} \sim 10. \tag{3.16}$$

It is worth mentioning that the Eq. 3.15 is valid only when the particles slip, i.e. if $|\widetilde{F}| > \mu_s F_R$. If the particles stick to the ground then no frictional dissipation occurs.

3.3 Design and calibration of an embedded dynamic force sensor

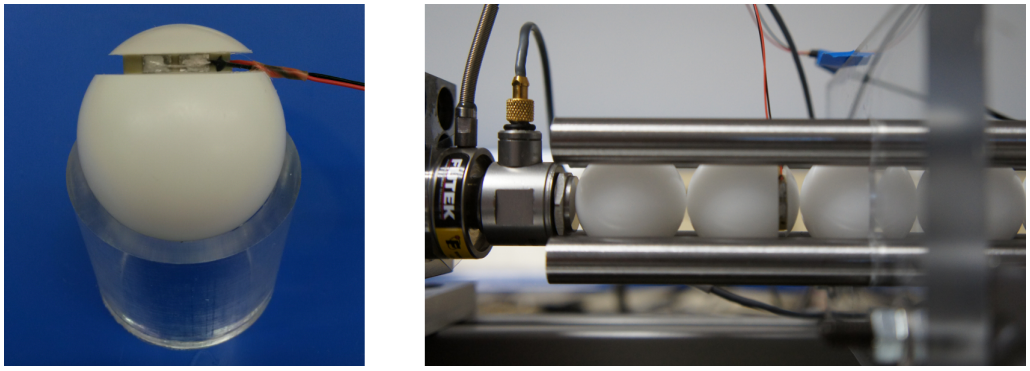

Figure 3.7: Experimental setup. (left) Embedded dynamic force sensor: a piezoelectric ceramic is glued between two caps cut from a 25 mm in diameter polyacetal sphere. (right) The sphere with embedded sensor can replace any particle in an alignment and allows precise measurement of the dynamic force as a function of time and position in the chain.

As to measure the dynamic force that propagates inside our alignments of spheres, we specially designed a non-intrusive instrumented particle. This particle consists in a 2 mm thin and 12.5 mm in diameter piezoelectric annular patch glued in between two caps cut from an original sphere, as shown in Fig. 3.7. The electrical charge generated by the piezoelectric patch is proportional to the dynamic force exerted on the direction perpendicular to the patch and the signal is conditioned by a separate charge amplifier and then amplified. The total mass of the device matches the mass of an original sphere up to a good precision. In addition, the contact mechanics is preserved: the thinnest cap is few millimeter thick, well larger than the penetration depth of the deformation near a contact between particles, see Sec. 2.3. Both the inertia and the elasticity of the instrumented particle thus reliably match the features of an original sphere.

The sensor is calibrated as follows. We place the embedded sensor in direct contact either with the dynamic force sensor glued on the piezoelectric actuator, or with the dynamic force sensor on the output extremity of the alignment. The alignment is made of 40 polyacetal particles under moderate compression. In both cases, we excite the system with a chirp between 50 Hz and 4 Hz and we estimate the transfer function between the embedded sensor voltage (via the charge amplifier) and the reference sensor. This provides a measurement of the sensitivity of the embedded sensor. The ratio $H(\omega) = |H|e^{j\phi}$ between the dynamic force measured by the embedded sensor to the dynamic force measured by the reference sensors is presented in Fig. 3.8 as a function of frequency. These results demonstrate the reliability and the robustness of the embedded sensor: it provides a fairly constant sensitivity and no phase shift over the whole frequency range of interest.

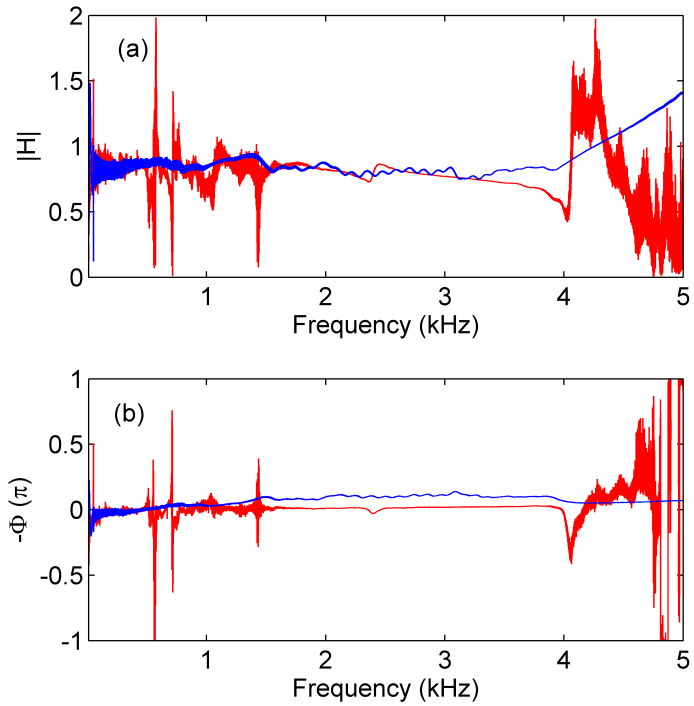

Figure 3.8: Transfer function $H(\omega) = F_{emb}/F_{ref}$ between the signals acquired by the embedded sensor and the reference dynamic force sensor F_{ref}, where $F_{ref} = F_{in}$ is the dynamic force sensor in front of the piezoelectric actuator (the blue curve) and $F_{ref} = F_{out}$ is the dynamic force sensor on the output side (the red curve). Results are shown in modulus (a) and in phase (b) as a function of frequency.

3.4 Characterization of the static loading apparatus

Here, we describe in details the apparatus used to apply a static load F_0 on the alignment. In particular we will analyze its accuracy, reliability and mechanical stability. Due to the friction between the spheres and their supports (the aligning rods), one can infer that the static force F_0 is not homogeneously distributed along the chain. For instance, the beads near the extremity, where the static force is applied, may be more compressed than the spheres in the central part or at the other side of the alignment. The latter depends on the way the static force is prescribed and issues can be bypassed by first applying a value that exceeds a given set point, before slowly decreasing it until reaching a final desired value. In all cases, the stabilization of the static force depends on a relaxation time related to micro slips of the grains on their supports.

As to quantify these influences, we perform two sets of experiments. For these experiments, we use a granular chain of 40 polyacetal spheres supported by four steel rods. In the first set of experiments, following a *protocol (A)*, the chain is compressed at a given value of the static force (10 N, 20 N, 30 N and 40 N) for about 5 minutes. During this time, we observe the evolution of the force registered by the static force sensor as a func-

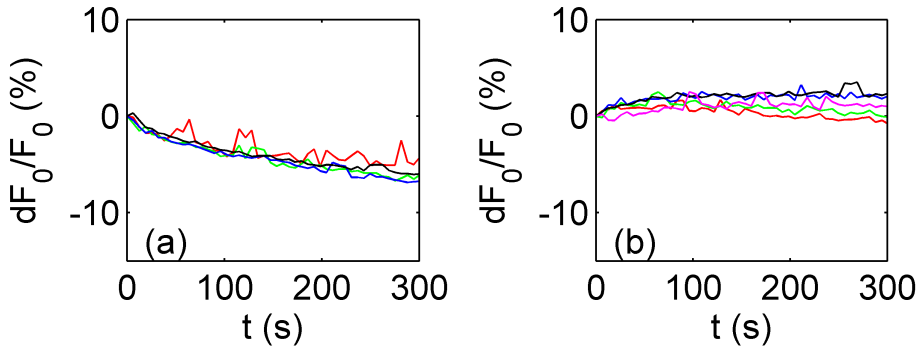

Figure 3.9: Relative decay of the static force F_0 measured as a function of time t. (a) Protocol 1A: temporal evolution of the static force from set points 10 N, 20 N, 30 N and 40 N in red, green, blue and dark respectively. (b) Protocol 1B: temporal evolution of the static force at 20 N after having waited 1 min, 2 min, 3 min 4 min and 5 min in red, green, blue, dark and magenta respectively at the static force of 40 N. Here, the system is not excited by a dynamic signal.

tion of time. In the second type of experiments, following a *protocol (B)*, one compresses the chain with a static force at 40 N up to 5 minutes. Then this force is decreased to 20 N, while we record the time evolution of the static force during 5 more minutes.

In addition, these two protocols are done via two different variants, in order to probe the occurrence of micro slips of the grains on their support. Following the protocol of Espindola [93], we set the dynamic actuator either on or off while loading and unloading the chain. In the *protocol (1)*, one does not send any dynamic signal in the alignment. In the *protocol (2)*, a chirp of 1 s duration is sent every 5 s by the actuator. The chirp signal has a large frequency range (100 Hz to 6 kHz) and has a rather large magnitude.

Experimental results for both protocoles (1) and (2) are traced in Fig. 3.9 and in Fig. 3.10, in which both protocols (A) and (B) reveal the temporal evolution of the static force. The results from the protocols (1A) and (1B) are traced on the Fig. 3.9. Here at time $t = 0$, the compression is concentrated at the beginning of the chain, where one applies and measures the static force. At longer time, the static force starts to redistribute along the chain, due to micro slips at the level of the contact [91, 93]. This homogenization of the compression results in the decay (in A) or an increase (in B) of the force measured at the extremity as a function of time t. Comparing protocols (1A) and (1B), one observes that the relative evolution of the static force are comparable, $dF_0/F_0 \sim 3-5\%$, within the same duration. The latter suggests that the relaxation time is controlled by the same process, no matter the static load is increased or decreased.

In the protocols (2A) and (2B) in which one sends intermittent chirps, the temporal evolution of the force is more pronounced, see Fig. 3.10(a). One expects here to reach a homogeneous compression more quickly: applying a dynamic perturbations facilitates micro slips of the beads at the level of asperities [91, 93], which in turn boosts the homogenization of the force.

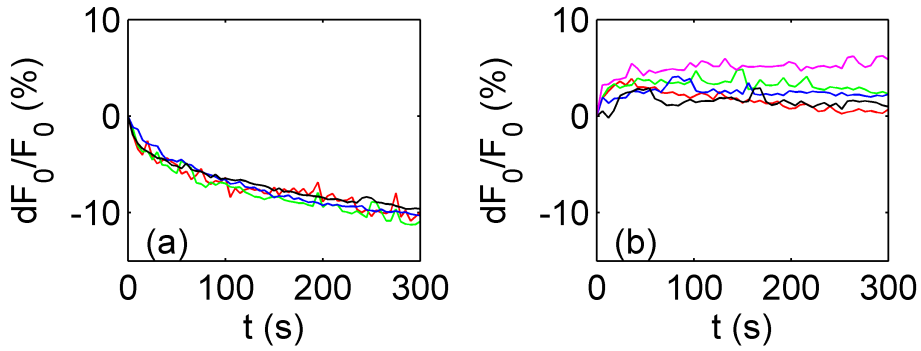

Figure 3.10: Relative decay of the static force F_0 measured as a function of time t. (a) Protocol 2A: temporal evolution of the static force from set points 10 N, 20 N, 30 N and 40 N in red, green, blue and dark respectively. (b) Protocol 2B: temporal evolution of the static force at 20 N after having waited 1 min, 2 min, 3 min 4 min and 5 min in red, green, blue, dark and magenta respectively at the static force of 40 N. Here, the system is intermittently excited by a broad frequency range chirp with a rather large amplitude.

In the protocol (2) and experiment (b), one observes that the dynamic solicitation of the system has almost no impact on the convergence of the force, compare for instance the results shown in Fig. 3.9(b) and in Fig. 3.10(b). Indeed, if the static force is increased up to 40 N, as in the previous case, F_0 is concentrated in the region at the beginning of the chain. Along the chain, the force is smaller than the compression applied at the extremity. However, there exists regions (maybe even the whole chain), where the static force is yet above 20 N. Decreasing then the set point down to 20 N at the extremity, from this higher state, let the chain in a more stable arrangement: the applied static force is homogeneously distributed along the chain. So far, the solicitation of the signal does not change further the configuration of the particles on their support. This differs from the cases shown in Fig. 3.9(a) and Fig. 3.10(a), where the beads are in metastable positions and where the dynamic signal alters these configurations.

When it comes to the stability and the convergence of the applied static force, the best way to perform experiments is thus to protocol (1B), by overloading the set point and without dynamical solicitation; the latter having no significant effect on the practical point of view. However the method (B) has a pitfall at the highest static loads, since the onset of plastic deformation may easily be reached while preparing the system. In order to bypass this limit, we tested a *third protocol (C)* which consists in applying a set point at the desired value of the static force and then in facilitating the homogenization by accommodating the micro displacements of the beads by hand at random locations.

As for the protocols (A) and (B), the stability of the static force is tested by following the temporal evolution of the static force at 20 N for 5 minutes, while driving or not a dynamic solicitation. The experimental results are traced in Fig. 3.11. With this method one obtains a relative decay which is comparable but slightly more regular and more repeatable than the original protocol (A) and (B). Taking into account that the

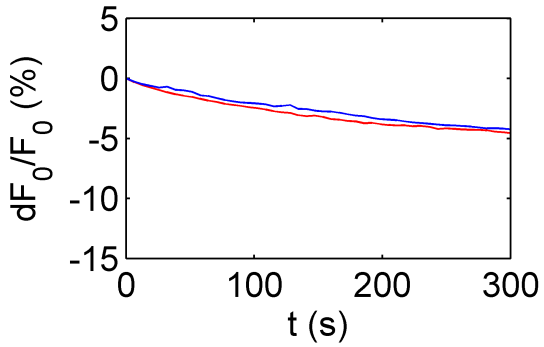

Figure 3.11: Relative decay of the static force as a function of time t with experimental protocol C, for a 20 N static force and during 5 min. In red, the response without solicitation (protocol 1C), in blue the response with solicitation (protocol 2C).

protocol (C) helps avoiding any onset of plastic deformation at large static force as in the protocol (B), we chose to retain it as the conventional way to set our alignments of spheres under compression, without any dynamical solicitation.

3.5 Preliminary results: observation of a band structure

After having evaluated the elastic properties of the sphere and quantified the stability and the homogeneity of the static compression, we here perform our first experiments concerning wave propagation in one-dimensional chains. For this, we excite the medium with the piezoelectric actuator on one of its extremity and we measure the output signal at the other side. The transfer function and the coherence between the input and the output is estimated according the method described in Eq. 3.9 and Eq. 3.10.

In what follows, we use two different types of signals to excite the system: long duration chirps or short duration, time resolved, gaussian pulses. On one hand, owing to their high energetic content, the broad band chirp signals allow probing efficiently the frequency response of the system with a very good signal to noise ratio. However, their long duration does not allow discriminating the incident waves from their reflections. On the other hand, owing to their short duration, gaussian pulses centered at particular frequency allows distinguishing any delayed reflected waves in transmitted signals: one can thus truncate these contributions to obtain unambiguous information of the wave speed or the attenuation.

In this first set of experiments, we send a chirp along granular chain of 32 polyacetal spheres supported by four plexiglas rods with length $L = 0.8$ m. The estimation of the cutoff frequency $f_{cut} = 2\sqrt{k_H/M}/2\pi$, see Eq. 2.92, in an alignment of polyacetal spheres under a static compression ranging from 5 N to 40 N indicates that f_{cut} lies in between 3 kHz and 4.5 kHz. We thus chose a chirp signal with frequency going from 10 Hz to 7.5 kHz as to reveal the whole propagative band and part of the forbidden band.

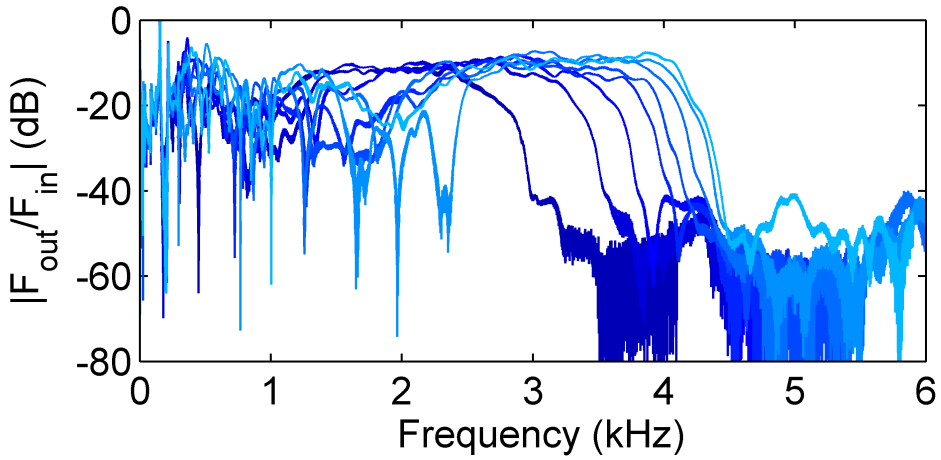

Figure 3.12: Modulus of the transfer function between the force measured at the beginning F_{in} and at the end F_{out} of the chain as a function of frequency. Different colors correspond to different applied static forces F_0. Here, the spheres are in polyacetal and the rods are in plexiglas.

It is worth mentioning that the maximum value of F_0 remains below the onset of plasticity; according to von Mises criterium [50], the onset of plastic deformation is $F_p \sim 45$ N for 25 mm in diameter polyacetal spheres and $F_p \sim 350$ N for steel spheres with same radius. Additionally, as to fulfill the condition of a linear regime, see Eq. 2.85, the amplitude of the chirp signal is chosen so that it does not exceed 1 N, well below the imposed static force.

In a first attempt, we acquire the transfer function between the force at the beginning $F_{in}(t)$ and at the end $F_{out}(t)$ of the chain. The experimental results are traced on Fig. 3.12. In Fig. 3.12, the modulus of the transfer function $|F_{out}/F_{in}|$ shows that above a cutoff frequency f_{cut}, in between 3 kHz and 4.5 kHz, the transmission is strongly attenuated: one observes a pass band at low frequency and a forbidden band above the cutoff frequency. Additionally, one sees that the cutoff frequency increases with the static compression. These results appear in qualitative agreement with the theoretical description given in Eq. 2.91 and Eq. 2.92.

Finally, by focusing on the low frequency region, around 1-2 kHz, one distinguishes a slight attenuation of the transmitted signal. At even lower frequency, around 0.1-0.5 kHz one also remarks peaks of transmission and possibly resonances. These two phenomena are not predicted by the model derived in Eq. 2.91. In the following sections and chapters, we focus our attention on the identification of the observations at low frequency, below 2 kHz.

3.6 Preliminary analysis of the response of granular chains

3.6.1 Analysis of the low frequency attenuation: elasto-frictional coupling between the spheres and the supports

At first, we focus on the source of attenuation encountered in the low frequency range between 1 kHz and 2 kHz, where a cutoff frequency appears in the transfer function. Here and in the following, we denote this low frequency cutoff as f_0. Interestingly, f_0 depends on the static force F_0. As to quantify this behavior in more details, we performed experiments within different configurations corresponding to different combinations of materials of the spheres (polyacetal or steel) and of the supporting rods (plexiglas or steel). Here, the frequency response of all alignments are achieved by using the same chirp signal and the same range of static forces as in Sec. 3.5.

The results for each configurations are presented in Fig. 3.13. The Fig. 3.13(a) corresponds to the transfer functions at different static forces in an alignment of polyacetal spheres clamped between four plexiglas rods, the Fig. 3.13(b) is for polyacetal spheres with steel rods and the Fig. 3.13(c) stands for steel spheres with steel supports.

In all the configurations presented in Fig. 3.13, one clearly observes the low cutoff frequency f_0 below which an attenuation is more pronounced. For the configurations presented in Fig. 3.13(a) and (b), f_0 depends on the static compression F_0, while it appears almost constant in the configuration shown in Fig. 3.13(c). On one hand, the low frequency cutoff thus depends on the specific materials of the sphere and of the rods. In another hand, f_0 depends on the combination of materials; it thus stands to reason that the underlying mechanism may rely on an interaction between the two.

As to gain further information on these observations, we performed additional experiments, which are summarized in Fig. 3.14. Here, the static force is applied in a cyclic way, first by increasing F_0 by steps of 5 N, from 5 N to 40 N, and then by decreasing it, down to 5 N. The procedure is then repeated twice to check the reproducibility. For each value of the static force, one estimates the transfer function and the low cutoff frequency f_0, measured at -20 dB below the average level of the propagative band. As shown in Fig. 3.14, the cutoff f_0 increases with the static force F_0 and experiences a slight but noticeable non-repeatability if not a hysteresis. The latter is compatible with the occurrence of solid friction between the spheres and their supports, which may likely introduce a hysteretical response depending on stick/slip regimes for instance. At this point, one can derive an assumption on the mechanism leading to the occurrence of the low cutoff frequency and of a low frequency region of noticeable attenuation. If the solid friction is involved, the spheres can stick to the rods, and as long as the low frequency cutoff f_0 depends on the elastic properties of both materials in contact, then the low frequency cutoff may results from an on-site elastic interaction between the two. As we will see in the next third chapter, including such a local elastic interaction in a lattice indeed induces a forbidden band gap at zero frequency, in agreement with our observations.

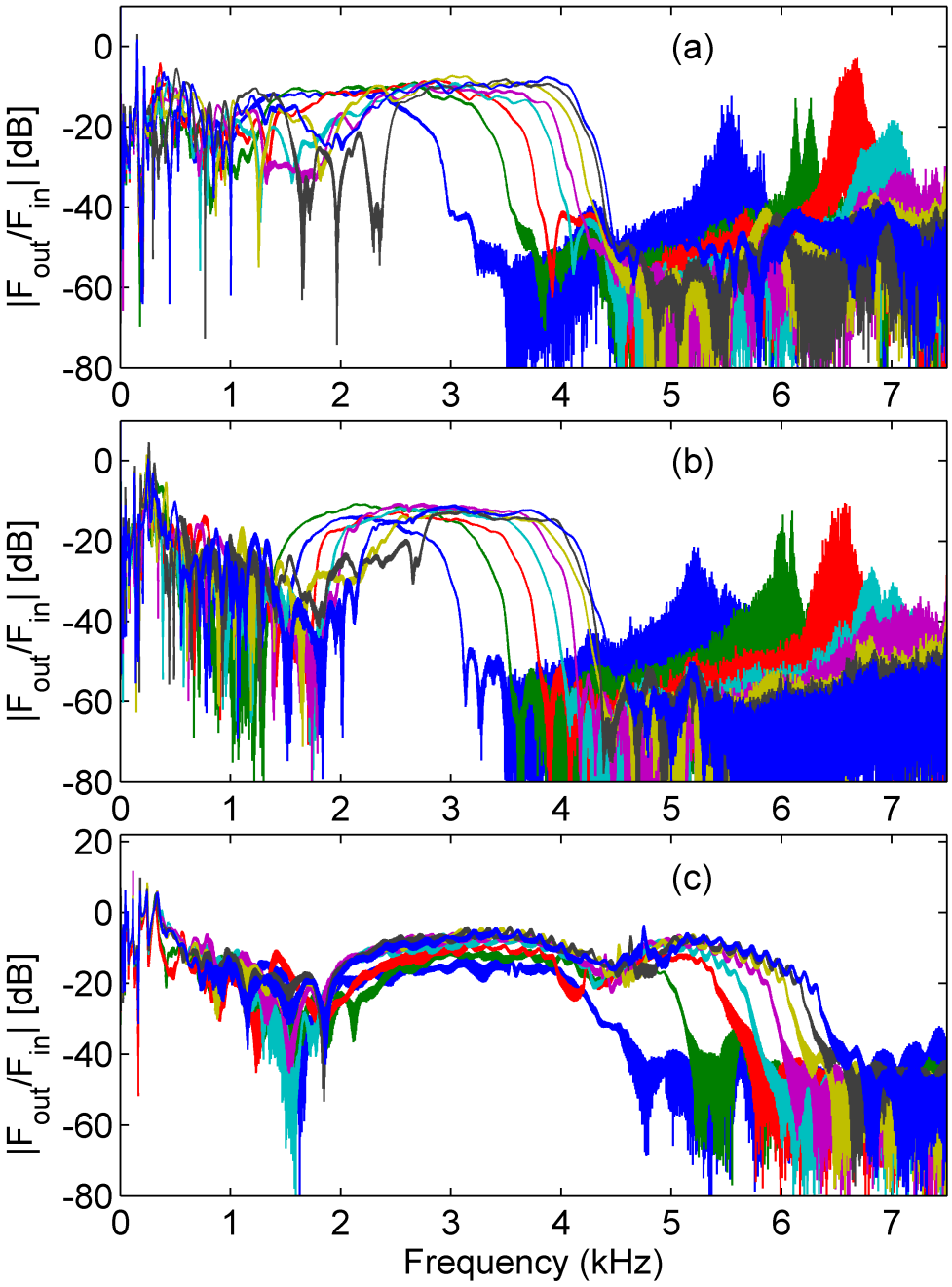

Figure 3.13: Modulus of the transfer function, for dry chain between the output signal F_{out} and input signal F_{in} as a function of frequency; different colors show different static force applied F_0 ranging from 5 N to 40 N every 5 N. (a) The results for configuration with polyacetal spheres and plexiglas supports, (b) polyacetal spheres and steel supports and (c) steel spheres and steel supports.

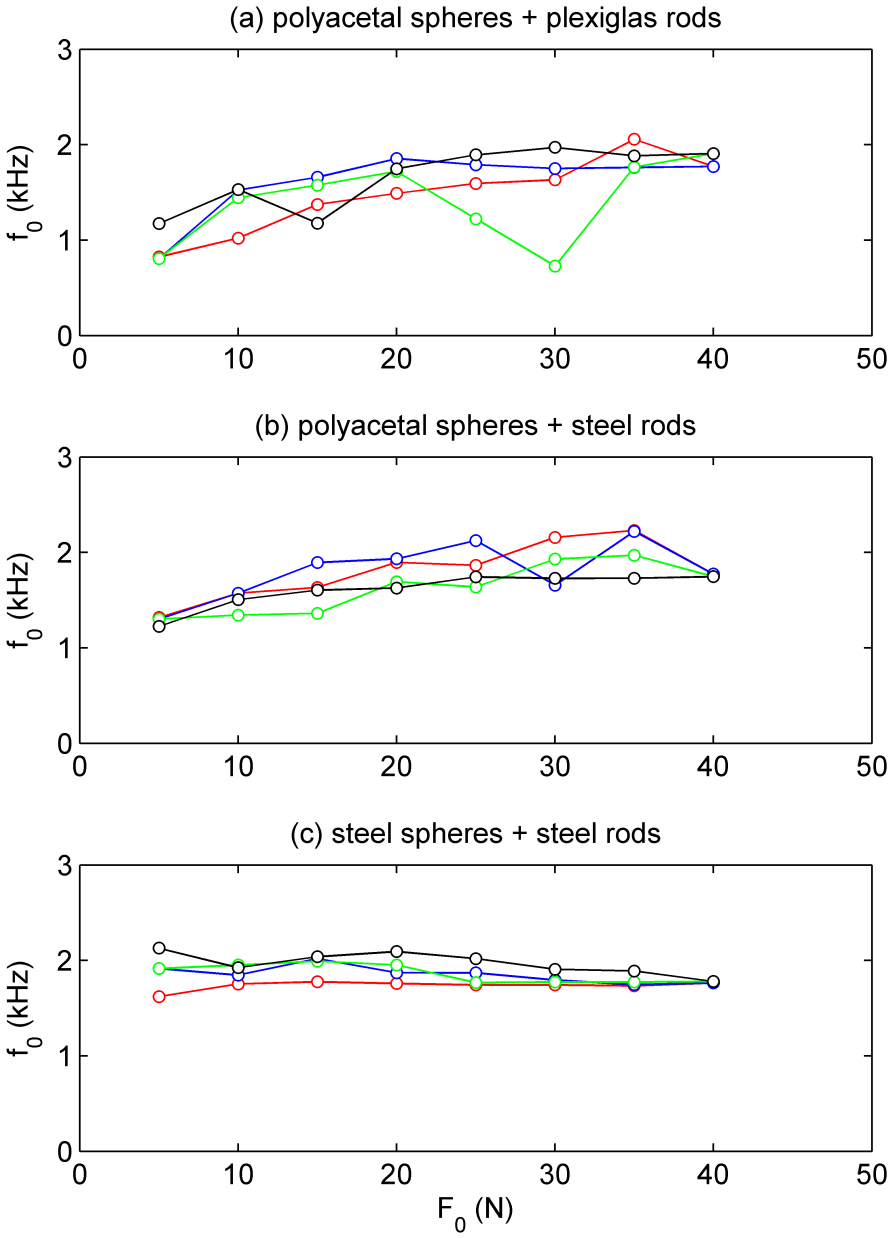

Figure 3.14: Low cutoff frequency f_0 estimated at -20 dB below the average value of the propagative band (see Fig. 3.13). (a) Polyacetal spheres with plexiglas supports, (b) polyacetal spheres with steel supports and (c) steel spheres with steel supports. The red curves correspond to the first increase of the static force, from 5 N to 40 N, the blue curves to the first decrease, from 40 N to 5 N, the green curves to the second increase and the black curves to the second decrease.

3.6.2 Analysis of the resonant peaks at very low frequency: spurious resonances and bending waves in the support

Having quantified the interaction between the spheres and their supports, here we focus on the peaks of transmissions observed in the transfer function at very low frequency, between 100 Hz to 500 Hz, see Fig. 3.12 and Fig. 3.13. Possible sources of these observations may result from resonances of the experimental setup. As to identify these sources, we ruled out any possible contributions, starting from the resonances of the table on which stands the setup, resonances of individual mechanical parts of the setup (mainly the apparatus used to apply the static force) or resonances of the rods.

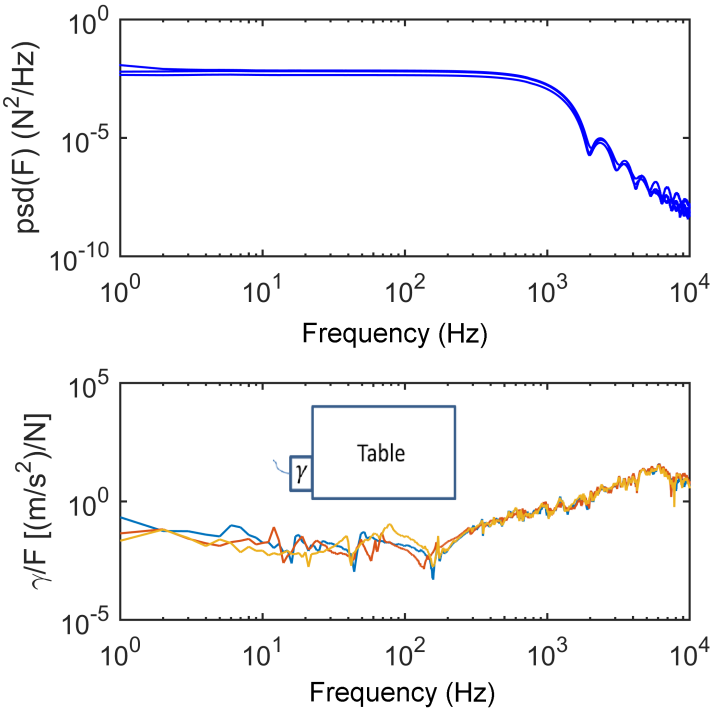

Figure 3.15: (a) Power spectral density of the force measured with an impact hammer while kicking the table on which stands the setup. (b) Acceleration γ measured by an accelerometer glued on a side of the table. (b) The different colors show different experimental conditions: in blue the hammer kicks the table as is, in red a 40 kg mass is set on top of the table and in yellow the table is firmly constrained against a wall. The inset shows a sketch of the experiment (b).

We here first check eventual resonances of the table. The frequency response of the table is probed, as is, by kicking it with an impact hammer, instrumented with a dynamic force sensor, and by recording the lateral acceleration. The attempt is repeated by putting a heavy mass of 40 kg on top of the table: any resonance mode should be shifted toward lower frequency regions. Finally in a third attempt, the table is firmly constrained against a wall, with the hope that it would stiffen the system and shift any

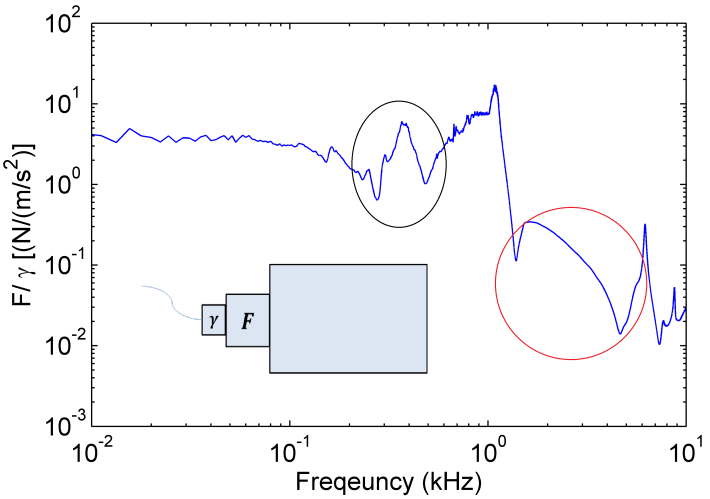

Figure 3.16: Modulus of the transfer function between the acceleration γ captured by an accelerometer glued on the static force sensor and the force F recorded by an impact hammer. One can observe resonances near 280 Hz and 470 Hz and anti-resonance near 380 Hz (see inside the black circle). Inside the red circle, resonances are observed in the 1-5 kHz frequency region. In inset, a sketch showing the experimental configuration.

resonant frequency toward high frequency region.

The transfer functions between the acceleration and the force sensor of the impact hammer are presented in Fig. 3.15 all three configurations. In any of the configuration, no clear peaks of resonance appear in the frequency range of interest, 0.1-0.5 kHz. As a consequence, one can conclude that the table is not responsible for the peaks observed in the response of the media at very low frequency.

Next, we probe the mechanical response of the device used to apply the static force. Possible artifacts may result from the fact that this apparatus is made from the assembly of a fairly rigid dynamic sensor screwed on a rather soft static force sensor. The assembly would therefore likely present one resonant peak. In addition, the whole apparatus is placed on a heavy, 5 kg or so, translation tray: thanks to inertia, the extremity does not recoil when reached by a high frequency dynamic perturbation. The mechanical response of this subsystem is probed by gluing an accelerometer in front of the dynamic sensor and by kicking the subsystem with the impact hammer. The results are presented in Fig. 3.16.

Firstly, we focus on the frequency range below 500 Hz, where we observe a peak at about 280-470 Hz, see the black circle in Fig. 3.16. The comparison between the transfer functions of the static force apparatus in Fig. 3.16 and the transfer function of an alignment in Fig. 3.17 - another realization similar to Fig. 3.12 and Fig. 3.13 but with a lot more averaging - shows that the peak does not match all the resonances observed in the transfer function of the chain of spheres. Although the resonance at 280-470 Hz may participate to the overall mechanical response of the setup, it does not explain the entire frequency spectrum of the alignments below 500 Hz: we thus exclude this part

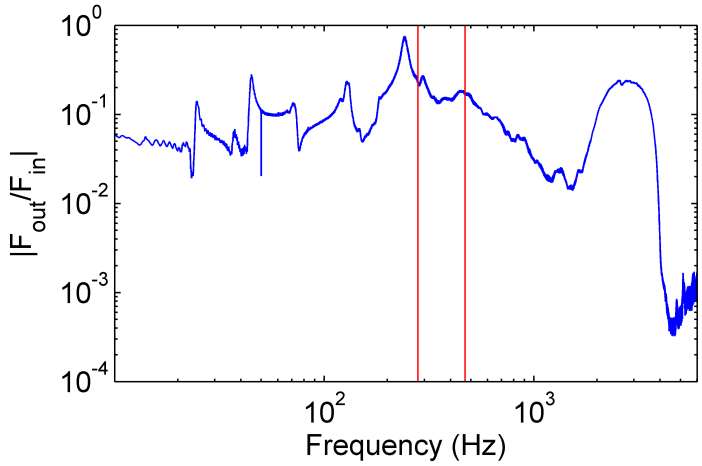

Figure 3.17: Modulus of the transfer function between the signal measured at the beginning F_{in} and at the end F_{out} of the chain as a function of frequency, under 20 N static compression. Here, the configuration is an alignment of polyacetal spheres on steel rods. Red lines indicate the values of the resonant frequencies measured in Fig. 3.16

of the system from the possible sources of the peaks observed at very low frequency in Fig. 3.12, Fig. 3.13 and Fig. 3.17.

Next, we focus on the transfer function of the static force apparatus at higher frequency, above 1 kHz, see the red circle in Fig. 3.16. Here, one observes resonant peaks and anti-resonant deeps at frequency between 2.5 kHz and 4.7 kHz, right in the middle of the pass band of the granular chains: the pass band is comprised between 2-4 kHz with polyacetal spheres while it is 2-6 kHz with steel spheres, see Fig. 3.13). As to verify if these resonances and anti-resonances may perturb the characterization of one-dimensional alignments, we intend to estimate the stiffness k_E at the boundary, as the ratio between the force F and the displacement $\delta_0 = \gamma/\omega^2$ of the apparatus: ideally, the stiffness k_E should be very large compared to the typical stiffness of the alignment. The stiffness k_E is thus compared to the Hertzian stiffness k_H between contacts given by Eq. 2.20,

$$k_H = ER\left(\frac{6F_0}{ER^2}\right)^{1/3}. \tag{3.17}$$

The experimental measurements of k_E is compared to the estimations of k_H in Fig. 3.18. One sees that above few hundreds hertz, the effective stiffness k_E at the extremity, where the static force apparatus stands, is few order of magnitude larger than the stiffness k_H between the spheres. The static force apparatus would thus not deform or displace: it should not affect the characterization of the media in the frequency region of interest. However, k_E falls below k_H at extremely low frequencies, below 200 Hz for steel spheres and below 30 Hz for polyacetal spheres. The latter relies on the inertia of the static force apparatus, which is not sufficiently large at very low frequency to prevent the recoil of the static force apparatus. Below these frequencies, the estimation of the transfer function of the samples should be considered with care, since they may not be

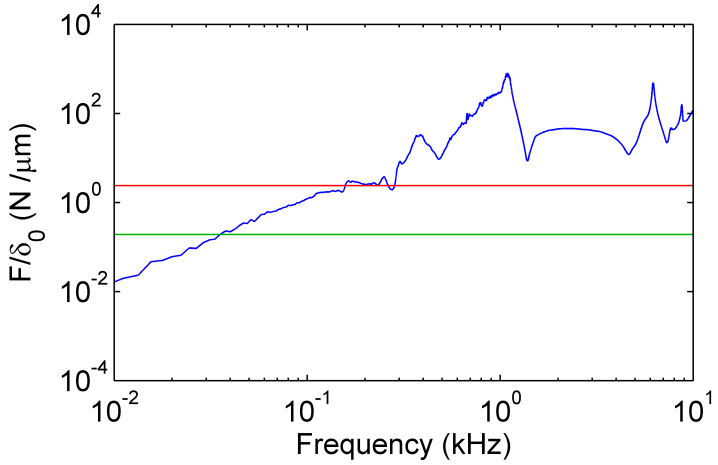

Figure 3.18: Effective stiffness k_E of the end extremity, as the ratio between the force F measured by the impact hammer and the displacement δ_0 measured from the accelerometer. The red line (resp. the green line) indicates the typical stiffness k_H between two steel spheres (resp. between two polyacetal spheres).

fully reliable.

In a very final attempt, we focus our attention on the behavior of the elastic rods supporting the granular chain. These rods are very stiff in traction and compression: the only reasonable deformation may rely on bending. Here, we aim at verifying if the bending of the cylindrical rods may participate to the low frequency region of the transfer function.

We start from the equation of propagation of bending waves in a cylindrical beam. The transverse displacement $z_b(x,t)$ satisfies the equation [110],

$$\rho_s A_s \ddot{z}_b(x,t) + E_s I_s \frac{\partial^4}{\partial x^4} z_b(x,t) = 0, \tag{3.18}$$

where $A_s = \pi R_s^2$ is the cross section of the supporting beam with radius R_s, ρ_s is the density, E_s is the Young's modulus and $I_s = \pi R_s^4/2$ is the second moment of inertia. Looking for the dispersion relation of a harmonic bending wave $z_b(x,t) = e^{i(\omega t - q_b x)}$, where $q_b = \omega/c_b$ is the bending wavenumber and c_b is the bending wave speed, the Eq. 3.18 gives

$$q_b = \left(\frac{\rho_s A_s \omega^2}{E_s I_s}\right)^{1/4} \propto \left(\frac{\omega}{c_L R_s}\right)^{1/2}, \tag{3.19}$$

where c_L stands for the longitudinal wave speed in the rod, $c_L \propto \sqrt{E_s/\rho_s}$. The wave speed $c_b = \omega/q_b$ of the bending mode is thus

$$c_b = \left(\frac{E_s I_s \omega^2}{\rho_s A_s}\right)^{1/4} \propto (\omega c_L R_s)^{1/2}. \tag{3.20}$$

As a consequence, assuming an unconstrained finite length beam of length L, the

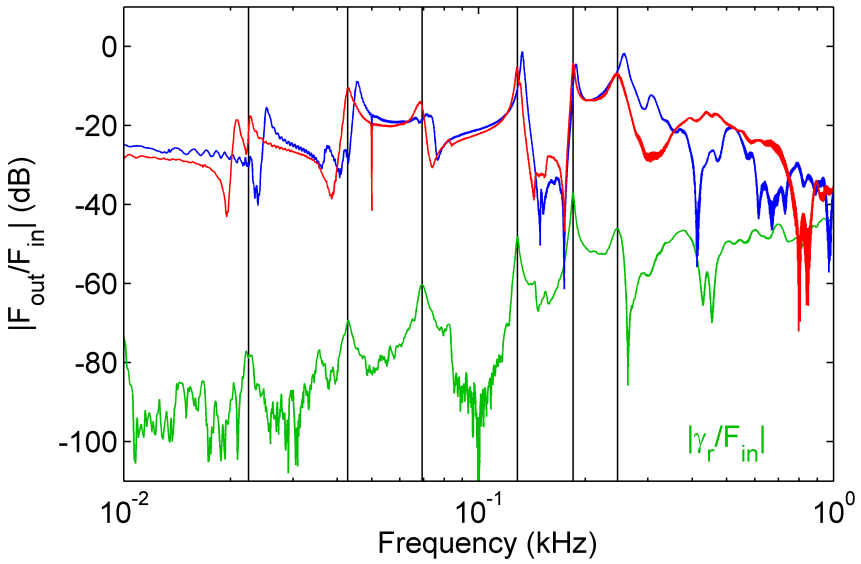

Figure 3.19: Modulus of the transfer function between the input force F_{in} and the output force F_{out} measured for 20 N (blue) and for 40 N (red) static compression. The green curve represents the transfer function between the radial acceleration γ_r of a supporting cylinder and the axial input force F_{in}. The black vertical lines indicate the resonant frequencies found experimentally at about 22.5, 42.8, 69, 128.6, 184.8 and 246.4 Hz.

normal modes matches $q_b L = n\pi$ with n an integer, such that the bending frequencies of resonance are, from Eq. 3.19,

$$\omega_n \propto c_L R_s \left(\frac{n\pi}{L}\right)^2 . \tag{3.21}$$

Experimentally, we verify the presence of bending modes in the supporting rods by sensing the radial acceleration γ_r captured by an accelerometer glued on the lateral side of a cylinder. The acceleration normalized to the dynamic force input shown in Fig. 3.19 indeed reveals a transverse deformation of the rods while exciting the alignment with a chirp signal.

Comparing the experimental transfer function between F_{in} and F_{out} with the experimental transfer function between F_{in} and γ_r, one clearly observes that the transverse deformations of the rods closely rely on the frequency peaks observed at low frequency region. Additionally, the numerical estimation of the five first resonant frequencies, from Eq. 3.21, of a steel rods (radius $R_s = 5$ mm, length $L_s = 1.15$ m, $E_s = 190$ GPa and $\rho_s = 7780$ kgm^{-3}) indicates that $f_n = 14.6, 58.6, 132.1, 234.7$ and 366.8 Hz. Up to certain extent, the minimal model given by Eq. 3.21 provides a fair agreement, as shown in Fig. 3.20.

Since the alignments of spheres slightly buckle when set under static compression - all spheres are aligned up to a given tolerance - the transverse deformation of the supporting rods thus introduce a weak coupling with the axial displacement of the spheres. As a consequence, we can thus conclude from the very last experimental probe that the resonant

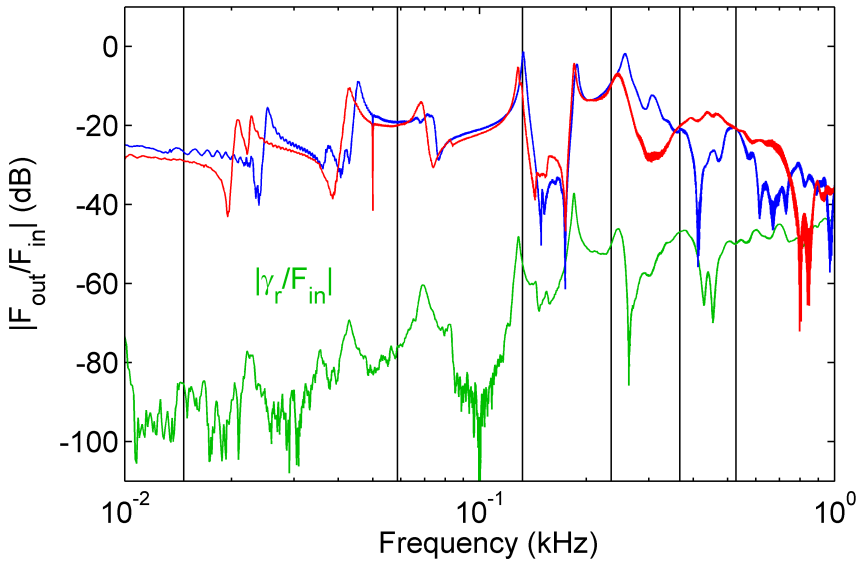

Figure 3.20: Modulus of the transfer function between the input force F_{in} and the output force F_{out} measured for 20 N (blue) and for 40 N (red) static compression. The green curve represents the transfer function between the radial acceleration γ_r of a supporting cylinder and the axial force F_{in}. Here, the black vertical lines show the resonant frequencies estimated theoretically by a simple model at 14.6, 58.6, 132.1, 234.7 and 366.8 Hz, from Eq. 3.21. These frequencies correspond to the mode number n= $1, 2, 3, 4, 5, 6$, respectively.

peaks observed below the cutoff frequency f_0 in the transfer functions of the alignments essentially relies on the bending deformation of the supporting cylinders. These peaks are most favorably detected below the cutoff frequency f_0, where the longitudinal waves are strongly attenuated. Above the low frequency cutoff of the samples, where longitudinal waves propagate through the sample, the bending modes likely exist but contribute to a lesser extent. In addition, the bending modes frequency being inharmonic, see Eq. 3.21, the density of these modes rapidly decreases with the frequency.

3.7 Conclusions

In this chapter we have focused our attention on the careful presentation and calibration of the experimental setup. Firstly, we characterized the bulk elastic properties of our spheres from ultrasonic experiments. Then, we derived a reliable and repeatable method to set our alignments of spheres under static compression; as far as one can do, we aimed at ensuring that the static compression is homogeneously distributed along the alignment. Next, we carefully ruled out any observable artifacts from the experimental setup, in order to ensure the accuracy of further estimations of the transfer function of one-dimensional granular media. Then, we unraveled a low frequency region with a significant attenuation due to frictional and elastic interactions between the grains and

the aligning rods. These interactions likely induce an elastic on-site potential between the particles and their supports, as demonstrated in the next chapter. One of the pitfalls of the coupling between the particles and their supports is related to the fact that it generates transverse deformations of the rods that ultimately lead to the propagation of spurious bending waves along them. However, the strongest effects of the bending modes in the rods are mostly concentrated at low frequency. Having undertaken this study, one can now tackle a detailed experimental analysis on wave propagation in dry granular media, as presented in the next chapter.

Chapter 4

Waves in dry 1D granular media

Contents

4.1 Wave propagation in 1D alignments of spheres

In the previous chapter, we related the occurrence of a low cutoff frequency f_0 observed in Fig. 3.12 and in Fig. 3.13 to the existence of an elastic on-site potential between every particle and their supports. Here and in the following, we will denote the stiffness of this potential as k_0. In the first section of this chapter, we derive a theoretical expression for k_0 as a function of the elastic and geometrical properties of both the spheres and the cylindrical supports. We then find the dispersion relation in an alignment of particles that account for such a local potential at every bead. Then in the next three sections, we describe the experimental procedures as to estimate the phase velocity, the group velocity and the attenuation in these media. Lastly we compare our observations to the analytic estimations.

4.1.1 Zero frequency band gap and cutoff frequencies

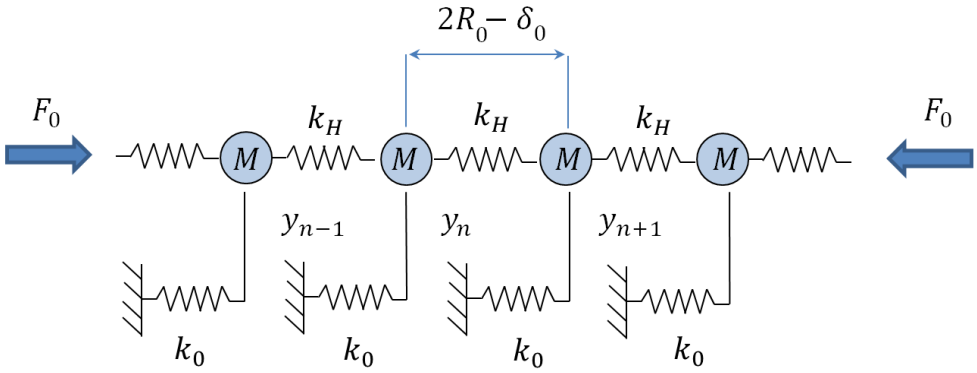

Figure 4.1: One-dimensional chain of spheres with mass M under static compression F_0 interacting via a Hertzian contact stiffness k_H, with an additional stiffness k_0 which quantifies the interaction of the spheres with the support.

Firstly, we focus on the theoretical derivation of k_0 and f_0. For this purpose, we model the granular medium as an alignment of compressed spheres, with mass M, interacting via the Hertz potential k_H given by Eq. 2.20. In addition, every particles interact with the ground via an elastic potential with stiffness k_0. As for the alignment described in Sec. 2.5, see Eq. 2.84, one uses the Newtonian's second law of motion,

$$M\ddot{y}_n = \kappa\left(\delta_0 + y_{n-1} - y_n\right)^{3/2} - \kappa\left(\delta_0 + y_n - y_{n+1}\right)^{3/2} + k_0 y_n, \tag{4.1}$$

where $\kappa = \sqrt{2R_0}E_0/[3(1-\nu_0^2)]$. In the linear regime, see Eq. 2.85, Eq. 4.1 becomes,

$$M\ddot{y}_n \simeq k_H(y_{n+1} + y_{n-1} - 2y_n) + k_0 y_n, \tag{4.2}$$

with $k_H = (3/2)\kappa\delta_0^{1/2}$. By looking for a harmonic plane wave solution $y_n(t) = y(x =$

$2nR_0, t) = e^{j(\omega t - qx)}$ one finds the dispersion relation,

$$\omega^2 = \omega_{cut}^2 \sin^2(qR_0) + \omega_0^2, \tag{4.3}$$

where ω_0 stands for the low cutoff frequency,

$$\omega_0 = \sqrt{\frac{k_0}{M}}, \tag{4.4}$$

and ω_{cut} is

$$\omega_{cut} = 2\sqrt{\frac{k_H}{M}}. \tag{4.5}$$

According to the dispersion relation Eq. 4.3, the wavenumber q is purely imaginary below the low cutoff frequency, $\omega < \omega_{min}$, and above the high cutoff frequency, $\omega > \omega_{max}$, with

$$\omega_{min} = \omega_0, \tag{4.6}$$

$$\omega_{max} = \sqrt{\omega_{cut}^2 + \omega_0^2}. \tag{4.7}$$

In between, for $\omega_{min} < \omega < \omega_{max}$, the wavenumber is real: waves propagate. The alignment schematized in Fig. 4.1 is thus characterized by a band gap at zero frequency, a forbidden band at high frequency and a propagative band in between.

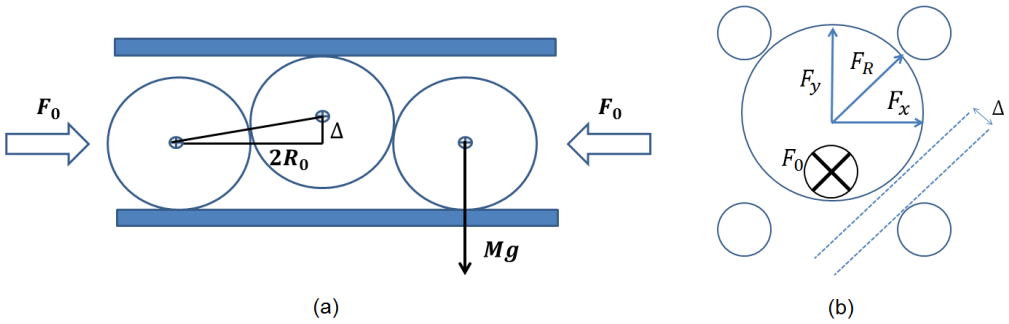

Figure 4.2: (a) Spheres with radius R_0, weight Mg and clearance Δ under compression F_0. (b) Axial view, where F_y is the projection of F_0 and F_r is the radial force.

Theoretically, we model k_0 as twice the tangential component of the stiffness between a sphere and a cylinder, see Eq. 2.29,

$$k_0 = 2 \times 2G_r \left(\frac{3F_R R_r}{4E}\right)^{1/3}, \tag{4.8}$$

where R_r, G_r and E stand for the effective radius, Shear and Young's modulus, see from Eq. 2.29 to Eq. 2.31, and F_R is the magnitude of the radial force that compresses a sphere on one cylinder. The stiffness is counted twice in Eq. 4.8 since every sphere is in contact with two cylinders. The radial component F_R comes from the buckling of the

alignment of spheres. Considering a clearance Δ between the diameter of the spheres and the distance between two cylinders, see Fig. 4.2, the alignment can indeed naturally buckles when it is set under static compression. The origin of the clearance comes from the machining of the spacers, made of plexiglas, that maintain the four cylinders in place, as shown in Fig. 3.1 and in Fig. 3.2. We checked that the clearance is about $\Delta \simeq 0.5$ mm at the most. From a geometrical consideration, see Fig. 4.2, the radial force is either the projection of the static force F_0 exerted in the axial direction of the alignment,

$$F_R \simeq \frac{\Delta F_0}{4R_0} \text{ if } F_R \gg Mg, \tag{4.9}$$

or the projection of the weight Mg of a sphere

$$F_R \simeq \frac{Mg}{\sqrt{2}} \text{ if } F_R \ll Mg, \tag{4.10}$$

where g is the gravity. Here in Eq. 4.9, the radial force is $F_R = \sqrt{F_x^2 + F_y^2} \simeq \sqrt{2}F_y$, see Fig. 4.2, if one assumes $F_x = F_y$ with $F_y \simeq (F_0/2)(\Delta/\sqrt{2})/(2R_0)$.

According to Eq. 4.4 and Eq. 4.8, the lower cutoff frequency f_0 depends on the characteristics of the spheres and the supporting cylinders. If the beads are not too heavy (this is the case for polyacetal spheres, as shown below) in respect to the radial force F_R, then the lower cutoff frequency may depend on the static force F_0 maintained in the axial direction of the alignment, see Eq. 4.9. Otherwise, f_0 does not depend on F_0 if the spheres are heavy enough, as it is the case with steel beads, as shown below.

Next, we confront the theoretical expression given by Eq. 4.4 and Eq. 4.8 with the experimental observations shown in Sec. 3.6, see for instance the Fig. 3.14. As to estimate f_0, we indeed used different combinations involving polyacetal or steel spheres and plexiglas or steel rods. For the estimations of f_0, we consider a Young's modulus $E_c = 3.3$ GPa, a Poisson ratio $\nu_c = 0.3$ and a radius $R_c = 5$ mm for the plexiglas cylinders, while the Young's modulus of steel cylinders if assumed at $E_c = 190$ GPa.

The mass of one steel bead is $M \simeq 63.8$ g and the mass of one polyacetal bead is $M \simeq 10.9$ g. In the case of steel beads with steel supports one has $0.1 \times Mg < \Delta F_0/4R_0 < 0.6 \times Mg$: we thus retain the approximation given in Eq. 4.10 to estimate the radial force F_R. In this case, the lower cutoff frequency does not depend on the static load F_0, $f_0 = \text{const}$ in first approximation. For polyacetal spheres, one finds $0.5 \times Mg < \Delta F_0/4R_0 < 3.8 \times Mg$: the weight of a polyacetal sphere is marginal in the range of moderate to large axial static forces and we thus retain the approximation given in Eq. 4.9 to estimate the radial force F_R. For polyacetal, the lower cutoff frequency depends on the axial static force, $f_0 \propto F_0^{1/6}$ in first approximation.

All these results are consistent with the observations given in Sec. 3.6. A close comparison between these data and the theoretical estimation of f_0, given by Eq. 4.4 and Eq. 4.8, is shown in Fig. 4.3. Our model explains quantitatively and qualitatively the experimental findings: one observes a nonlinear increase of the lower cutoff frequency

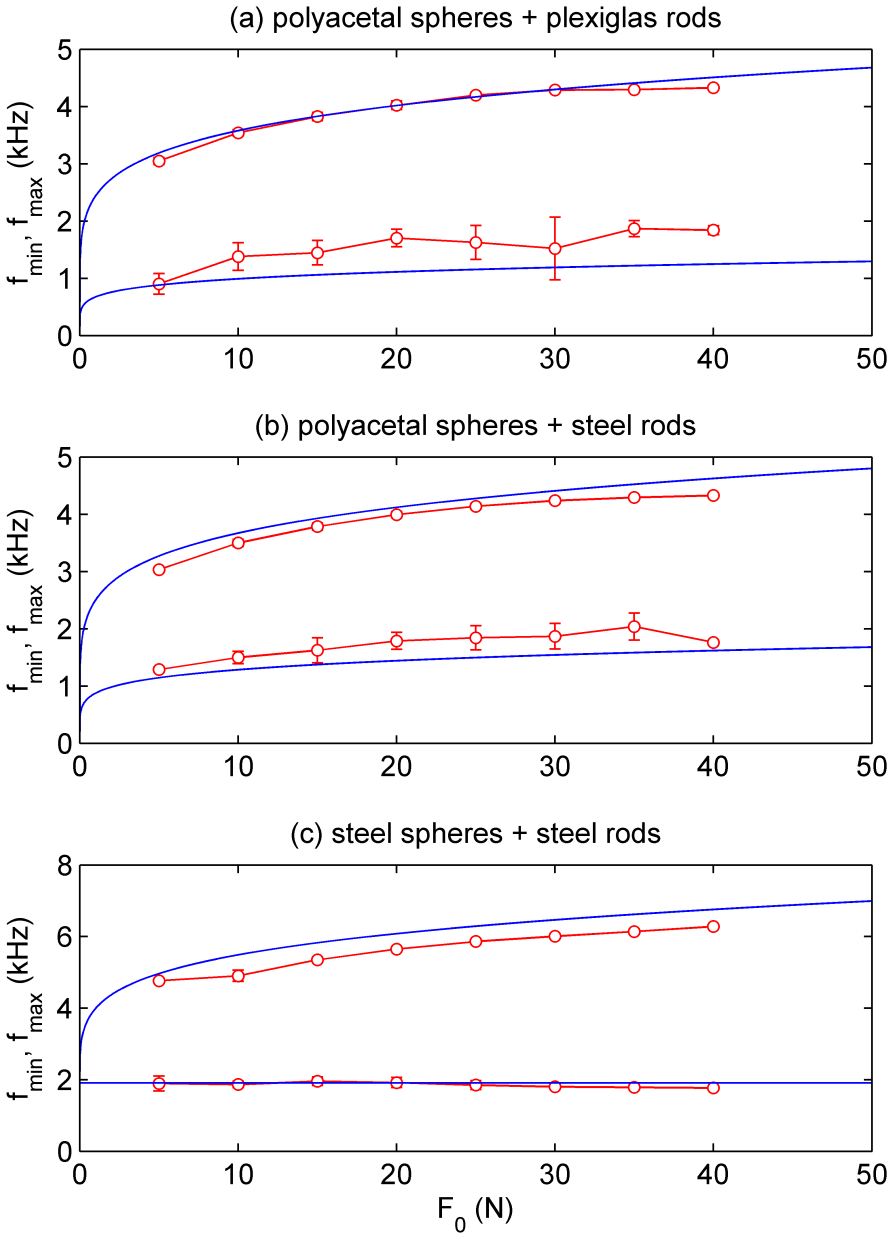

Figure 4.3: Lower and upper cutoff frequencies, f_{min} and f_{max}, as a function of the static force in the axial direction. (a) Configuration with polyacetal spheres and plexiglas supports, (b) polyacetal spheres with steel supports and (c) steel spheres with steel supports. Blue lines represent Eq. 4.6 and Eq. 4.7 and red dots are the experimental data extracted from Fig. 3.13 and shown in Fig. 3.14.

$f_{min} = f_0$ with the axial static force, see Fig. 4.3(a) and (b). In turn, when considering steel spheres, the lower cutoff frequency is almost constant over the range of compression, see Fig. 4.3(c). In all cases, the upper cutoff frequency f_{max} increases with the axial static force F_0, in fair agreement with Eq. 4.7.

In this section, we derived an expression for the lower and the upper cutoff frequency, f_{min} and f_{max}, which reliably describe the experimental data. We thus showed that the elastic coupling between the spheres and the cylindrical supports, via shear deformations due to sticky frictional contacts between the two, introduces a zero frequency band gap in the dispersion relation of an alignment of particles. The precise knowledge of the dispersion relation, see Eq. 4.3, now allows one to determine all the features of the waves that propagate in these media. In the next sections we aim at probing how fast they propagate and attenuate.

4.1.2 Theoretical dispersion relation with on-site potential

In this section, we focus on the theoretical estimation of the dispersion relation, in order to get information on the wave speed and the loss factor. The dispersion relation is, from Eq. 4.3,

$$q = \Re(q) + i\Im(q) = \frac{1}{R_0}\text{asin}\left(\frac{\sqrt{\omega^2 - \omega_0^2}}{\omega_{cut}}\right), \tag{4.11}$$

From Eq. 4.11, one can estimate the phase velocity c_ϕ, the group velocity c_g and the attenuation length l_a,

$$c_\phi = \frac{\omega}{\Re(q)}, \tag{4.12}$$

$$c_g = \frac{\partial\omega}{\partial\Re(q)}, \tag{4.13}$$

$$l_a = \frac{-1}{\Im(q)}. \tag{4.14}$$

As an example, we represent in Fig. 4.4 the dispersion relation given by Eq. 4.11 both in magnitude and in phase, for an alignment of polyacetal spheres supported by cylindrical rods made of materials with very different elasticity. Here, the dissipation is taken into accounts via the loss angle measured in polyacetal in Sec. 3.2.1. In Fig. 4.4(b), we show the magnitude of the transfer function $H = \exp(-i\Im(q)L)$ in dB. One can observe clear forbidden bands, at zero frequency and above a high cutoff frequency. In the propagative band, the waves are dispersive: the phase velocity and the group velocity differ and both depends on the frequency.

As to quantify and measure the dispersion relation given by Eq. 4.11 in the following, we rewrite the wave number in a more convenient way,

$$q = \left(\frac{\omega}{c_\phi} - \frac{i}{l_a}\right) = (\omega/c_\phi) \times (1 - i\eta), \tag{4.15}$$

where η is the loss factor: the loss factor is defined as the ratio of the energy dissipated per cycle of oscillation to the energy stored during one cycle,

$$\eta = \frac{1}{\omega\tau_a} = \frac{c_\phi}{\omega l_a} = \frac{1}{\Re(q) l_a} = \frac{\lambda}{2\pi l_a}, \tag{4.16}$$

where $\tau_a = l_a/c_\phi$ is a relaxation time related to the dissipation.

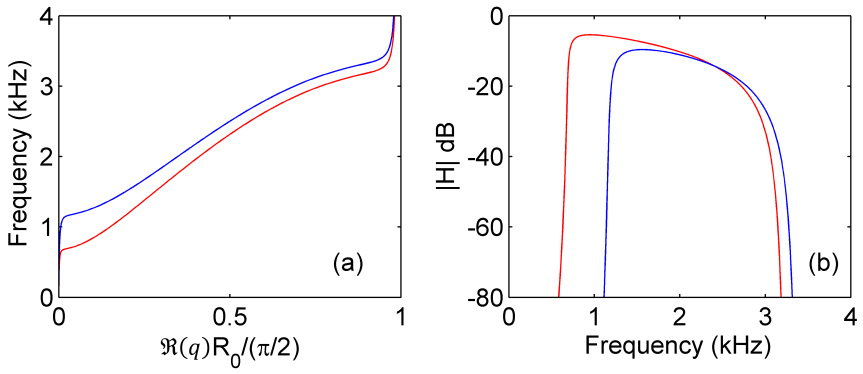

Figure 4.4: (a) Theoretical dispersion relation, where $\Re(q)$ is the real part of the wave number and R_0 is the sphere radius, (b) modulus of the transfer function. Here the results are estimated for polyacetal spheres under a 20 N static compression. The spheres are supported by four 1 m long rods with Young's Modulus of $E_s \simeq 0.1$ GPa (red curves) and with $E_s \simeq 200$ GPa (blue curves).

4.1.3 Long wavelength speed and attenuation estimations

Here, for sake of clarity and simplification, we consider the long wavelength approximation of Eq. 4.11. On purpose, we consider an arbitrary medium where the stiffness of the on-site potential is weak compared to the contact stiffness between spheres, i.e. $\omega_{max} \gg \omega_{min}$ see Eq. 4.6 and Eq. 4.7. We analyze this medium in an intermediate frequency range $\omega \simeq (\omega_{max} + \omega_{min})/2$, such that the angular frequency is high enough to neglect the effect of the on-site potential and is low enough to linearize the Eq. 4.11,

$$q \simeq \frac{\omega}{R_0\omega_{cut}}, \tag{4.17}$$

where ω_{cut} is given by Eq. 4.5. In the intermediate frequency range, see Fig. 4.4, the wave number is such that $\Re(q)R_0 \simeq \pi/4 \sim 1$: the wavelength $\lambda = c_\phi/f = 2\pi/\Re(q)$ is few particles wide, $\lambda/2R_0 \sim 4$.

We then account for the attenuation of waves from the dissipation involved by the deformation of the contacts between the particles. This dissipation is rendered by the complex elastic modulus $E = E_0 e^{i\delta}$ introduced in Sec. 3.2.1, where δ is the loss angle, see Eq. 3.8: we measure $\delta \simeq 0.053$ in polyacetal and $\delta \simeq 0.023$ in steel. Since $\omega_{cut} \propto$

$k_H^{1/2} \propto E^{1/2}$, see Eq. 2.20 and Eq. 4.5, then one finds,

$$c_\phi \simeq c_g \propto c_0 (P/E_0)^{1/6}, \tag{4.18}$$

$$\eta \simeq \tan(\delta/2), \tag{4.19}$$

where $c_0 = (E_0/\rho)^{1/2}$ is proportional to the speed of longitudinal waves in the bulk material of the spheres and $P = F_0/\pi R_0^2$ is the confinement pressure.

In Eq. 4.19, η stands for a rough estimation of the attenuation in the dry case. In turn, the friction of the beads on the supports may also affects the attenuation of the waves. In this case, the loss factor may account for such a contribution,

$$\eta \simeq \tan(\delta/2) + \eta_f, \tag{4.20}$$

where $\eta_f = 1/\Re(q) l_f$ and where l_f is the frictional attenuation length defined in Eq. 3.16. According to the order of magnitude indicated in Eq. 3.16, $l_f/2R_0 \sim 10$, the frictional loss factor would lies around $\eta_f \sim 0.05$ in the intermediate range $\Re(q)R_0 \sim 1$. It thus turns out that the contribution of the friction to the attenuation of the waves, when friction is involved between the particles and their supports, has likely the same strength as the dissipation in the contact between particles, $\tan(\delta/2) \sim 0.025$, with polyacetal spheres and steel supports,

$$\eta_f \sim \tan(\delta/2). \tag{4.21}$$

4.1.4 Measurement method of the wave speed and the loss factor

In this subsection, we provide the details of the protocol derived to obtain reliable measurement of both the wave speed and the attenuation in alignments of particles. Owing to the experimental protocol described in Sec. 3.5 and in Sec. 3.6, we quantified the transfer function between the input dynamic force measured at one extremity of the alignment, $F_{in} = F(x = 0, t)$, and the output $F_{out} = F(x = L, t)$ at the other end, where L is the total length of the chain. Considering a harmonic plane wave $F(x, t) = e^{i(\omega t - qx)}$, such that the Fourier transform over time is $\mathrm{FT}_t[F(x, t)]$, the transfer function is

$$H(L, \omega) = \frac{\mathrm{FT}_t[F(x = L, t)]}{\mathrm{FT}_t[F(x = 0, t)]} = e^{-iqL}. \tag{4.22}$$

where q is the complex wave number. Note that in practice, the sample is excited by a broad frequency range chirp signal and we measure the average transfer function over a large number of acquisitions from the method detailed in Eq. 3.9, from which one also estimates the coherence from Eq. 3.10.

According to Eq. 4.22, the phase and the magnitude of the transfer function provides estimations of the phase velocity c_ϕ and the attenuation length l_a, see Eq. 4.15,

$$\phi(\omega) = -\Re(q)L = -\omega L/c_\phi(\omega). \tag{4.23}$$

$$|H(L,\omega)| \quad = \quad \exp\left[-\Im(q)L\right] = \exp\left[-L/l_a(\omega)\right]. \tag{4.24}$$

However, issues with this this approach is twofold. Owing to the strong attenuation near the cutoff frequency and inside the low and the high forbidden bands, see Fig. 3.13 for instance, the signal to noise ratio of the transmitted wave is thus degraded. This leads to the determination of the transfer function with a very poor coherence between the input and the output of our samples near edges of pass band. This *first limit* is illustrated in Fig. 4.5, where we show both the normalized phase and the coherence of H as a function of frequency. The phase and consequently, the phase velocity is poorly determined in frequency bands where the attenuation is strong, i.e. where the coherence between input and output signals is weak. The *second limit* is related to the fact that the phase of the transfer function turns very quickly as a function of frequency. Indeed, assuming a phase velocity at about $c_\phi \sim 250$ m/s (see below), the phase is about $\phi/2\pi \sim 20$ at the upper frequency 5 kHz and for $L = 1$ m. Issues arise when attempting to unwrap the phase, not mentioning the fact that the low frequency reference phase is not reliable to modulo 2π. The *third limit* relies on the existence of additional modes, see for the bending waves that may propagates in our supports described in Sec. 3.6.2. These spurious contributions may affect the reliability of our characterization: identifying all the contributions is in fact not an easy task. This third limit is tackled in the following Sec. 4.2.

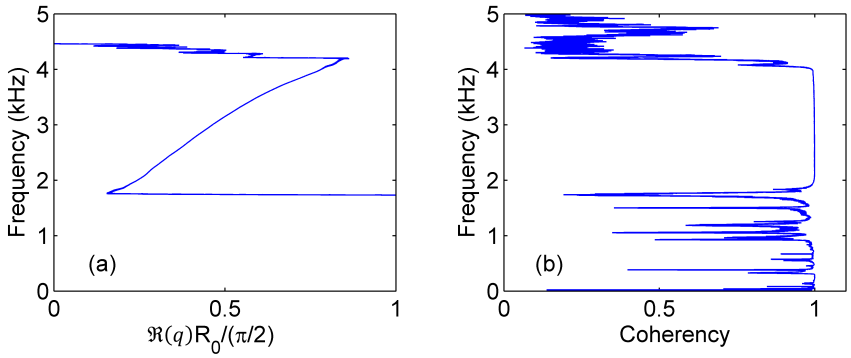

Figure 4.5: (a) Measured dispersion relation for polyacetal spheres with steel support and $F_0 = 20$ N, in response to chirp excitation. $\Re(q)$ is the real part of the wave number and R_0 is the radius of the spheres. (b) Coherency between the output and input signals.

Here, we present a protocol to tackle the issues found from the ambiguity of the phase shifting. Instead of the phase velocity, we aim at estimating the group velocity from the group delay. The method consists in the deconvolution of the transfer function acquired with a chirp excitation, Eq. 4.22, by a well defined analytic incident wavepacket $F_{pulse}(x = 0, t)$, defined as a gaussian pulse centered on any specific frequency f_c and with a narrow frequency bandwidth.

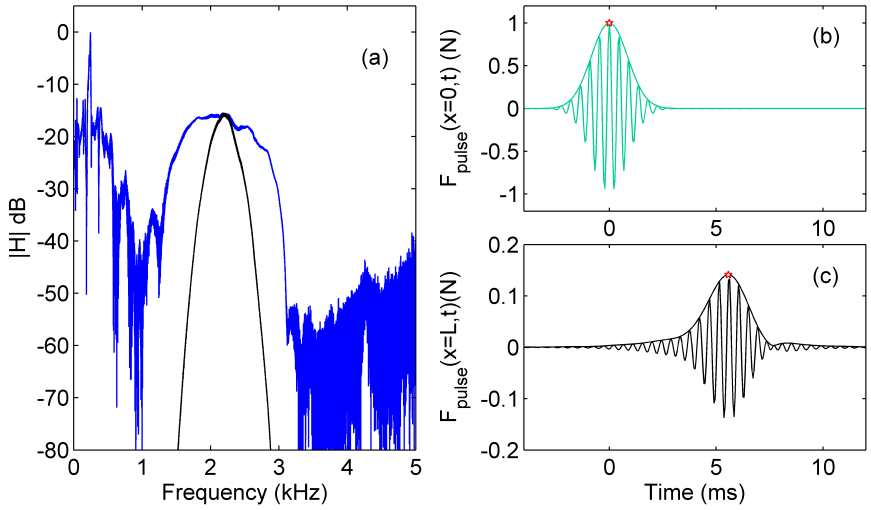

Figure 4.6: Example of the experimental method. (a) Magnitude $|H|$ of the experimental transfer function $H(\omega) = F_{out}/F_{in}$ versus frequency, is shown in blue; the black curve represents the Fourier transform of the analytic input wavepacket (b) convolved by the experimental transfer function. Temporal representation of (b) the analytic input wavepacket and (c) output force convolved by the experimental transfer function. All data are shown for an $F_0 = 5$ N static force. Here, the analytic wavepacket is a gaussian pulse centered at $f_c = 2.2$ kHz with bandwidth 0.2. The red stars indicate the maximum of the envelopes.

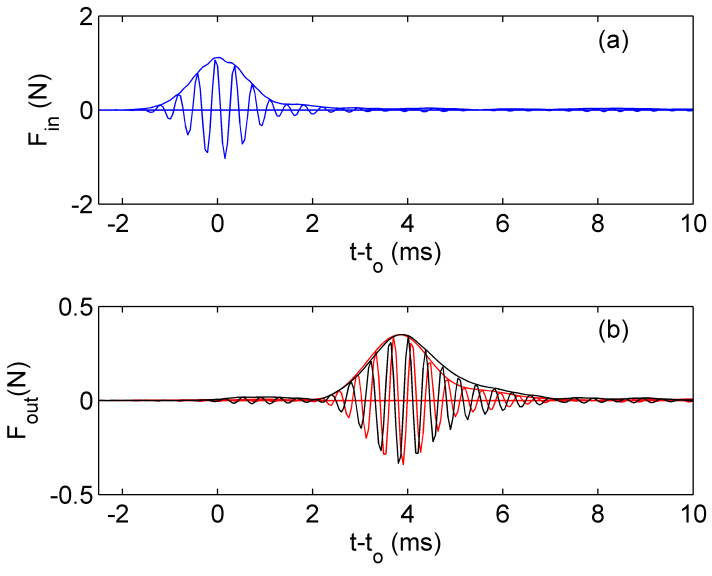

Figure 4.7: (a) Input signal measured at the beginning of the chain $F_{in}(t) = F_{pulse}(x = 0, t)$. (b) Output signal measured as the response of gaussian pulse excitation $F^g_{out}(t)$ (black curve) and as the convolution of the input (a) with the experimental transfer function measured from the response of broadband chirp excitation $F_{out}(t) = F_{pulse}(x = L, t)$ (red curve, see the details of the method in Sec. 4.1.4).

The transmitted wavepacket is thus

$$F_{pulse}(x=L,t) = \mathrm{FT}_t^{-1}\{H(L,\omega) \times \mathrm{FT}_t[F_{pulse}(x=0,t)]\}, \tag{4.25}$$

and one can extract its envelope as the absolute value of the Hilbert transform,

$$F_{pulse}^{env}(x=L,t) = |\mathrm{FT}_t^{-1}[F_{pulse}(x=L,t)]|. \tag{4.26}$$

The estimation of the magnitude and the arrival time of the maximum of the envelope then provides information on the dissipation and the group delay τ_g (the time of flight of the maximum of a wavepacket), i.e. on the attenuation length and on the group velocity $c_g = L/\tau_g$. The protocol defined in Eq. 4.25-4.26 is illustrated in Fig. 4.6. As a crude check of reliability of the method, we compare in Fig. 4.7 a transmitted gaussian F_{out}^g pulse measured in an alignment of spheres to the deconvolution of the acquired incident pulse $F_{pulse}(x=L,t)$ with the transfer function obtained from a chirp excitation. The transmitted and the deconvolved pulses fairly match one to the other: the method defined in Eqs. 4.23-4.24 and the method described in Eqs. 4.25-4.26 thus provide similar features and shapes. Any nonlinearity may have introduced some bias, which are not observable here. Finally, from the practical point of view, it is worth mentioning that acquiring a transfer function with a chirp excitation, at once, and then deconvolving as many gaussian pulses at any frequency, instead of exciting the sample with many pulses, significantly saves time when performing experiments.

4.1.5 Experimental values of the wave speed and the loss factor

Having validated the experimental method, we now present the experimental estimations of the group velocity c_g and the loss factor $\eta = c_\phi/\omega l_a$, obtained from the protocol defined in Eqs. 4.25-4.26. Since the phase velocity is poorly determined, we assume that $c_\phi \simeq c_g$ in first approximation in the middle of the pass band, such that the loss factor is determined as $\eta \simeq c_g/l_a\omega$. The attenuation length l_a is estimated from the maximum of input envelope, $F_{pulse}^{envm}(x=0,t)$, and output envelope of wave packet, $F_{pulse}^{envm}(x=L,t)$, $l_a = -L/ln(F_{pulse}^{envm}(x=L,t)/F_{pulse}^{envm}(x=0,t))$ (where ln is the natural logarithm).

Here, the granular sample is an alignment of 40 polyacetal spheres supported by four cylindrical rods in steel. We deconvolve the transfer function acquired from a chirp excitation, see Eq. 4.22, to obtain a gaussian pulse centered in the middle of the pass band, at $f_c = (f_{min}(F_0) + f_{max}(F_0))/2$ (where $f_{min}(F_0), f_{max}(F_0)$ are the theoretical values see Sec. 4.1.1) and with a 20% bandwidth, according to Eq. 4.25. Owing to the narrow bandwidth of the analytic pulse, the time of flight of the maximum of the envelope, see Eq. 4.26, thus provides an estimate of the group velocity c_g near the central frequency f_c. The experimental result is presented in Fig. 4.8 as a function of the static force F_0. Here one observes that c_g nonlinearly increases with F_0. These results are compared to the theoretical values given by Eq. 4.11 and Eq. 4.13. In the model, ω_0 and ω_{cut} are inferred from the experimental determination of the low and the high frequency cutoff,

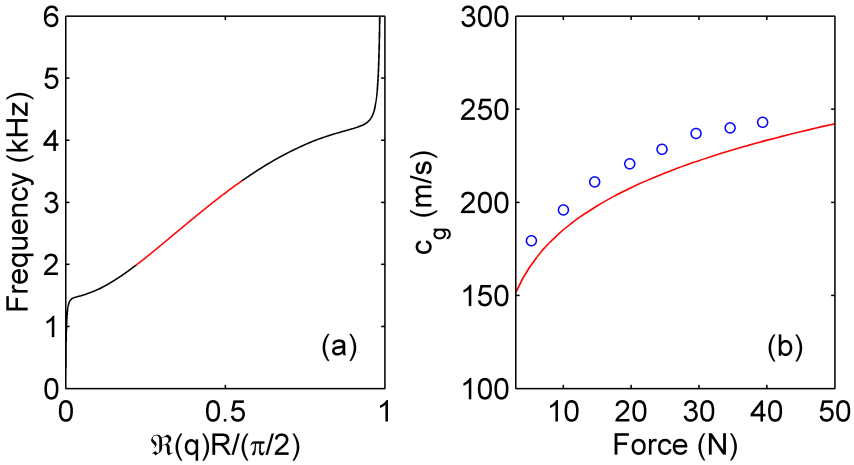

Figure 4.8: (a) Theoretical dispersion relation for polyacetal spheres with steel support under $F_0 = 20$ N static force. From (a), one estimate the theoretical group velocity as the average slope over the frequency range indicated in red. (b) Experimental (blue dots) group velocity, c_g, at central frequency $f_c = (f_{max}(F_0) + f_{min}(F_0))/2$.

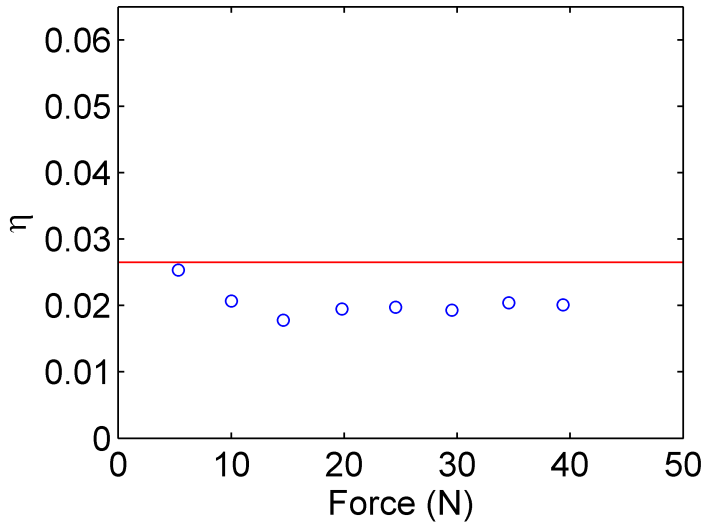

Figure 4.9: Experimental loss factor η (blue dots) versus estimation from Eq. 4.19 (red line) as a function of the static force.

f_{min} and f_{max}, according to Eq. 4.6 and Eq. 4.7; the values of the cutoff frequencies are shown in Fig. 4.3.

In turn, the loss factor is directly estimated from the amplitude ratio between the maximum of the input and output of wave packet's envelopes, and from the approximate knowledge of the phase velocity, $c_\phi \simeq c_g$, see Eq. 4.16. The result are presented in Fig. 4.9. Here, we compare the observations to the theoretical dissipation coming from the viscoelastic behavior of the particles only, see Eq. 4.19. One observes that the prediction provides the correct order of magnitude. The slight overestimation of the prediction is in fact due to the underestimation of the phase velocity by the group velocity, while estimating the loss factor $\eta = c_\phi/\omega l_a \simeq c_g/\omega l_a$, as demonstrated in Sec. 4.2.2.

4.2 Full dispersion relation with an on-site potential

In the Sec. 4.1, we demonstrated that the model given in Eq. 4.11 fairly describes the existence of a pass band between a low and a high cutoff frequency, see Eq. 4.6 and Eq. 4.7. The low frequency cutoff is related to an on-site potential; below this frequency stands a band gap at zero frequency. As mentioned in Sec. 3.6.2, this elastic potential also possibly introduces a coupling with bending waves in the support. These spurious contributions may constitute a limit of the interpretation if they are not correctly identified, see the comments in Sec. 4.1.4. Still, despite the satisfactory agreement found between the measured and the estimated group velocity and loss factor deep inside the pass band, as shown in Sec. 4.1.5, the details of the dispersion relation near the cutoff frequencies remains unclear. Here, we aim at providing a deeper inspection of the dispersion relation, by probing waves as they propagate inside our alignments or particles.

4.2.1 Experimental method and protocol

Here, we use the embedded sensor presented in Sec. 3.3 in order to get a deeper inspection of the features of waves as they propagate inside an alignment of n particles. Here, the embedded sensor probes the dynamic force near a contact, see the picture in Fig. 3.7, as a function of time t and at any position $x = 2nR_0$ in the chain,

$$F_{emb}(0 < x \leq L - 2R_0, t), \tag{4.27}$$

where in our protocol, the sample is driven in $x = 0$ by a 10 s chirp excitation whose frequency ranges from 10 Hz to 7.5 kHz; all acquisitions are repeated 8 times in order to get rid of the noise as much as possible.

From the whole measurement, one can first estimate the Fourier transform over time, similarly to Eq. 4.22,

$$H(x, \omega) = \mathrm{FT}_t[F_{emb}(x, t)]. \tag{4.28}$$

A plot of the magnitude of $H(x, \omega)$ may for instance provide a closer view on how the energy decays in space, as a function of frequency. From now, one can also extract

the Fourier transform over the propagated distance,

$$K(\Re(q), \omega) = \mathrm{FT}_x[H(x, \omega)], \tag{4.29}$$

in order to get a direct access to the dispersion relation, $\Re(q) = 2\pi/\lambda$, including all the modes involved from one extremity of the sample to the other. It is worth mentioning that the function $K(\Re(q), \omega)$ obtained from Eq. 4.28 and Eq. 4.29 can be estimated indifferently as

$$K(\Re(q), \omega) = \mathrm{FT}_{xt}[F_{emb}(x, t)], \tag{4.30}$$

where FT_{xt} is the bi-dimensional Fourier transform over time and space coordinates.

As a crude check of the method, before any measurement, we set the analytic transfer function $H_{th} = e^{-iq_{th}x}$ of a finite chain of $N = 40$ particles in Eq. 4.30, where q_{th} is given by Eq.4.11 and accounts for 20 N static load. It is worth mentioning that H_{th} does not account for wave reflection at the extremities of the sample; these reflections should likely excite resonance modes in the axial direction of the alignment.

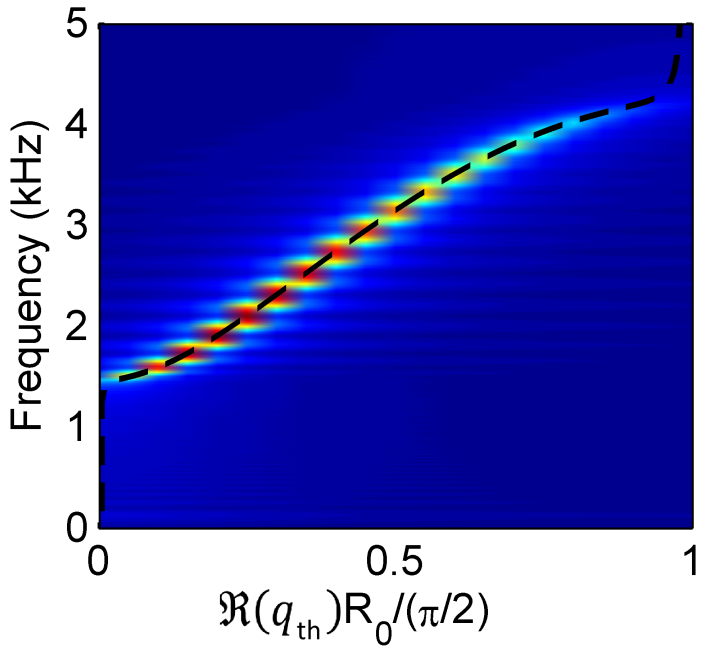

Figure 4.10: Dispersion relation K_{th}, the dashed line is Eq. 4.11. Here the simulations and the analytic estimation are performed for polyacetal spheres with steel rods under $F_0 = 20$ N static compression.

The result of our verification is presented in Fig. 4.10, where we plot the magnitude of K_{th} as a function of the normalized wave number and the frequency. One can observe clearly the dispersion relation between low and high frequency cutoff, which matches the direct estimation given by Eq. 4.11 and superimposed in dashed line.

4.2.2 Experimental results

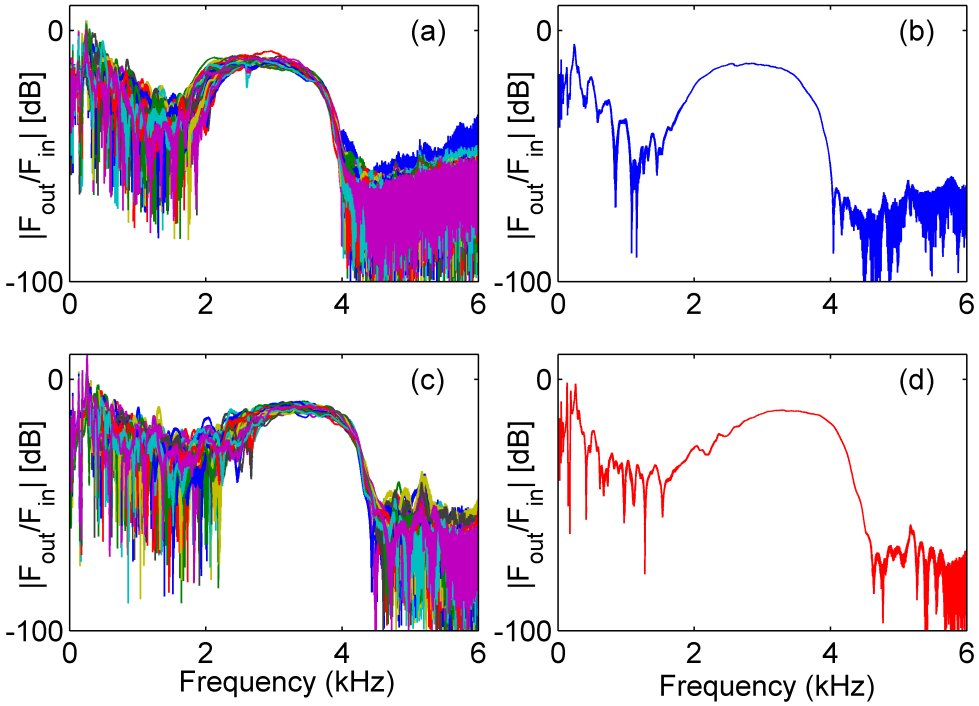

Figure 4.11: (a,c) 40 realizations of the transfer function $H(\omega) = F_{out}/F_{in}$ between the signals measured at the beginning F_{in} and at the end F_{out} of the alignment, as a function of frequency; (a) is at 20 N static compression and (c) at 40 N. (b,d) Average magnitude $|H|$ over the 40 realizations at 20 N and 40 N, respectively.

Experimentally we probe a one-dimensional chain of 40 polyacetal spheres supported by steel rods and either 20 N or 40 N static load. The sample is driven by a 10 s long chirp ranging from 10 Hz to 7500 Hz. Here, one acquires simultaneously the signals at the beginning of the chain where stands the piezoelectric actuator and a dynamic force sensor, $F_{in}(t) = F(x = 0, t)$, at its end $F_{out}(t) = F(x = L, t)$ and at one particular location with the dynamic embedded force sensor $F_{emb}(x, t)$. We then displace the embedded sensor at every positions in the alignment and redo the acquisition. The information gathered by the embedded sensor serves for the estimation of the transfer function $H(x, \omega)$ and the function $K(\Re(q), \omega)$, see Eq. 4.28 and Eq. 4.29. In turn, the forces acquired at $x = 0$ and $x = L$ serve for the estimation of the transfer function defined in Eq. 4.22.

Firstly in Fig. 4.11, we present the modulus of the transfer function H measured between the input and the output extremities. Thanks to the very large amount of data collected by displacing the embedded sensor at every position in the chain, we obtained the well defined average values shown in Fig. 4.11(b,d) at either 20 N or 40 N. Here, one clearly observes, for both static load, a pass band surrounded by the forbidden bands with an attenuation greater than 60 dB; in addition, the bending modes resonances clearly show up in the low frequency forbidden band. Remarkably, the comparison between 20 N

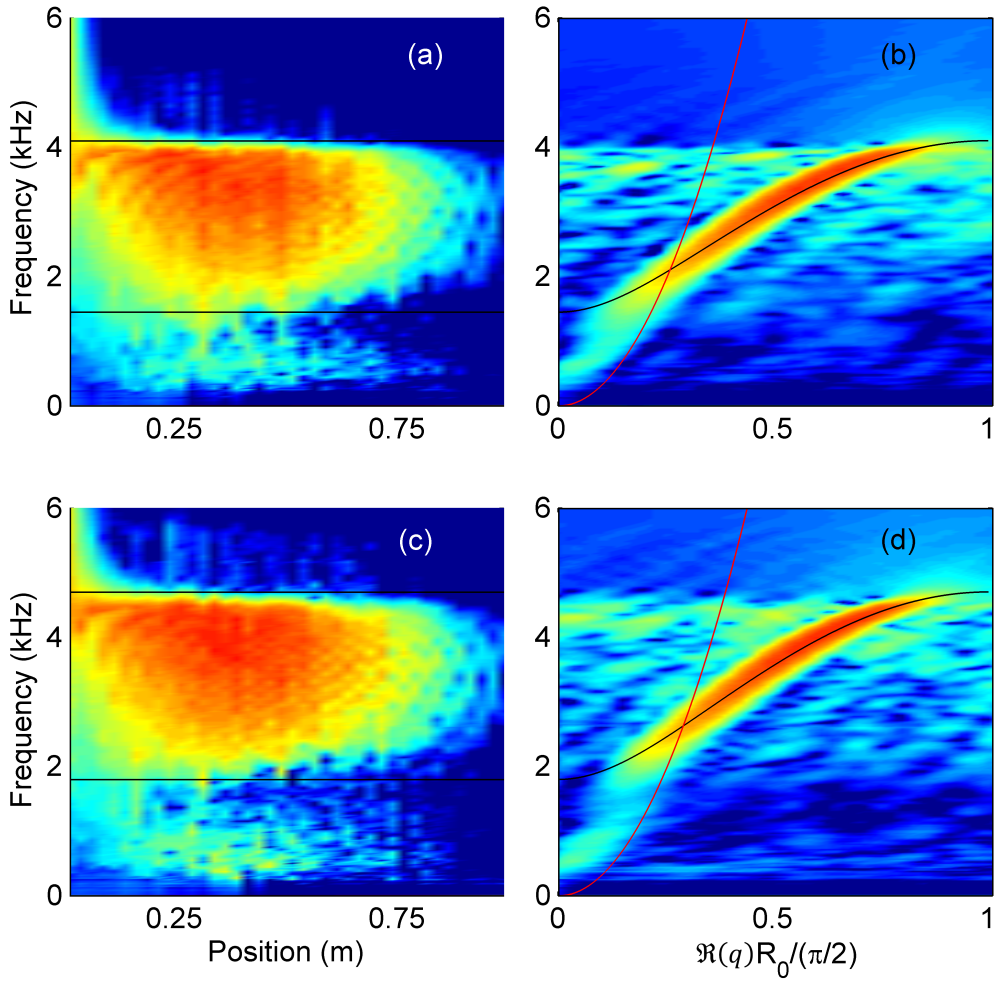

Figure 4.12: (a,c) Modulus of the transfer function measured by the embedded sensor for 20 N and 40 N respectively. (b,d) Dispersion relation reconstructed from the embedded sensor for 20 N and 40 N, respectively. The black vertical lines in (a) and (c) shows the minimal f_{min} and maximal frequency f_{max}, which stems from the fit of the dispersion relation, see the black lines in (b) and (d). Red lines in (b) and (d) stands for the dispersion relation of bending waves. Here, $\Re(q)$ is the real part of the wavenumber and R_0 is the radius of the spheres.

and 40 N experiments shows that the whole pass band is shifted according to the static load, whereas the low frequency resonances do not.

In Fig 4.12(a,c) we plot the modulus of the transfer function $H(0 < x < L, \omega)$ measured at every position of the chain, see Eq. 4.28. One can first,Fig 4.12(a,c), observes the formation of the forbidden bands as the waves propagate deeper inside the alignment. Except at very low frequency, below 1 kHz, both plots shift in frequency according to the confinement pressure. In Fig 4.12(b,d) we show the dispersion relation obtained from the method described in Eq. 4.29. In this figure, we fit the dispersion relation where the low and the high frequency, f_{min} and f_{max}, correspond to the data shown in Fig 4.12(a,c) (black vertical lines). We find that the pass band extend from 1450 Hz to 4100 Hz under 20 N. The theoretical estimation given by Eq. 2.20 and Eq. 4.4 to Eq. 4.9 indicates a frequency range spanning from 1440 Hz to 4120 Hz. For a chain under 40 N we find 1800 Hz and 4700 Hz, and the theory gives 1620 Hz and 4620 Hz. One observes that the model and the measurements are in excellent agreement. In addition, we also superimpose the theoretical dispersion relation of the bending waves traveling in the cylindrical rods, from the knowledge of the bending wave velocity defined in Eq. 3.20. The latter provides a reliable demonstration that the short propagative band below 1 kHz, i.e. inside the zero frequency band gap, comes from the coupling between the chain of spheres and their support.

Finally, we depict in Fig. 4.13 the evolution of the analytic gaussian pulse, deconvolved from the experimental transfer function $H(x, \omega)$ with a method similar to the Eq. 4.25 and Eq. 4.26, as it propagates inside the alignment,

$$F_{pulse}(x,t) = \mathrm{FT}_t^{-1}\{H(x,\omega) \times \mathrm{FT}_t[F_{pulse}(x=0,t)]\}, \tag{4.31}$$

$$F_{pulse}^{env}(x,t) = |\mathrm{FT}_t^{-1}[F_{pulse}(x,t)]|. \tag{4.32}$$

Here, the central frequency of the incident pulse $F_{pulse}(0,t)$ matches the central frequency of the pass band, $(f_{min} + f_{max})/2 \simeq 3.25$ kHz. The Fig. 4.13(a) actually shows the dynamic force oscillations as a function of position and time: this type of plot provides a direct and non-biased observation of the phase velocity, from the slope of the red and the blue parallel beams that unravel the compression and the depletion phases of the wave, respectively. Instead, the plot of the envelop of the deconvolved pulse, see Eq. 4.26, provides a direct visualization of the group velocity as the speed of the maximum of the wavepacket, as shown in Fig. 4.13(b). A quick estimation indicates that the phase velocity is here about $c_\phi \simeq 330$ m/s while the group velocity is about $c_g \simeq 250$ m/s. According to our expectations, the phase velocity is larger than the group velocity inside the propagative band, see for instance the Fig. 4.4 where the ratio $\omega/\Re(q)$ is larger than the slope $\partial\omega/\partial\Re(q)$. In addition, the latter provides an indication on the accuracy of the approximation retained in Sec. 4.1.5 to estimate the loss factor $\eta = c_\phi/\omega l_a \simeq c_g/\omega l_a$; within this approximation, the experimental value of η is likely underestimated by 30%. Taking into account for the phase velocity instead of the group velocity would have led to a better agreement for the attenuation.

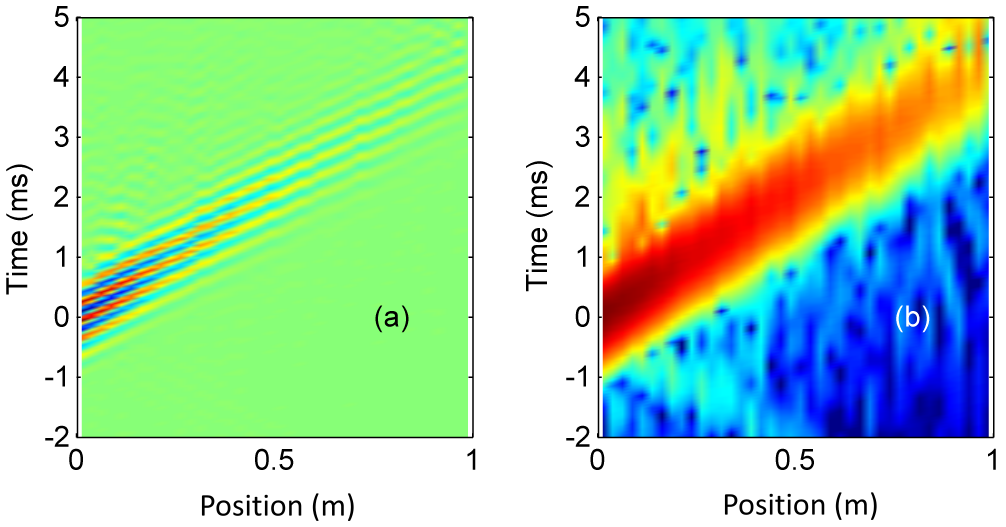

Figure 4.13: (a) Output signal $F_{pulse}(x,t)$ deconvolved from the transfer function measured at each position inside the alignment and as a function of time. (b) Envelope of the pulse $F^{env}_{pulse}(x,t)$ as a function of time and position. Both results obtained by the method given by Eq. 4.31 and Eq. 4.32 while considering an input wavepacket centered at 3.25 kHz and bandwidth 0.3, at $F_0 = 40$ N static force.

4.3 Conclusions

In this chapter, through theoretical and experimental studies, we quantified wave propagation in one-dimensional chains of spherical particles. In particular, we showed that interactions of every sphere with its support induces a low cutoff frequency. We described the coupling between elastic bodies by mean of a tangential component of the stiffness between plane and cylinder, which provides a quantitative prediction of the cutoff frequencies of various combinations of spheres and supports, as a function of either the weight of the spheres or the static load applied on the sample. Next, we quantified a global group velocity and the loss factor in the pass band; our description of the system matches the experimental observations. Finally we unraveled the full dispersion relation of the system thanks to an embedded force sensor that allows measuring perturbations as they propagates inside the chain; the experimental dispersion relation is in close agreement with the prediction and our measurements allows identifying the spurious propagation of bending waves in the supports at very low frequency.

Chapter 5

Waves in wet 1D granular media

Contents

In this chapter, we probe wave propagation in wet granular chain. This chapter is divided in three sections. The first section concerns the experimental study of wave propagation in wet chain over a broad range of static compressions and viscosities of fluids. In the second section, we derive appropriate contact model between wet spheres, which qualitatively and quantitatively describes our experimental observations. In the third section, we present additional experimental results concerning wave propagation in wet chain.

5.1 Raw experimental data

As in chapter 3, we probe dynamics of compressed granular chain made of polyacetal spheres supported by steel rods. We create wet granular media by adding small amount (less then 1 mm^3) of viscous fluid at each contact between spheres, see Fig. 5.1(a). Due to capillary forces F_{cap}, see Sec. 2.4.1, the fluid remains at the contact between spheres, see Fig. 5.1(b), as long as the weight of the droplet remains negligible, $mg < F_{cap}$. Here, we use Rhodorsil fluid [111] with viscosity μ equals to 0.1, 0.2, 0.5, 1, 5 and 10 Pas.

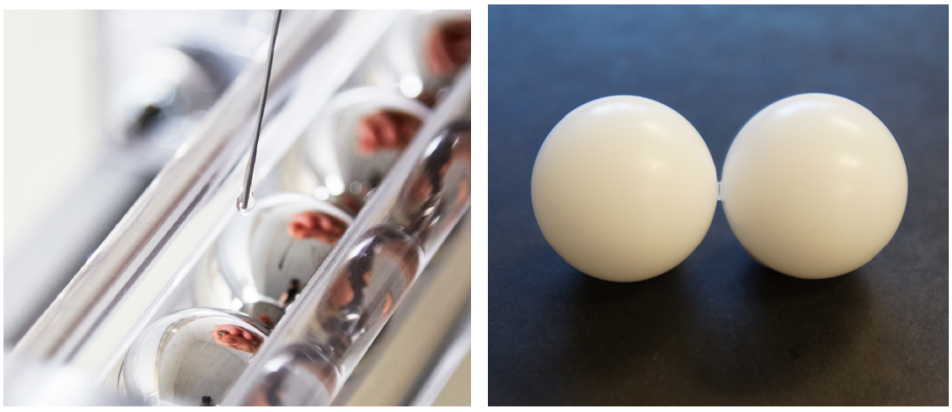

(a) (b)

Figure 5.1: (a) Small quantity of viscous fluid (Rhodorsil 47V) is poured between each sphere in contact. (b) A viscous meniscus of fluid shown between two polyacetal spheres.

Our experimental procedure is the same as for dry granular media (chapter 3). At first by sending large band energetic signal in from of chirp one obtains experimental transfer function H. Next one generates analytic gaussian pulse $F_{pulse}(x = 0, t)$ centered in the middle of passing band of dry system at $f_c = (f_{min}(F_0) + f_{max}(F_0))/2$ (where $f_{min}(F_0), f_{max}(F_0)$ are the theoretical values see Sec. 4.2, F_0 is static force). Here we send additionally pulse centered at $f_{c1}, f_{c2} \pm 20\% f_c$. Both signals, H and $F_{pulse}(x = 0, t)$, serve for estimation of output signal $F_{pulse}(x = L, t)$ (see Sec. 4.1.4). Then by estimating envelope of $F_{pulse}(x = 0, t)$ and $F_{pulse}(x = L, t)$ (by Hilbert transform); from time of flight of maximum envelope one obtains group velocity c_g while it's ratio quantifies loss factor η.

Experimental results are obtained for static force, F_0, varying from 5 N, every 5 N, up to 40 N and for viscosity μ of 0.1 0.2 0.5 1 5 and 10 Pas. Firstly on Fig. 5.2 we trace magnitude of experimental transfer functions. In Fig. 5.2(b) we show magnitude of $H = F_{out}/F_{in}$ for fluid with viscosity of 10 Pas with varying compression. While on Fig. 5.2(c) we present transfer function for fixed compression F_0 =5 N and different viscosity. As the comparison we trace also $|H|$ for dry chain Fig. 5.2(a).

We remark that addition of the small amount of fluid increases the attenuation by about 20 dB when compared to the dry case. As observed on Fig. 5.2 dynamics of wet chain depends on the static force applied Fig. 5.2(b) and on viscosity Fig. 5.2(c). The passing band in the wet case shifts with static force Fig. 5.2(b), while attenuation depends both on compression and viscosity Fig. 5.2(b)(c).

If we focus on low and height cutoff frequency (below/above 2 kHz) one observes that in low frequency region, which quantifies interaction between the sphere and support (section 4.1.1) is not significantly changed in the wet chain when compared to the dry case.

We remark also that the high frequency region (above 2 kHz) changes with static force. For high compression, see Fig. 5.2(b) wet system tends to present cutoff frequency characteristic for the dry chain, see Fig. 5.2(a), while for low static force applied H decreases with frequency.

Next, we trace the temporal representations of a gaussian pulses $F_{pulse}(x = L, t)$ as a function of viscosity and for compression of 5 N in Fig. 5.3 while the compression is 40 N in Fig. 5.4. As comparison in Figs. 5.3(a),5.4(a) we trace $F_{pulse}(x = L, t)$ estimated in dry chain. Here one clearly see that wave propagates faster in wet case when compared to dry case Figs. 5.3(a),5.4(a), signals arrives faster. One observes in addition that c_g increase with viscosity. Additionally signals in wet chain are more attenuated when compared to dry case.

Finally, we focus on group velocity and loss factor for all viscosities η and static force F_0. On Fig. 5.5 we show c_g and η in function of viscosity and static force applied, where central frequency of pulse is f_c. As observed on Fig. 5.5(a) group velocity increase in the wet case up to 50% for the high viscosity when compared to dry case. From Fig. 5.5(a) we remark that for the lowest viscosity group velocity depends nonlinearly to static force applied, while for higher values group velocity is independent to compression. Loss factor in wet case Fig. 5.5(b) for the lowest compression is three times bigger when compared to the dry case, while the difference between loss factor in the dry and wet media decrease in function of the static force F_0.

5.2 Contact model between loaded wet spheres

In the first section we experimentally estimated the group velocity and the loss factor of wet granular media. Here we aim at deriving an expression for the mechanical impedance which quantifies the potential interaction between wet spheres, in order to provide a

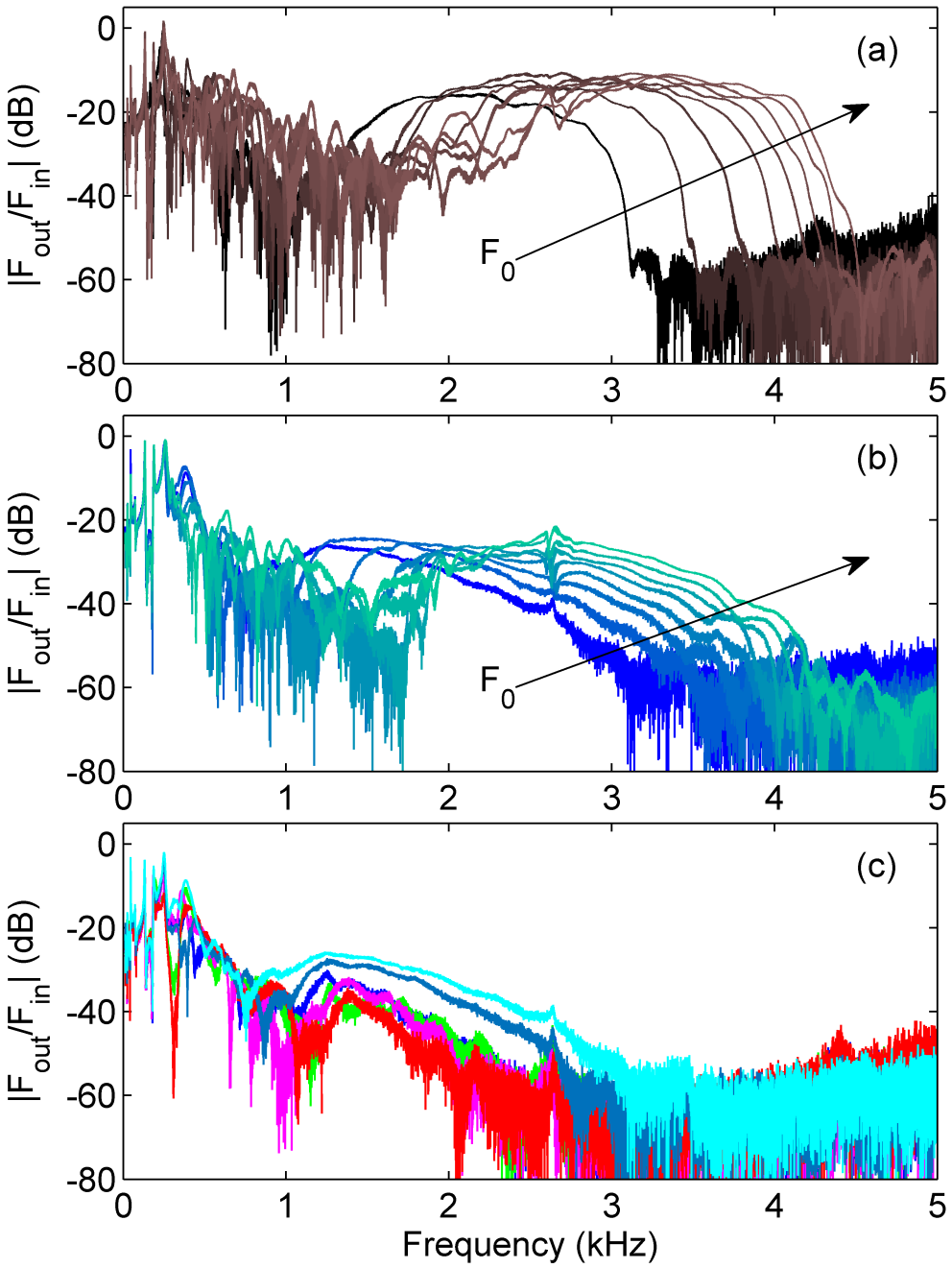

Figure 5.2: Magnitude $|H|$ of the transfer function $H = F_{out}/F_{in}$ versus frequency. (a) In the dry case for different static force F_0. (b) In the wet case as a function of F_0 for viscosity $\mu = 10$ Pas.(c) In the wet case at $F_0 = 5$ N, but for viscosity of 0.1, 0.2, 0.5, 1, 5 and 10 Pas, shown respectively in green, blue, magenta, red, light blue and cyan curves.

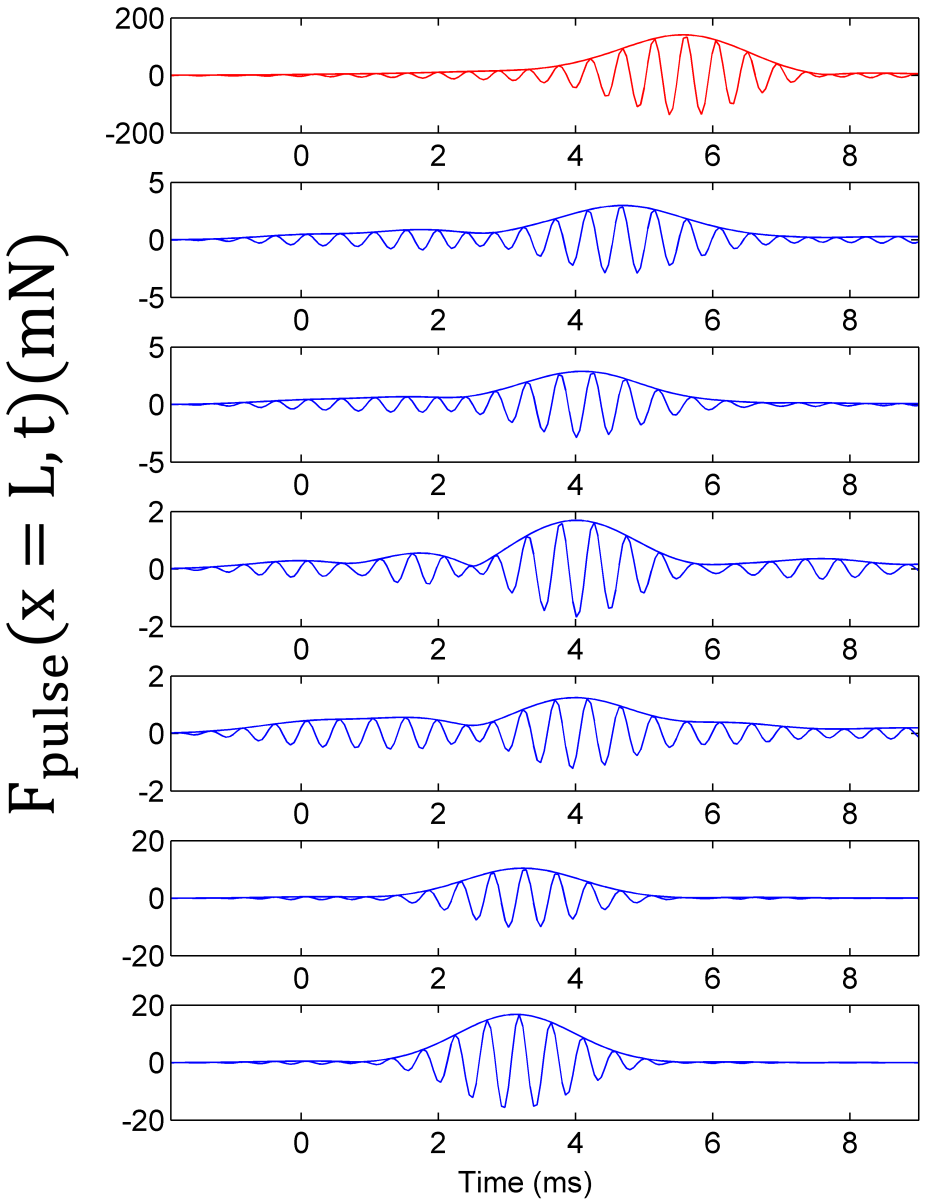

Figure 5.3: (a) Output deconvolved wavepacket $F_{pulse}(x = L, t)$ in the dry media. In (b), (c), (d), (e), (f) and (g): output signals for wet media for viscosity of $\mu = 0.1, 0.2, 0.5, 1, 5$ and 10 Pas; Here the static force is $F_0 = 5$ N. The wavepackets are centered at $f_c = 2.2$ kHz.

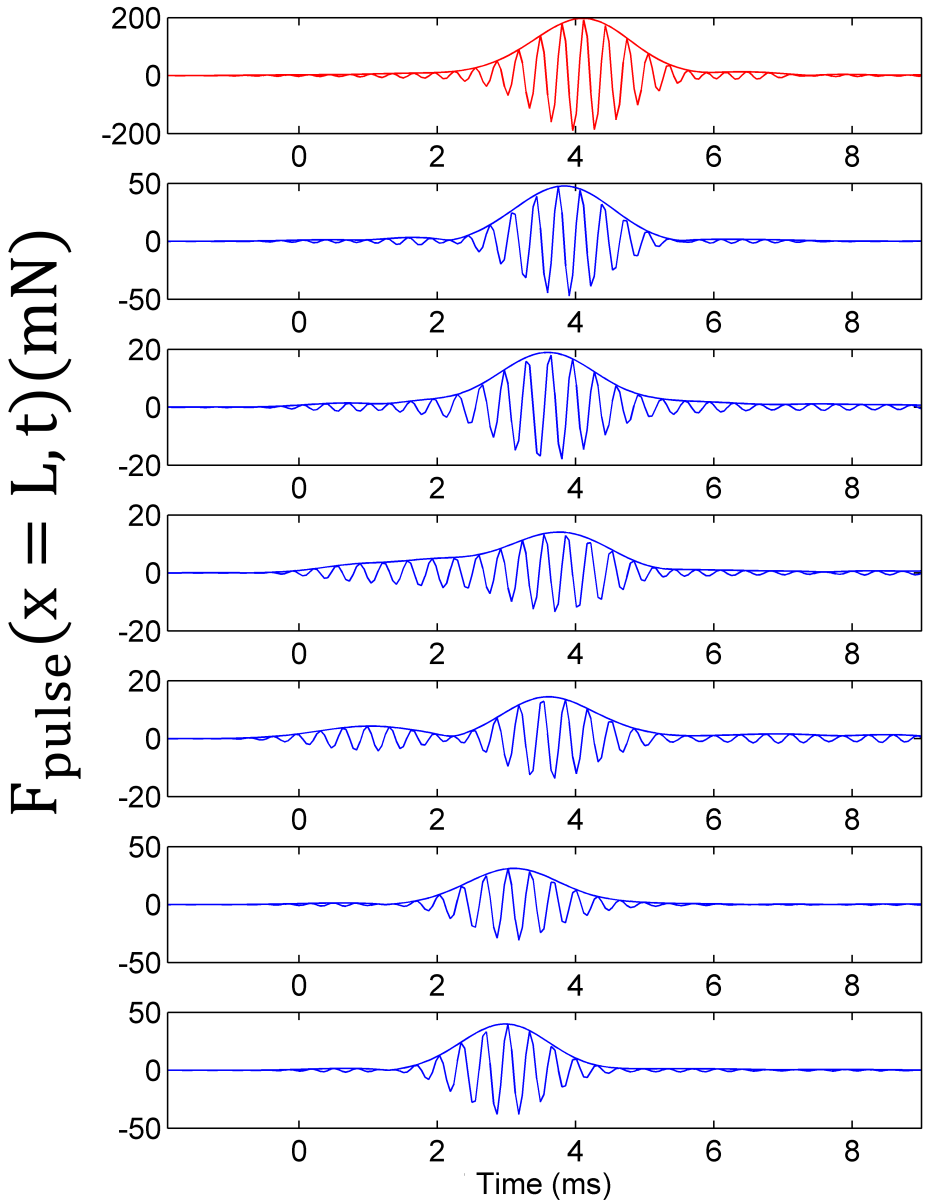

Figure 5.4: (a) Output deconvolved wavepacket $F_{pulse}(x = L, t)$ in the dry media. In (b), (c), (d), (e), (f) and (g): output signals for wet media for viscosity of $\mu = 0.1, 0.2, 0.5, 1, 5$ and 10 Pas; Here the static force is $F_0 = 40$ N. The wavepackets are centered at $f_c = 3.2$ kHz.

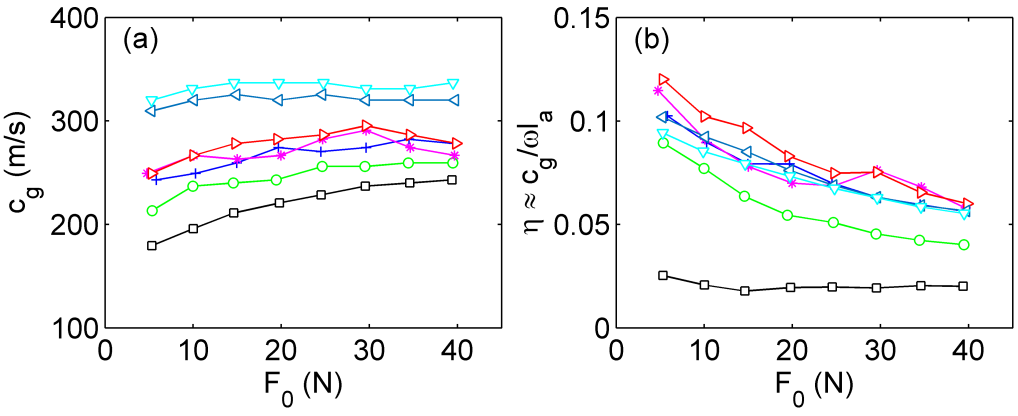

Figure 5.5: (a) Group velocity c_g and (b) loss factor $\eta = c_g/\omega l_a$ at central frequency f_c. The dry case is shown in black squares, the wet cases with viscosity of 0.1, 0.2, 0.5, 1, 5 and 10 Pa.s are traced respectively in green $\circ$, blue $+$, magenta $*$, red $\triangleright$, light blue $\triangleleft$ and cyan $\triangledown$.

theoretical expression for c_g and η. The theoretical estimations are obtained by probing the difference between the dry and the wet configurations.

5.2.1 Identification of the mechanical impedance between wet contacts

Here, we intend to provide a framework to describe our results. We follow the strategy derived in see Sec. 4.1.1. In the long wavelength approximation, the dispersion relation in a wet chain of spheres with radius R_0, Young's modulus E_0 and mass M is

$$M\omega^2 \simeq k_w q_w^2 (2R_0)^2 + k_0^2, \tag{5.1}$$

where q_w is the wet wave number, k_0 is the on-site stiffness and k_w is the mechanical impedance, i.e. the stiffness, between two wet particles. In turn, the dispersion relation in the dry alignments

$$M\omega^2 \simeq k_H q_d^2 (2R_0)^2 + k_0^2, \tag{5.2}$$

where q_d is the wet wave number and $k_H \simeq ER(F_0/ER^2)^{1/3}$ is the hertzian stiffness between two dry spheres, see Eq. 2.20.

In the following, we will assume that the mechanical impedance in the wet case, k_w, has two origins, as depicted in the sketch shown in Fig. 5.6: (i) an elastic contribution k_H that comes from the central region of the contact between particles under static load and (ii) an additional term κ_w due to the presence of the fluid at the periphery and which remains to be identified. In this case Eq. 5.1 becomes

$$M\omega^2 \simeq (k_H + \kappa_w)(2R_0)^2 q_w^2 + k_0^2, \tag{5.3}$$

Similarly to the expression given in Eq. 4.15, we introduce a complex wave number

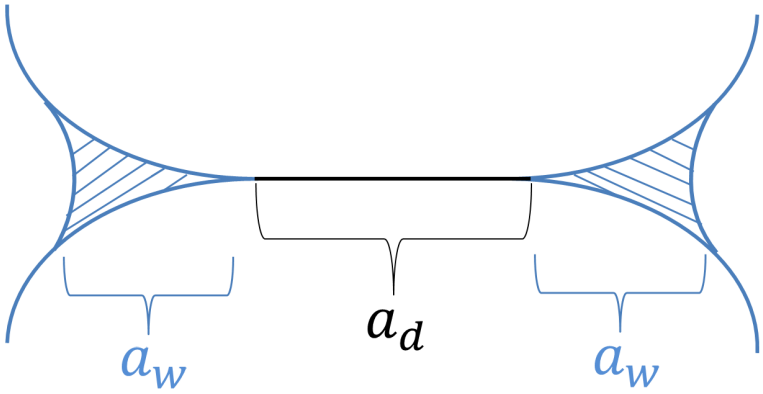

Figure 5.6: Sketch of the contact region between two compressed wet spheres. Here, a_d is the extent of the dry contact while a_w indicates the extent of the hydrodynamic field in the fluid. Such a framework is compatible with the one given by Marshall [63].

$q_d = (\omega/c_d)\times(1-i\eta_d)$ in the dry case and a complex wave number $q_w = (\omega/c_w)\times(1-i\eta_w)$ in the wet case, where $c_{d,w}$ stand for group velocities and $\eta_{d,w}$ are loss factors in dry and wet case. Subtracting Eq. 5.2 from Eq. 5.3, one simply obtains,

$$(k_H + \kappa_w)q_w^2 \simeq k_H q_d^2, \tag{5.4}$$

which equivalently provides a relation between c_d, c_w, η_d, η_w, k_H and κ_w,

$$\left[\frac{c_w}{c_d}\frac{(1-i\eta_d)}{(1-i\eta_w)}\right]^2 \simeq 1 + \frac{\kappa_w}{k_H}. \tag{5.5}$$

Within the assumption of weak dissipation $\eta_{d,w} \ll 1$, Eq. 5.5 becomes

$$(c_w/c_d)^2[1 + 2i(\eta_w - \eta_d)] \simeq 1 + \kappa_w/k_H. \tag{5.6}$$

Identifying the real and the imaginary parts of Eq. 5.6, one finally obtains

$$(c_w/c_d)^2 \simeq 1 + \Re(\kappa_w/k_H), \tag{5.7}$$

$$(\eta_w - \eta_d) \simeq \frac{\Im(\kappa_w/k_H)}{2\,[1 + \Re(\kappa_w/k_H)]}. \tag{5.8}$$

As a crude attempt to verify if the framework given by Eq. 5.7 and Eq. 5.8 is reliable, we plot the non-dimensional ratio of group velocities $(c_w/c_d)^2-1$ as a function of the main characteristics of a sample. The response of the system depending on the confinement pressure $P = F_0/\pi R_0^2$, on the viscosity of the fluid μ and on the angular frequency ω, see Fig. 5.5, one natural choice is to consider a non-dimensional parameter defined as $\mu\omega/P$ as the control parameter. The plot is shown in Fig. 5.7. Not surprisingly, all the data shown in Fig. 5.5(a) appear to collapse in a single master curve. A deeper inspection shows that the group velocity ratio increases as a power law of the non-

dimensional parameter, $[(c_w/c_d)^2 - 1] \propto (\mu\omega/P)^{1/3}$. Interestingly, the exponent 1/3 appears compatible with the models presented in Sec. 2.4.

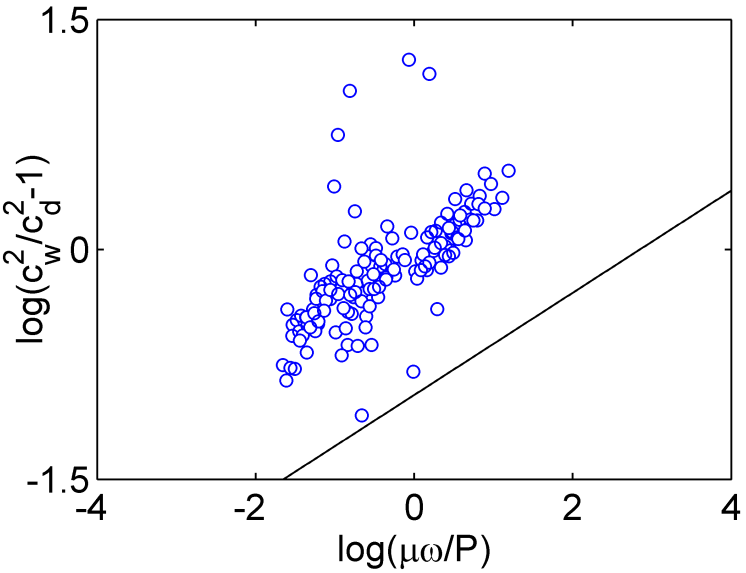

Figure 5.7: Ratio between the group velocity in the wet case c_w and the dry case c_d traced as a function of the viscosity μ, angular frequency ω and confinement pressure $P = F_0/\pi R_0^2$. The experimental data are traced for all static forces F_0, viscosity μ and central frequencies f_c, f_{c1} and f_{c2}. The black line is a guide line indicating a power law with and exponent 1/3.

5.2.2 Estimation of the mechanical impedance between wet contact

Here we aim at deriving an estimation of the mechanical impedance between loaded wet contacts, based on the description given in Sec. 2.3.2 and in Sec. 2.4.4. The analysis derived in Sec.5.2.1 shown that κ_w depends on properties of the fluid and elasticity of spheres. These findings are compatible with the elastohydrodynamic description provided by the group of Charlaix, see for instance [26, 81].

One has to mention that our experimental conditions differ from the conditions described in [26, 81]. In our configuration, the particles are in direct contact and submitted to a static load in the normal direction. The latter has to be taken into account in the description.

On purpose, we consider an elastic sphere with effective values of radius R and Young's modulus E pressed against another sphere, with a static force F_0. A small drop of liquid with viscosity μ stands right at the contact. Under the static compression, the fluid escapes the central region of the contact where the particles touches. This central region is a disk with radius a_d, see the sketch shown in Fig. 5.6. However, it stands to reason that some fluid may be trapped within the asperities and the roughness of the spheres,

i.e. one still has an arbitrarily thin layer of fluid between the solids. In any cases, owing to the strong confinement, the fluid trapped in the central region of the contact between the particles does not flow, the interaction potential between particles thus results in a stiffness given by Eq. 2.20

$$k_H = ER\left(\frac{6F_0}{ER^2}\right)^{1/3}, \tag{5.9}$$

over a radial extent $a_d = \sqrt{R\delta_0}$, where δ_0 is the overlap distance.

In turn, at the periphery of this central region, an annular capillary bridge of fluid surrounds the solid contact. Such a framework is compatible with the description given by Marshall [63]. When submitted to a perturbation in the normal direction, the peripheral fluid is squeezed out in the radial direction. As in Sec. 2.4.3, we start from the Reynolds equation [66], see for instance the Eq. 2.59,

$$\frac{\partial}{\partial r}\left(\frac{rh^3}{12\mu}\frac{\partial p}{\partial r}\right) = r\dot{h} \tag{5.10}$$

where r is radial coordinate, h is the fluid thickness, $\dot{h}$ is the normal velocity and p is the hydrodynamic pressure.

The fluid standing at the periphery of the solid contact, $r \geq a_d$, its thickness can be defined as

$$h(r \geq a_d) \simeq D + \frac{r^2 - a_d^2}{2R}, \tag{5.11}$$

where D is the arbitrarily thin thickness of the fluid trapped in the central region $r \leq a_d$. Thus, the integration of Eq. 5.10 gives

$$\frac{rh^3}{12\mu}\frac{\partial p}{\partial r} = \frac{r^2\dot{h}}{2} + \text{const}, \tag{5.12}$$

where the integration constant can be found from the Stokes equation $\partial_r p = \mu\partial_{zz}^2 v_r \propto -\mu v_r/h^2$, where v_r is the radial velocity of the squeezed fluid. At the edge of the capillary bridge, the radial velocity of the fluid is zero, i.e. $\partial_r p(r = a_d) = 0$, such that const $= -a_d^2\dot{h}/2$. It turns out that the pressure gradient becomes

$$\frac{\partial p}{\partial r} = \frac{6\mu\dot{h}}{rh^3}\left(r^2 - a_d^2\right), \tag{5.13}$$

and the pressure, once integrated over $r \geq a_d$, is

$$p \simeq -\frac{3\mu\dot{h}R}{h^2} + \frac{\mu\dot{h}a_d^2}{h^3}. \tag{5.14}$$

The second term in the right hand side of Eq. 5.14 is an approximation found by assuming D as arbitrarily small, $D \to 0$, and by considering $h(r) \gg \delta_0$, i.e. $r \geq 3a_d$, such that $h(r) \simeq r^2/2R$ in first approximation. Finally, the integration of the pressure

given by Eq. 5.14 provides the viscous repulsive force exerted by the peripheral fluid,

$$F_w \simeq \frac{6\pi\mu R^2 \dot{h}}{D}\left(1 - \frac{a_d^2}{6RD}\right). \tag{5.15}$$

This force is similar to the one found in Eq. 2.61, but minored by the term in parenthesis: the fluid here extends over a smaller region than in Sec. 2.4.3. In turn, the mechanical impedance $\kappa_w = F_w/h$ of the peripheral fluid thus becomes

$$\kappa_w(h) \simeq \frac{6\pi\mu R^2 \omega}{D}\left(1 - \frac{a_d^2}{6RD}\right), \tag{5.16}$$

and one recovers a result which is compatible with the description given by Marshall [63].

At arbitrarily small thickness D the elastic confinement of the fluid clamped at the periphery of the solid contact occurs, see Sec. 2.4.4 and Sec. 2.4.5: both elastic solids deform upon the action of the hydrodynamic pressure generated by the very large viscous shear and stress near the geometrical singularity, at the edge of the disk of solid contact. According to the description given in Sec. 2.4, when the thickness D tends to the crossover thickness $D_c = 8R(\mu\omega/E)^{2/3}$, see Eq. 2.72, the elastohydrodynamic interaction between the fluid and the elastic solids implies that the mechanical impedance given by Eq. 5.16 tends to

$$\kappa_w \simeq 1.163\left(\sqrt{3}+i\right)\frac{6\pi\mu R^2\omega}{D_c}\left[1 - \frac{1}{3}\left(\frac{a_d}{a_w}\right)^2\right], \tag{5.17}$$

where $a_w = \sqrt{2RD_c}$ is the typical extent of the fluid's flow, see for instance Eq. 2.62.

From now on, adding the elastic repulsion coming from the central region of solid contact, see Eq. 5.9, to the viscous repulsion of the peripheral fluid given by Eq. 5.17, and assuming that the fluid extends significantly above the region of solid contact, $a_w \gg a_d$, one finds the overall mechanical impedance of a wet contact between two statically loaded spheres, $k_w = k_H + \kappa_w$, such that

$$k_w \simeq ER\left(\frac{6F_0}{ER^2}\right)^{1/3} + 1.163\left(\sqrt{3}+i\right)\frac{6\pi\mu R^2\omega}{D_c}. \tag{5.18}$$

It turns out that, according to Eq. 5.7 and Eq. 5.8, the ratio of wet to dry group velocity and the difference of the loss factors become

$$(c_w/c_d)^2 \simeq 1 + \alpha(\mu\omega/P)^{1/3}, \tag{5.19}$$

$$(\eta_w - \eta_d) \simeq \frac{\beta(\mu\omega/P)^{1/3}}{1+\alpha(\mu\omega/P)^{1/3}}, \tag{5.20}$$

where $P = F_0/\pi R_0^2$ is the confinement pressure and α and β are constants of the order of unity, $\alpha \sim \beta \sim 1$. These results are consistent with the trend of the experimental data demonstrated in Fig. 5.7.

It is worth mentioning that strictly speaking, the square bracketed correction term in in Eq. 5.17 can be safely neglected if $(a_w/a_d) \geq \sqrt{10/3} \simeq 1.8$. Within our experimental

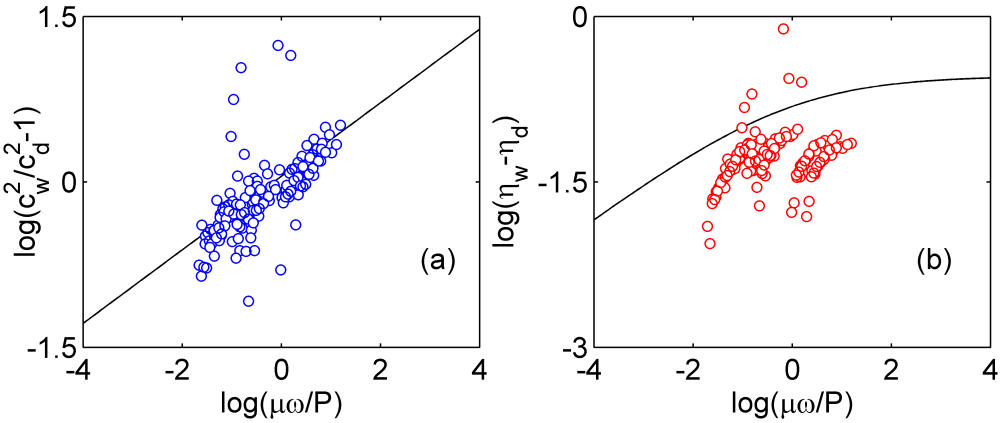

Figure 5.8: (a) Ratio between the group velocity in the wet case c_w and in the dry case c_d; the experimental data are traced in blue dots. (b) Difference between loss factor in the wet case η_w and in the dry case η_d; the experimental data are traced in red dots. In both cases, the data are represented as a function of viscosity μ, angular frequency ω and confinement pressure $P = F_0/\pi R_0^2$. Experimental data are traced for all static forces F_0, viscosity μ and central frequencies f_c, f_{c1} and f_{c2}. The black line represents the theoretical estimations from Eq. 5.19 and Eq. 5.20.

conditions, this assumption is fulfilled at low confinement pressure or high fluid viscosity only, since $(a_w/a_d) \propto (\mu\omega/P)^{1/3}$. At large pressure or low viscosity, the correction term should be taken into account, though we do not do it in practice. The limit of arbitrarily high pressures or arbitrarily small viscosity indeed corresponds asymptotically to the behavior of a dry contact: the description given in Eq. 5.18 actually matches this limit, though our model remains beyond the required precision to account for a reliable crossover between dry and wet regimes. In practice, the typical extent of the dry solid contact a_d lies in between 200 μm and 400 μm at lowest and highest confinement pressures, respectively. In turn, the characteristic extent of the the fluid's flow is a_w is 200 μm at the lowest viscosity $\mu = 0.1$ Pa.s: in this case, $a_w < a_d < 2a_w$ and the assumption is not fully valid. However, at the the highest viscosity $\mu = 10$ Pa.s, the typical extent of the fluid's flow is $a_w \simeq 1$ mm such that $2.5 < a_w/a_d < 5$, in agreement with the assumption leading to Eq. 5.18.

5.3 Experimental validation

5.3.1 Group velocity and loss factor

In this part we confront the descriptions given in Sec. 5.2 with our experimental results. The full comparison between all the experimental data shown in Fig. 5.5 and the theoretical expressions given by Eq. 5.19 and by Eq. 5.20 is presented in Fig. 5.8 as a function of the non-dimensional parameter $\mu\omega/P$. One observes that the theoretical description is in fair agreement with the experimental observations, for both the group velocity and

the loss factors. In Fig. 5.8(a), the estimations given by Eq. 5.18 provides qualitatively and quantitatively the master curve found in Fig. 5.8. In addition, we observe that the description also provides the correct order of magnitude and the correct trend for the difference of the loss factors, see Fig. 5.8(b), though the data are more scattered. According to Eq. 5.19 and Eq. 5.20, both the relative difference of group velocity and the difference of the loss factors increases as a power law of the non-dimensional parameter $\mu\omega/P$.

5.3.2 Dispersion relation

Having validated experimentally the theoretical description, we present additional experiments and comparisons between the dynamics of dry and wet chains. Using our embedded sensor, we record the dynamic force as a function of time and position inside an alignment of 40 wet polyacetal spheres supported by steel rods. As in previous Sec. 4.2.2, we excite the medium with a chirp. The force is registered at the beginning of the chain $F_{in}(t) = F(x = 0, t)$, at the end $F_{out}(t) = F(x = L, t)$ and by the embedded sensor $F_{emb}(x, t)$ at any position $x = 2nR$ with $1 \leq n \leq 40$. This experiment is performed with the three highest fluid viscosity, $\mu = 1$ Pas, $\mu = 5$ Pas and $\mu = 10$ Pas. For the two last fluids, we record the force at the first 10 particles only. In all cases, the static compression is 20 N.

At first, one analyzes the results obtained with an interstitial fluid with a viscosity equal to 1 Pas. In Fig. 5.9(a) and in Fig. 5.9(b), we show the dispersion relation $K(\Re(q), \omega) = \mathrm{FT}_{tx}[F_{emb}(x, t)]$, estimated according to the method described in Sec. 4.2.1, for dry and wet configurations respectively. Here the fluid viscosity is $\mu = 1$ Pa.s. In Fig. 5.9(c) and in Fig. 5.9(d), we plot the modulus of the transfer function, $H(x, \omega) = \mathrm{FT}_t[F_{emb}(x, t)]$, as a function of the position x and frequency ω, see Sec. 4.2.1, for dry and wet chains respectively. One can see that the wet medium is more dissipated than the dry medium: the decay as a function of the position is faster and more pronounced; in addition, the decay is faster at higher frequencies. As observed on the dispersion relations shown in Fig. 5.9(a,b), the low frequency region remains almost unaffected by the presence of fluid, in agreement with the fact that the mechanical impedance of the wet contact tends to the stiffness of a dry contact at low frequency, see Eq. 5.18. On the opposite, the overall slope of the dispersion relation is larger with fluid than in the dry case: this suggests that the fluid stiffens the contact and significantly increases the group velocity. Finally, on can still observe the spurious bending mode of the supports in the low frequency region of the dispersion relation of bending modes, as in the dry case detailed in Fig. 4.12.

Then, as a crude probe of the attenuation of waves, as they propagate inside the alignments, we deconvolve the measured transfer function $H(x, \omega)$, obtained from the chirp excitation, with the Fourier transform of an analytic incident gaussian pulse $F_{pulse}(x = 0, t)$ centered in the middle of the propagative band in order to obtain a time resolved propagated pulse $F_{pulse}(x, t)$, see the details of the method in Sec. 4.1.4. One then extract the

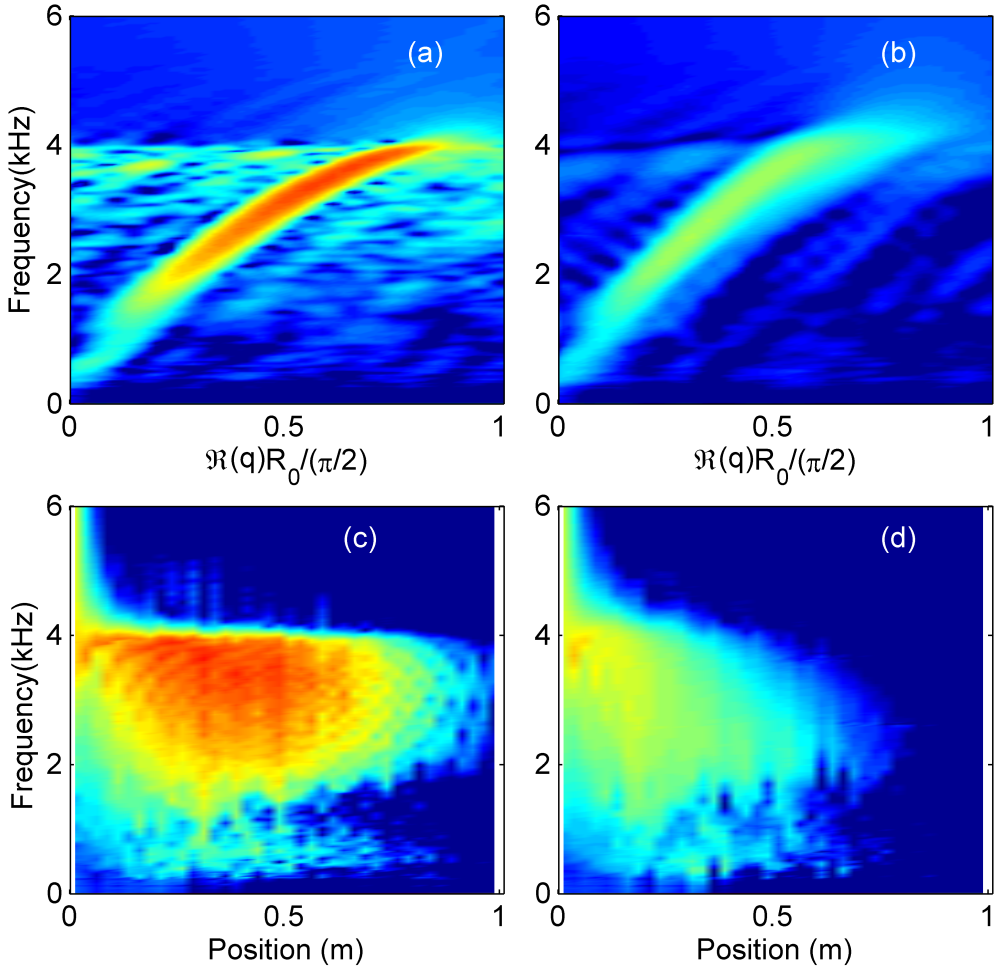

Figure 5.9: (a,b) Dispersion relation unraveled by the use of the embedded sensor in the dry and the wet cases, respectively. Here, the fluid viscosity is $\mu = 1$ Pa.s. (c,d) Modulus of the transfer function measured by the embedded sensor in the dry and the wet cases, respectively. Here, the static compression is 20 N and $\Re(q)$ is the real part of the wave number and R_0 is the radius of the spheres.

envelope of the pulse propagated from the Hilbert transform, $F^{env}_{pulse}(x,t)$, as detailed in Sec. 4.1.4. The envelop of such a signal is shown Fig. 5.10 as a function of propagated distance and as a function of time. One clearly sees that the time of flight is shorter with an interstitial fluid with viscosity $\mu = 1$ Pa.s than in the dry case; the group velocity is significantly faster in presence of a fluid.

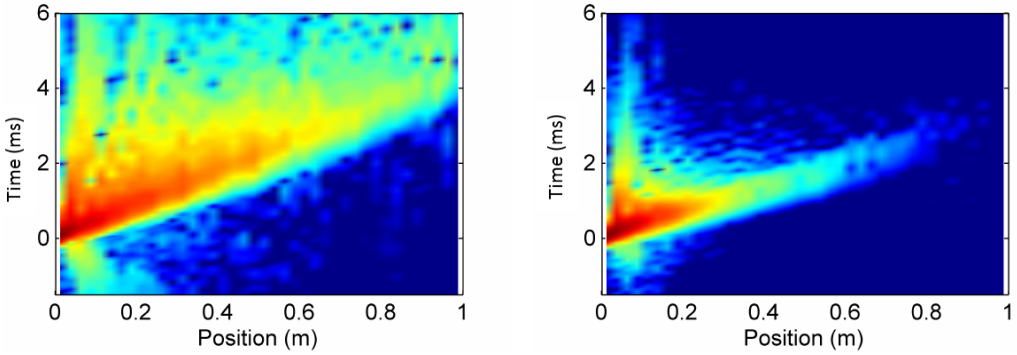

(a) (b)

Figure 5.10: Envelope of the wavepacket deconvolved from the response to a chirp excitation, as a function of position of the embedded sensor and time: (a) in a dry chain and (b) with an interstitial fluid with 1 Pas viscosity. Here, the alignments are both under a 20 N compression.

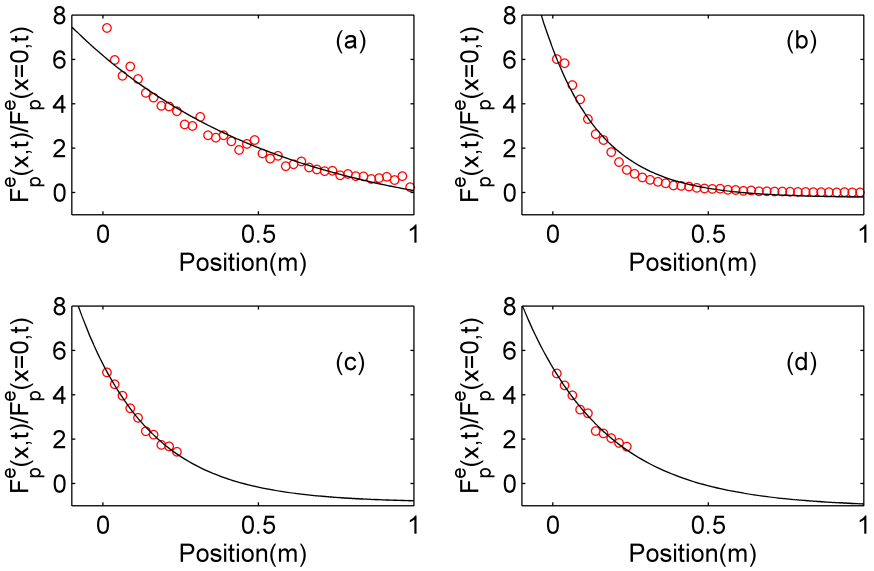

Figure 5.11: Evolution of the attenuation $\max[F^e_p(x,t)]/\max[F^e_p(x=0,t)]$ as a function of the position $x = 2nR$ inside the chain; experimental results are shown in red dots and the the black line stands for the Eq. 5.21. (a) Dry chain of spheres and in (b,c,d) wet chains of spheres with interstitial fluid with viscosity of 1 Pas, 5 Pas and 10 Pas, respectively. Here, the alignments are both under a 20 N compression.

At this point, one can finally extract the evolution of the maximum of the envelope of the deconvolved pulse as a function of the propagated distance. This result is presented in Fig. 5.11, for the dry configuration and for the three viscosities. These results are compared with the attenuation length l_a inferred from the ratio of the force deconvolved at the beginning and at the end of the chain,

$$\max[F^{env}_{pulse}(L,t)]/\max[F^{env}_{pulse}(0,t)] \approx e^{-L/l_a}. \tag{5.21}$$

One observes in Fig. 5.11 that the magnitude of the pulse decreases as a function of the propagated distance of the chain and attenuation measured at the end of chain gives the conform results. The extrapolation from the measurements at both extremities, see Eq. 5.21, demonstrates in all cases a fairly well defined exponential decay which matches the experimental data, our description, in term of an attenuation length is thus confirmed. It turns out that friction for instance would have led here to a non-exponential decay, which is not observed here.

5.4 Conclusions

In this chapter, we characterized wave propagation in wet alignments of spheres via careful measurements of the experimental transfer function H. From the knowledge of H, we measured the group velocity and the loss factor over a vast range of static forces, frequencies and fluid viscosities. By comparing the group velocity and the loss factor measured in wet and dry chains, we inferred a model of contact dynamics between wet load particles.

Our model shows that Hertz contact dynamics, which describes the propagation of waves in dry chains of spheres, commonly used in the literature, must be corrected by an elastohydrodynamic contribution [81] in the presence of a very small amount of interstitial fluid. Our interpretations and estimations are both in qualitative and quantitative agreement for the group velocity and a qualitative agreement for the loss factor.

Chapter 6

Waves in 3D granular packing

Contents

In this chapter, we present a preliminary experimental study on ultrasonic wave propagation in three-dimensional dry and wet granular media, in a setup shown in Fig. 6.1. In particular, we focus on the characterization of the wave speed c and the attenuation length l_a. This chapter is divided in three sections. In the first section, we expose a theoretical framework for the description of both the wave speed and the attenuation length in dry and wet case. In the second part, we present the experimental protocols and the results acquired at low or high frequencies and at low or high driving amplitudes. Finally, we compare the experimental results with the theoretical estimations derived in the first section.

6.1 Wave speed and attenuation in 3D granular media

6.1.1 Effective medium theory in dry and wet granular media

Firstly, we remind the model concerning wave propagation in three-dimensional dry granular media based on the effective medium theory (EMT) [101–105]. In EMT, the contact dynamics between grains is described by Hertz-Mindlin interaction [50]. In the presence of a normal confining pressure P, one has to consider not only the hertzian normal stiffness k_H but also a tangential stiffness k_t resulting from shear deformation of the contacts. The passage from the microscopic scale, at the level of the contact, to the macroscopic scale, in the long wavelength approximation, is provided by an effective bulk modulus K_e, an effective shear modulus μ_e and an effective density $\rho_e = \rho\Phi$, where Φ is the compaction of the packing of grains, ρ is the density of the material of the sphere, see Eq. 2.95 and Eq. 2.96. The longitudinal wave speed V_p is given by [7,9], see Eq. 2.93

$$V_p = \sqrt{\frac{K_e + 4/3\mu_e}{\rho_e}}, \tag{6.1}$$

where the effective moduli are

$$K_e = \frac{Z\Phi}{12\pi R_0} k_H, \tag{6.2}$$

$$\mu_e = \frac{Z\Phi}{20\pi R_0}(k_H + 3/2k_t). \tag{6.3}$$

Here, R_0 is the radius of the spheres and Z is the coordination number. In the case of frictionless spheres, one has $k_t = 0$. The normal and transverse contact stiffnesses are [7,9]

$$k_H = \frac{4aG_0}{1-\nu_0}, \tag{6.4}$$

$$k_t = \frac{8aG_0}{2-\nu_0}, \tag{6.5}$$

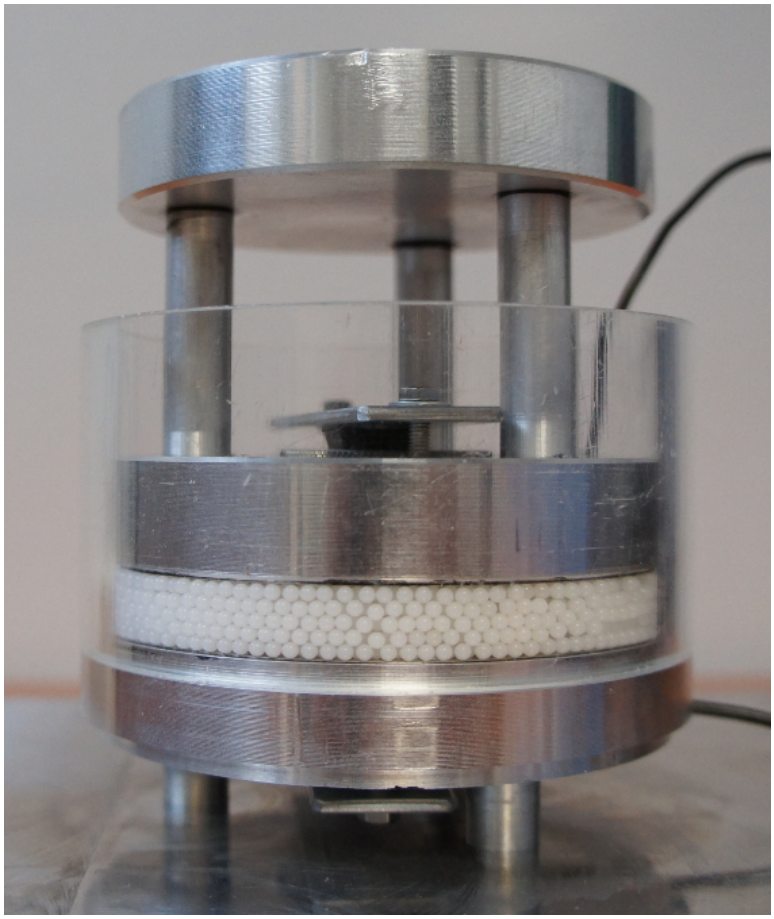

Figure 6.1: A five layers thick three-dimensional granular medium filled with 2 mm in diameter polyacetal spheres. A plane wave ultrasonic emitter is placed on the bottom of the sample and the receiver is fixed on the upper movable cap. The confinement pressure is exerted by placing different mass on the upper cylindrical part.

where, ν_0 is the Poisson ratio and G_0 is shear modulus

$$G_0 = \frac{E_0}{2(1+\nu_0)}. \tag{6.6}$$

The radius a of the contact disc is [7]

$$a = R_0 \left[\frac{3\pi(1-\nu_0)}{2Z\Phi G_0}P\right]^{1/3}, \tag{6.7}$$

where ν_0 is the Poisson ratio of the spheres. Under a confinement pressure P, the static force F_0 between grains is estimated at

$$F_0 = \frac{4\pi R_0^2 P}{Z\Phi}. \tag{6.8}$$

Starting from the EMT, which describes wave propagation in dry media, we attempt to extend the derivation to the wet configuration and find an expression for the longitudinal velocity in the presence of an interstitial fluid. On this purpose, one introduces the mechanical impedance between wet grains k_w, where k_w is the combination of Hertz stiffness k_H and the mechanical impedance κ_w estimated from the EHD theory [26],

$$k_w = k_H + \kappa_w, \tag{6.9}$$

where according to Eq. 5.17, κ_w is

$$\kappa_w = 1.163\left(\sqrt{3}+i\right)\frac{6\pi\mu R^2\omega}{D_c}\left(1-\frac{a_d^2}{3a_w^2}\right). \tag{6.10}$$

Here, $D_c = 8R(\mu\omega/E)^{2/3}$ is the critical distance, with effective values of sphere radius R and Young's modulus E. In this case we assume that $a_w > a_d$ (where a_w is the characteristic extent of the fluid and a_d is the characteristic extent of the dry contact) for ultrasonic frequency $f > 20$ kHz, for a fluid viscosity $\mu = 5$ Pas and for a confinement pressure $P \simeq 5$ kPa, such that Eq. 6.10 becomes

$$\kappa_w = 1.163\left(\sqrt{3}+i\right)\frac{6\pi\mu R^2\omega}{D_c}. \tag{6.11}$$

In analogy with the EMT, see Eq. 6.2 and Eq. 6.3, and assuming that the tangential stiffness is zero in presence of the lubricant, one finds the effective moduli K_{ew} and μ_{ew} as

$$K_{ew} = \frac{\Phi Z}{12\pi R_0}k_w, \tag{6.12}$$

$$\mu_{ew} = \frac{\Phi Z}{20\pi R_0}k_w, \tag{6.13}$$

and the longitudinal wave speed V_w in the wet granular media, see Eq. 6.1, finally becomes

$$V_w = \sqrt{\frac{K_{ew} + 4/3\mu_{ew}}{\rho_e}}. \tag{6.14}$$

6.1.2 Multiple scattering and attenuation in 3D samples

Here, we deal with the attenuation in three-dimensional dry granular media. In one-dimensional dry granular media, the attenuation of waves is mostly given by a loss angle of the bulk material of the spheres; in the wet case the dissipation mainly results from the elastohydrodynamic interaction. In three-dimensional configuration, an additional mechanism of attenuation is due to the scattering of waves on every grain. In this section, we derive an estimation of the attenuation length l_s which accounts for wave scattering; this will serve for the estimation of total attenuation length in both dry l_d and wet l_w three-dimensional granular media.

Let's consider an incident plane pressure wave $p_i(\omega, q_0)$, where q_0 is the incident wave number, scattered by a spherical obstacle with radius R_0, see Fig. 6.2. The magnitude of the scattered wave $p_s[\omega, q(\theta)] \propto f(\theta)$ depends on the angular coordinate θ.

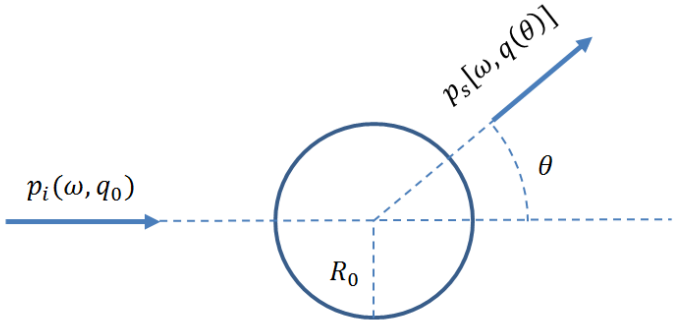

Figure 6.2: A plane wave scattered by a sphere.

The directivity function $f(\theta)$ defines the differential scattering cross section $\sigma(\theta)$, such that $|f(\theta)|^2 = d\sigma(\theta)/d\theta$ [112]. By integrating over all directions, one obtains the total scattering cross section,

$$\sigma_T = \int_0^{2\pi} |f(\theta)|^2 d\theta. \tag{6.15}$$

The scattering cross section is an effective area which can be compared to the real area of the spherical scatterer, $4\pi R_0^2$, and which provide a measure of its capacity to scatter an incident wave: the scattered energy is proportional to the scattering cross section σ_T. As a consequence, σ_T thus also provides a measure of the amount of energy the incident coherent wave lost to generate a scattered field in all directions [113]. In the independent scattering approximation [114], which assumes that each obstacle scatters independently the incident wave $p_i(\omega, q_0)$, one defines a characteristic decay length of the intensity of the coherent wave. This distance corresponds to the attenuation length

l_s. It is related to the total scattering cross section: the larger is the scattering cross section, the larger is the attenuation, i.e. the shorter is the attenuation length l_s. These quantity are formally related as [112]

$$l_s = \frac{1}{n\sigma_T}, \tag{6.16}$$

where n is the number of scatterers per unit volume. The compacity being $\Phi = 0.64 \simeq 2/3$ for a random loose packing of sphere and the volume of a sphere being $V_s = (4/3)\pi R_0^3$, the density n is thus

$$n \simeq \frac{1}{2\pi R_0^3}. \tag{6.17}$$

It is worth mentioning that the independent scattering approximation holds for weak concentrations of scatterers only, $n \ll 1$. Up to a certain extent, it is not fully applicable in the case of dense granular media. However, we retain this approximation as a lowest order estimation. In any case, the presence a very small volume fraction of an interstitial fluid does not affect the multiple scattering: analyzing the difference of attenuation between the wet and the dry configurations cancels out the effect of wave scattering.

In the long wavelength approximation limit, $\lambda \gg R_0$, which corresponds to the Rayleigh scattering regime [113], the cross section is such that

$$\frac{\sigma_T}{\pi R_0^2} \simeq \frac{7}{9} \left(q_0 R_0\right)^4. \tag{6.18}$$

The regime at which the wavelength is smaller than the radius of the scatterers, $\lambda \ll R_0$, corresponds to the geometrical limit [113], in which the cross section tends to

$$\frac{\sigma_T}{\pi R_0^2} \simeq 2. \tag{6.19}$$

By combining Eq. 6.16, Eq. 6.17 and Eq. 6.18, one obtains the attenuation length in the Rayleigh limit,

$$l_s = \frac{18}{7 q_0^4 R_0^3}, \tag{6.20}$$

and by combing Eq. 6.16, Eq. 6.17 and Eq. 6.19, one obtains l_s in the geometrical limit,

$$l_s = R_0. \tag{6.21}$$

Finally one can estimate the total attenuation length l_d in dry media as

$$\frac{1}{l_d} = \frac{1}{l_s} + \frac{1}{l_H}, \tag{6.22}$$

where l_H stands for the attenuation length due to the dissipation in the contacts, $1/l_H = -\Im(q) \simeq \Im(\omega/R_0\omega_{cut})$, where $\omega_{cut} = 2\sqrt{k_H/M}$.

In wet media, the total attenuation length l_w is

$$\frac{1}{l_w} = \frac{1}{l_s} + \frac{1}{l_H} + \frac{1}{l_{ehd}}. \tag{6.23}$$

where l_{ehd} is the attenuation length in the wet case, $1/l_{ehd} = -\Im(q) \simeq \Im(\omega/R_0\omega_w)$, where $\omega_w = 2\sqrt{k_w/M}$.

In turns out that the difference of attenuation between the dry and the wet configurations simply gives

$$\frac{1}{l_w} - \frac{1}{l_d} = \frac{1}{l_{ehd}}. \tag{6.24}$$

6.2 Experimental ultrasonic waves in 3D granular media

After having tackled the theoretical descriptions, we here focus on the experimental setup. We probe wave propagation in three-dimensional granular media made of polyacetal spheres with Young's modulus $E_0 = 4.25$ GPa and Poisson coefficient $\nu_0 = 0.38$. Here, the grains have a diameter $D_S = 2$ mm and are enclosed in a cylindrical container with radius $R_c = 4$ cm, see Fig. 6.3(a). The whole system is clamped between two steel cylinders; by placing different weight on the top cylinder cap, one changes the confinement pressure $P = (m + M)g/\pi R_c^2$, where m is the mass of the upper cylinder and M is the mass of an additional weight. We placed an ultrasonic emitter on the bottom part and an ultrasonic receiver on the upper part. Transducers are not in direct contact with granular media: a 0.25 mm thick steel sheet protects the transducers. This sheet is thin enough to be acoustically transparent.

6.2.1 Probing granular media at low frequency

In the first experimental study, we probe the sample by sending a short impulsion produced by an pulser-receiver (*Sofranel 5072PR*) to the emitting transducer, see Fig.6.3. Waves propagating through the granular medium are then received by a receiving transducer. This signal is amplified by a conditioner (*Sofranel 5072PR*) and transmitted to an oscilloscope (*Teledyne Lecroy HD0 4024*). We use two indentical plane wave and broadband receiving and emitting transducers (*Olympus V101*) centered on frequency $f = 0.5$ MHz.

Here, we probe wave propagation in the dry and wet granular media. We create a wet granular media by adding a very small amount of fluid with viscosity of $\mu = 5$ Pas between grains. The volume fraction of the liquid corresponds to a dozen of drops and is about $\varphi \simeq 0.05\%$. By carefully mixing the spheres, we ensure that the fluid is equally distributed in the sample.

In the main part of the experiment one pours from one to six layers of polyacetal spheres inside the cylindrical container. For each sample thickness, we compress and decompress by putting and removing the top cylinder on the granular sample, as to obtain

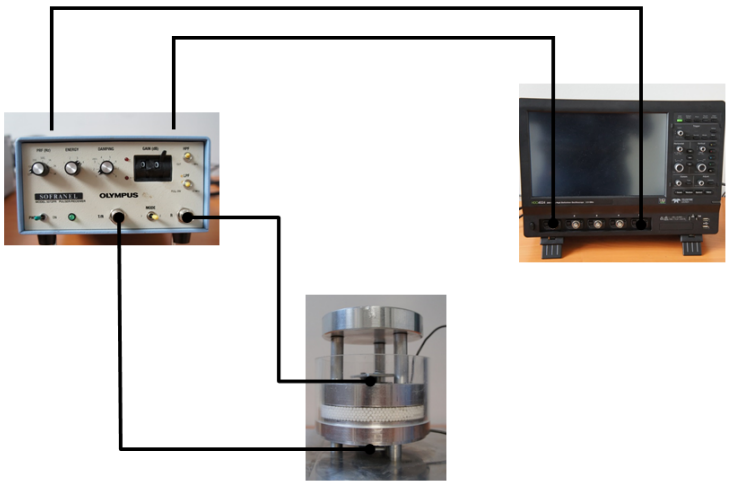

(a)

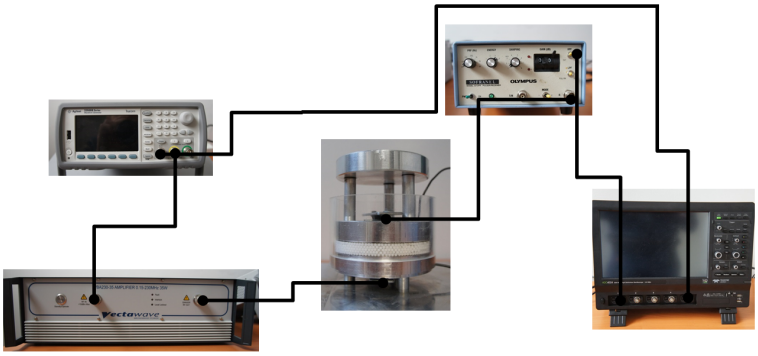

(b)

Figure 6.3: Sketch of the two experimental setups used to characterize ultrasonic wave propagation in granular media.(a) The emitter is connected to a pulser which drives the sample with a short broadband impulsion. (b) The emitter is connected to an arbitrary wave generator and an amplifier, which drive the medium with a long duration chirp.

the maximal achievable compacity. This procedure is repeated several times. Once the maximal compacity is obtained, $\Phi \simeq 0.64$, we place an $M = 2$ kg mass on the top cylinder. The mass of the top cylinder is $m = 530$ g, this generates a confinement pressure of about $P \simeq 5$ kPa. This pressure is far below the yield stress for our beads, see Eq. 2.24: the sphere would deform plastically with a mass larger than 50 kg, approximately.

Next, for each sample thickness, we repeat 8 times the acquisition of the transmitted signals. As an example shown in Fig. 6.4, we trace the mean value of the signals propagated through samples made of three or five layers of dry spheres. Here we trace also the envelope of the signal estimated with the Hilbert transform. The magnitude and the location of the maximum of the envelope, see the black stars in Fig. 6.4, serves for the estimation of the wave speed c and the attenuation length l_a.

We obtain c from the slope of the curve giving the time of flight (Tof) of the maximum of the envelope as a function of the thickness of the samples e. The attenuation length l_a is obtained from the slope of the curve giving the natural logarithm of the magnitude of the envelope, $ln(A_{max})$, as a function of the thickness of the sample e.

It is worth to mention that by tracing the Fourier transform of the signals transmitted through three and five layers, as shown in Fig. 6.5, one observes that the signals mostly contains very low frequency content, approximately centered on 30 kHz. The latter is due to the very strong and frequency dependent attenuation of the signals (Eq. 6.20) and the inefficiency of a short impulsion to properly excite the media: only the very low frequency content is detectable. However, we turned this pitfall in our advantage, and we used these signals to analyze the response of the media in the low frequency range. The response of the media at higher frequency is analyzed, via a more appropriate protocol, in the next subsection. From the estimation of the wave speed in a dry media within the experimental conditions, $c \simeq 200$ ms^{-1} see Eq. 6.1, we estimate the wavelength $\lambda = c/f$ at about $\lambda \simeq 6.5$ mm at 30 kHz: this corresponds to the long wavelength approximation $\lambda > R_0 = 1$ mm.

At first, we probe our granular media with low amplitude impulsions, in order to ensure the linearity of the response: the magnitude of the pressure wave must remain well below the confinement pressure. The experimental results for the wave speed are presented in Fig. 6.6 while in Fig. 6.7, we show the results for the attenuation length. By estimating the slope of the curves in Fig. 6.6, one obtains a wave speed $c_d \simeq 180$ ms^{-1} in the dry case. In wet granular media, the experimental wave speed is $c_w \simeq 344$ ms^{-1}. From the slope of the curve shown in Fig. 6.7, we measure the attenuation length l_a. Unfortunately, the results shown in Fig. 6.7 are too noisy, especially for the 5 and 6 layers. Thus as to increase the quality of the signal, we increased the amplitude by a factor five.

Next, we present experimental observations with impulsions at larger amplitudes. The results for the wave speed are presented in Fig. 6.8 while in Fig. 6.9 we show the results for the attenuation length. Here, we obtain wave speeds at about $c_d \simeq 435$ ms^{-1} in the dry case and $c_w \simeq 305$ ms^{-1} in the wet case. The attenuation length in the dry media is $l_d \simeq 4.76$ mm, while in the wet case one obtains, $l_w \simeq 2.44$ mm.

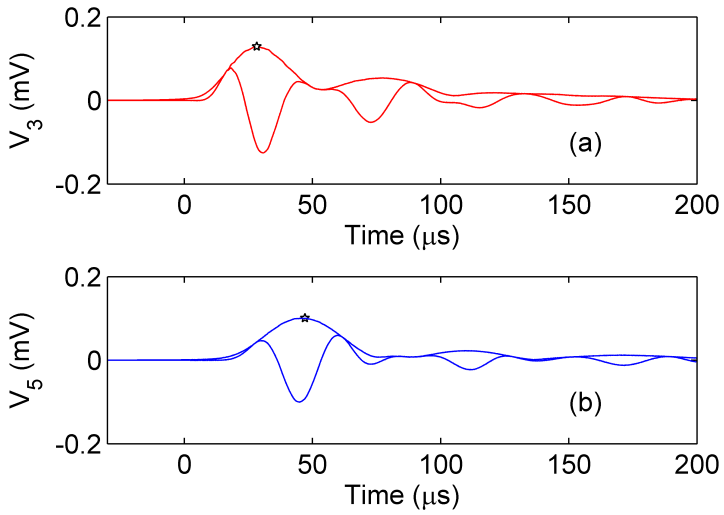

Figure 6.4: Example of signals propagating through (a) three and (b) five layers of polyacetal spheres. Black stars show the maximum of the envelope.

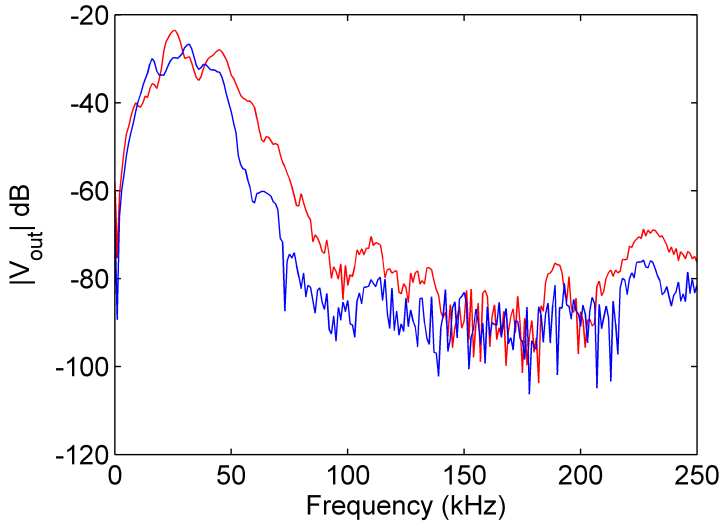

Figure 6.5: Example of Fourier transform of signals propagating through three (red curve) and five (blue curve) layers of polyacetal spheres.

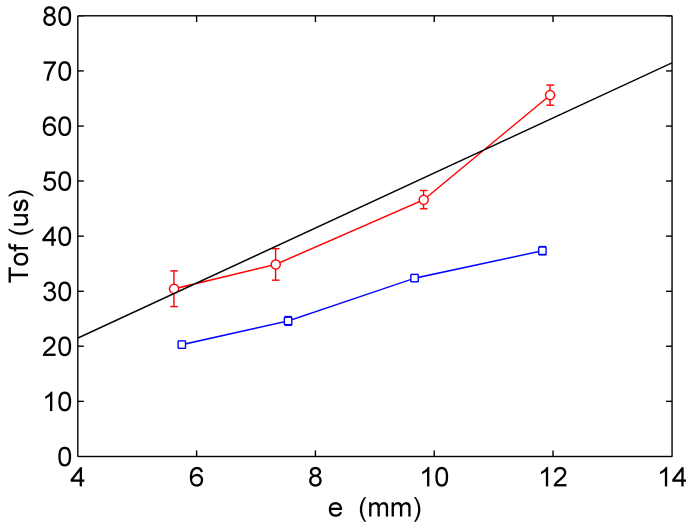

Figure 6.6: Time of flight (Tof) of the maximum of the envelope of transmitted pulses as a function of the sample thickness e (number of layers). Red circles are experimental results in the dry case and blue squares are experimental results in the wet case. The black line indicates the wave speed given by the EMT theory, see Eq. 6.1. Here, the input signal has a low amplitude.

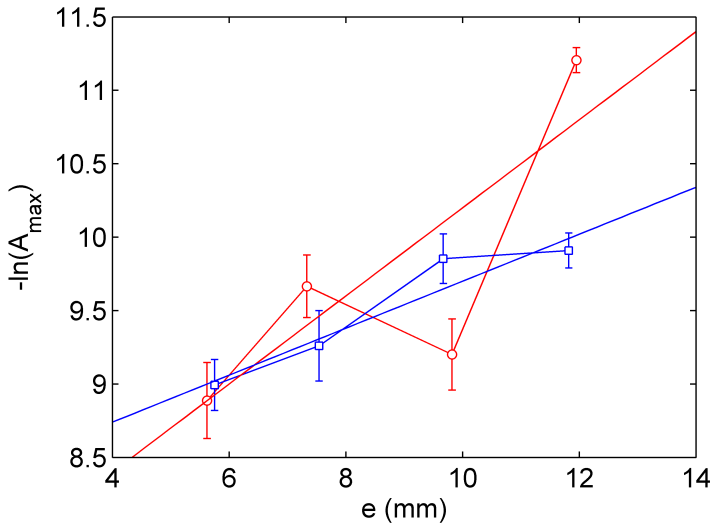

Figure 6.7: Maximum of the envelope of the transmitted pulses A_{max} as a function of the sample thickness e (number of layers). Red circles are experimental results in the dry case and blue squares are experimental results in the wet case. Here, the input signal has a low amplitude. The red and blue straight lines are best fits in the wet and dry cases, respectively.

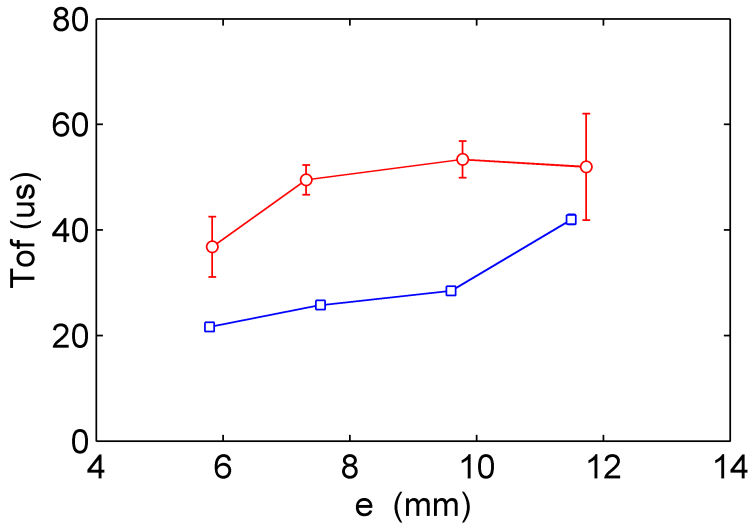

Figure 6.8: Time of flight (Tof) of the maximum of the envelope of transmitted pulses as a function of the sample thickness e (number of layers). Red circles are experimental results in the dry case and blue squares are experimental results in the wet case. Here, the input signal has a high amplitude.

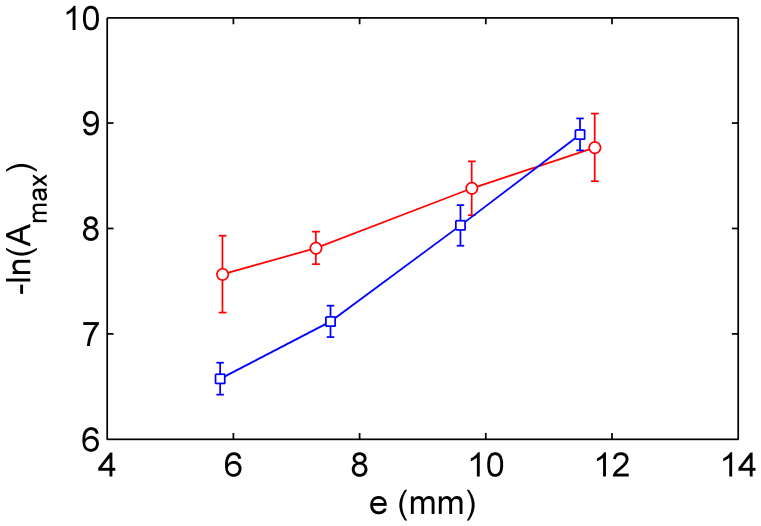

Figure 6.9: Maximum of the envelope of transmitted pulses A_{max} as a function of the sample thickness e (number of layers). The red circles are experimental results in the dry case and the blue squares are experimental results in the wet case. Here, the input signal has a high amplitude.

6.2.2 Probing granular media at high frequency

As to obtain an information on the attenuation length at higher frequencies, $\lambda \leq R_0$, we perform additional experiments. This second experimental procedure is such that the signal generated by an arbitrary wave generator (*Agilent 33500B*), is amplified by a high frequency power amplifier (*VectaWave VBA230-35*) and is finally transmitted to the emitting transducer, see the sketch in Fig. 6.3(b). The wave propagated through the granular media is then sensed by the receiving transducer and then amplified by a conditioner (Sofranel 5072PR), before being fed to the oscilloscope (Teledyne Lecroy HD0 4024). With the arbitrary waveform generator, one can drive the system with any type of signals. For this particular study we use a very long, 1 ms in duration, chirp covering a broad frequency range around 0.5 MHz, from 0.1 MHz to 0.9 MHz, see Fig. 6.10. The chirp is weighted by a hanning window. This very long signal is then post-processed as follows. One can estimate the cross correlation of the acquired voltage $V_{acq}(t)$ with the driving voltage reference $V_{ref}(t)$ sent by the arbitrary wave generator. This procedure provides a very short impulse response $x^{out}(t)$,

$$x^{out}(t) = V_{acq}(t) \otimes V_{ref}(-t), \tag{6.25}$$

where $\otimes$ denotes the convolution product. The result of the cross correlation of the driving voltage acquired by the oscilloscope $V_{acq}(t)$ with the reference voltage $V_{ref}(t)$ is shown in Fig. 6.10(c). The result of the cross correlation depends on the window used to weight the chirp, here a hanning window. Without windowing, Eq. 6.25 would have produced a delta Dirac function. When windowing the chirp, owing to the very long acquisition, one obtains a very well defined short pulse with a signal to noise ratio close to 100 dB. The hanning window is here used to adapt the spectrum of the driving voltage to the finite bandwidth of the frequency response of the transducers.

As in the original protocol, one pours particles of polyacetal (here from two to three layers) in the cylindrical container. We then compress/decompress the sample by putting/removing the top cylinder. This procedure is repeated several times until reaching the maximal achievable compacity. We then place the 2 kg mass on the top cylinder, in order to generate a confinement pressure of about $P \simeq 5$ kPa. The experimental protocol for the acquisition also remain unchanged: we acquire 8 realizations, which we then average. These acquisition (V_n) are then cross correlated with the reference signal $V_{ref}(t)$ provided by the arbitrary wave generator. According to the post-processing defied in Eq. 6.25, one finds

$$x_n^{out}(t) = < V_n(t) > \otimes V_{ref}(-t), \tag{6.26}$$

where $< \cdots >$ denotes the average of the 8 realizations and n is the number of layers, i.e. the thickness of the sample.

In Fig. 6.11, we plot the signals $x_2^{out}(t)$ and $x_3^{out}(t)$ as a function of time. One observes several additional pulses following the first pulse: these are due to multiple reflections at

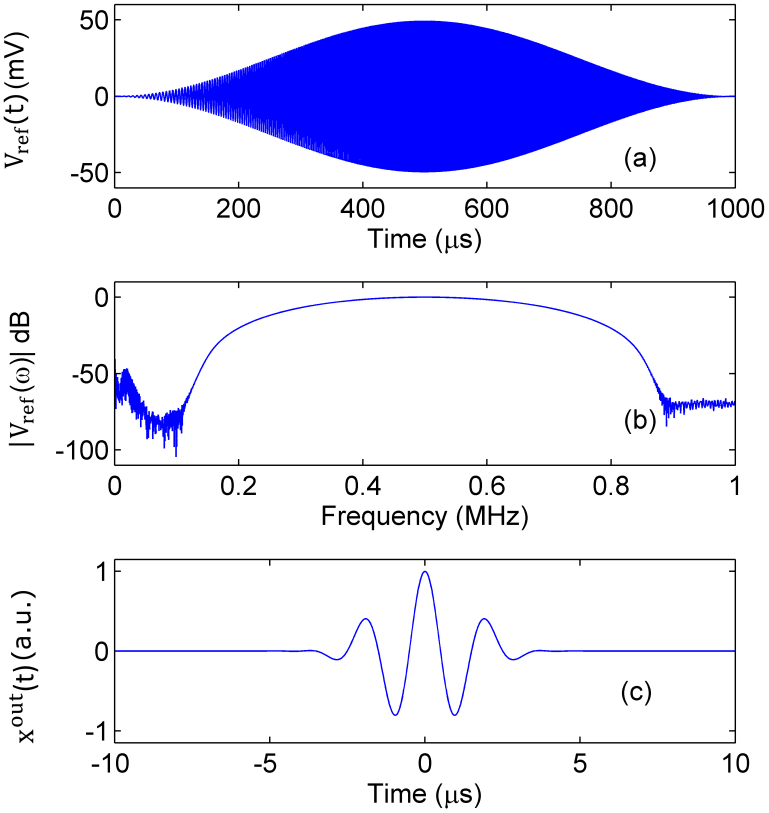

Figure 6.10: (a) Temporal representation of a signal generated by the arbitrary wave generator V_{ref} (Agilent 33500B). (b) Modulus of the Fourier transform of (a). (c) Cross-correlation $x^{out}(t)$ between the reference signal $V_{ref}(-t)$ and the signal transmitted through the sample $V_{acq}(t)$.

the boundaries of the sample. We then estimate the envelope of the signal by the Hilbert transform; the arrival time and the magnitude of the maximum of the envelope, x_2^m and x_3^m, serve for the estimation of the wave speed and the attenuation length. Here, we estimate c from the time of flight of the maximum of the envelope between x_2^m and x_3^m, while the ratio between x_2^m and x_3^m serves for the evaluation of the attenuation length $l_a = -\Delta e/ln(x_3^m/x_2^m)$, where $\Delta e = e_3 - e_2$ is the thickness difference between two and three layers of spheres. We estimate the wave speed at about $c_d \simeq 260$ ms^{-1} and the attenuation length at about $l_a \simeq 1.8$ mm.

In Fig. 6.12, we plot the Fourier transform of $x_2^{out}(t)$ and $x_3^{out}(t)$: we observe that the transmitted signals are centered around 0.5 MHz, in agreement with our requirement. Next, we analyze the wave transmitted through the wet granular medium. The results are plotted in Fig. 6.13 and in Fig. 6.14.

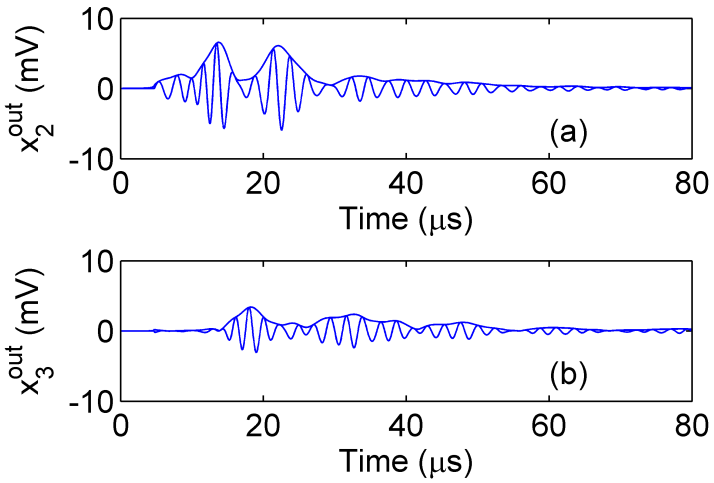

Figure 6.11: (a,b) Signals propagating through two x_2^{out} and three x_3^{out} layers of dry granular media, respectively.

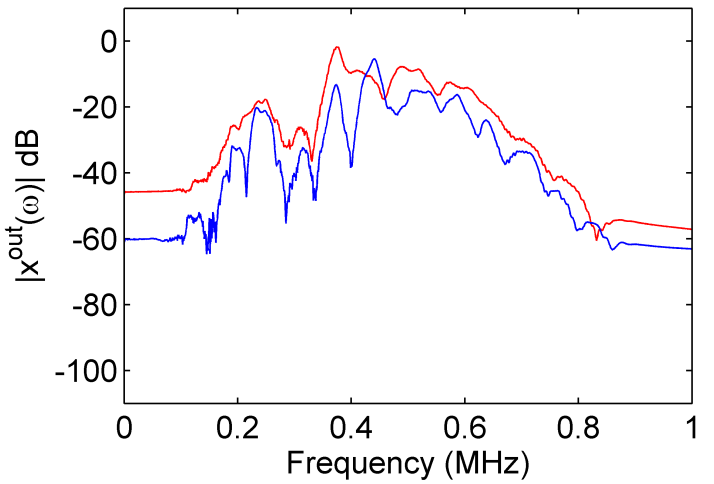

Figure 6.12: Fourier transform of the signals propagating through two x_2^{out} and three x_3^{out} layers of dry granular media, in red and in blue respectively.

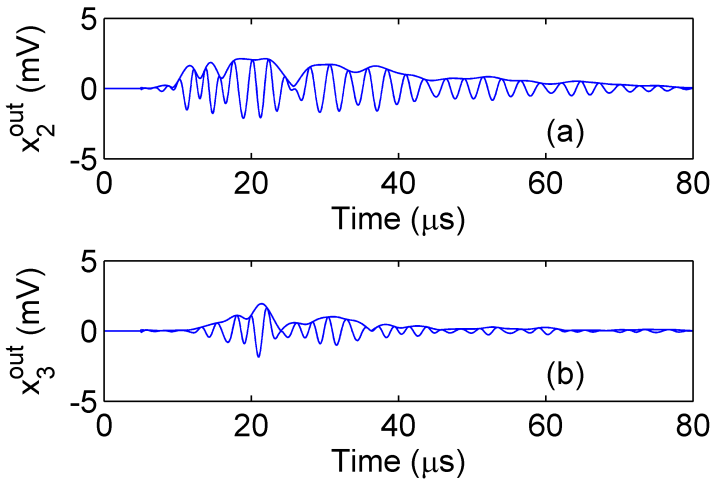

Figure 6.13: (a,b) Signals propagating through two x_2^{out} and three x_3^{out} layers of wet granular media, respectively. The signals are not filtered.

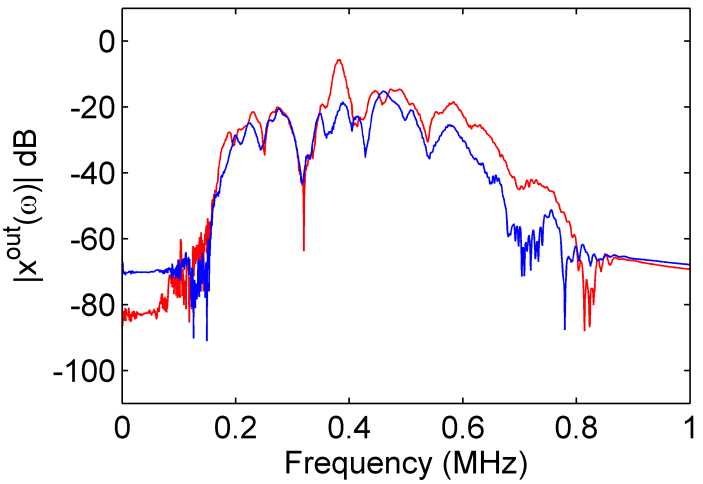

Figure 6.14: Fourier transform of the signals propagating through two x_2^{out} and three x_3^{out} layers of wet granular media, in red and blue respectively. The signals are not filtered.

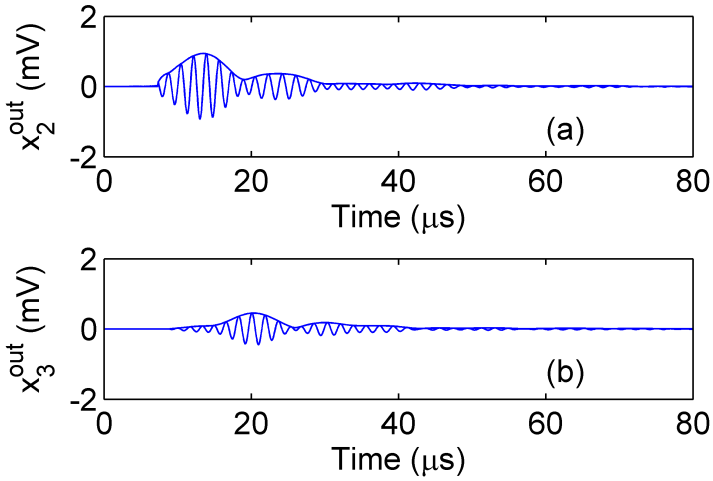

Figure 6.15: (a,b) Signals propagating through two x_2^{out} and three x_3^{out} layers of wet granular media, respectively. The signals are here filtered with a gaussian filter centered at 0.5 Mhz and with bandwidth equal to 0.15.

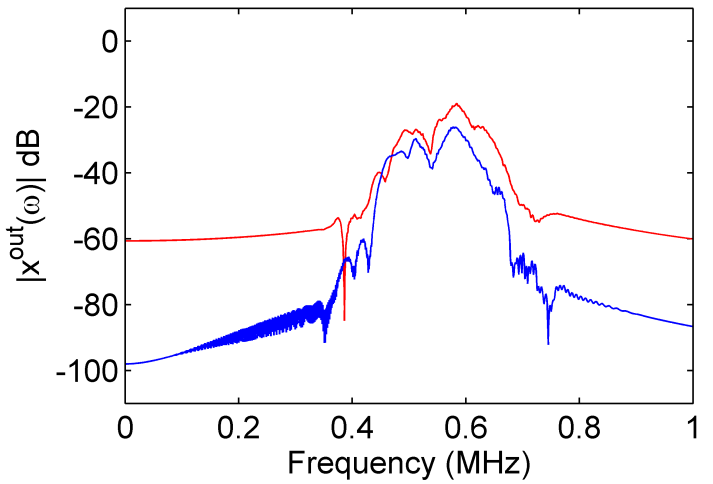

Figure 6.16: Fourier transform of the signals propagating through two x_2^{out} and three x_3^{out} layers of wet granular media, in red and blue respectively. The signals are here filtered with a gaussian filter centered at 0.5 Mhz and with a bandwidth equal to 0.15.

The lower magnitude of the transmitted signals, due to the slightly larger attenuation, make the signals more affected by spurious contributions; for sake of clarity, we clean these data by filtering out the frequency content with a gaussian filter centered on $f = 0.5$ MHz and bandwidth $bw = 0.15$. The filtered data are shown in Fig. 6.15 and in Fig. 6.16. As observed in this case, we estimate the wave speed to be $c_w \simeq 275$ ms^{-1}, while the attenuation length is found at $l_a \simeq 2.6$ mm. Applying the same gaussian filter to the dry case, we obtain $c_d \simeq 250$ ms^{-1} and $l_a \simeq 1.8$ mm.

6.3 Analysis of the experimental results

6.3.1 Analysis of low frequency experiments

First, we comment the experimental velocity at low frequency and low amplitude. The measured wave speed is $c_d \simeq 180$ ms^{-1} in the dry case and is compatible with the estimation of EMT, $V_p \simeq 200$ ms^{-1}, see the black line in Fig. 6.6, obtained from Eq. 6.1 with $Z = 6$, $\Phi = 0.64$, $P = 5$ kPa, $f = 30$ kHz and with the characteristics of polyacetal spheres. Additionally, the measured wave speed is $c_w \simeq 344$ ms^{-1} in the wet case, which also fairly agrees with the EMT estimation $V_w \simeq 340$ ms^{-1}, see Eq. 6.14. As for the dry case, we use $Z = 6$, $\Phi = 0.64$, $P = 5$ kPa, $f = 30$ kHz and $\mu = 5$ Pa.s.

It is worth mentioning that our estimations also fairly describe the experimental result obtained by Brunet [10] and Griffiths [107]. There the relative difference between wet and dry speed is about 10%, in both cases, for fluid with viscosity 20 mPas and confinement pressure $P \simeq 350$ kPa [10] and for fluid with viscosity 10 Pas and $P \simeq 1$ MPa [107]. In theirs experimental studies, Brunet and Griffiths used glass beads with Young's modulus $E_g = 70$ GPa, Poisson ratio $\nu_g = 0.25$ and density $\rho_g = 2450$ kg/m^3. Our estimation of the wave speed at frequency $f = 100$ kHz and with sphere radius $R_0 \simeq 400$ μm, in the dry case, see Eq. 6.1, and in the wet case, see Eq. 6.14, indicates that the relative difference would be 10% when using the parameters indicated by Brunet [10], while it would by 12% in the configuration probed by Griffiths [107].

Next, we focus on the experimental velocity obtained at low frequency and high amplitude. In this case, the measured wave speed $c_d \simeq 435$ ms^{-1} in the dry case does not provide a satisfactory agreement with the EMT estimation $V_p \simeq 200$ ms^{-1}: the measurement is more than twice the prediction. However, the curve of the time of flight versus thickness looks somehow awkward since it seems to tend to a plateau at large thickness: the data may lack precision and consistency here. Possible reasons may result from various nonlinearity at high amplitude and spurious contributions. The agreement is slightly better in the wet case, where the magnitude of the wave is lowered by the larger dissipation: we obtain $c_w \simeq 305$ ms^{-1} experimentally while it is $V_w \simeq 340$ ms^{-1} in theory.

Finally, we consider the estimations and the measurements of the attenuation length. At low frequency, the wavelength $\lambda = c/f$ is theoretically $\lambda_d \simeq 6.5$ mm in the dry case and $\lambda_d \simeq 11.3$ mm in the wet case: in all cases, the wavelength is larger than the size

of the spheres. We thus estimate the scattering attenuation length l_s from the Rayleigh approximation, see Eq. 6.20. In this case one obtains

$$l_s^{th} \simeq 12.5 \text{ mm}, \tag{6.27}$$
$$l_H^{th} \simeq 64 \text{ mm}, \tag{6.28}$$
$$l_{ehd}^{th} \simeq 11 \text{ mm}. \tag{6.29}$$

According to Eq. 6.22 and Eq. 6.23, the attenuation lengths in dry and wet cases are

$$l_d^{th} = 10.5 \text{ mm}, \tag{6.30}$$
$$l_w^{th} = 5.4 \text{ mm}. \tag{6.31}$$

Both the theoretical and the experimental data shows that the attenuation length is smaller in the wet case than in the dry case: this is consistent with an increase of the attenuation. In addition, the experimental data, $l_d \simeq 4.76$ mm and $l_w \simeq 2.33$ mm, have same order of magnitude as the estimations given by Eq. 6.30 and Eq. 6.31. Finally, by subtracting the attenuation of the dry configuration from attenuation of the wet case, see Eq. 6.24, one obtains $l_{ehd} = 1/(1/l_w - 1/l_d) \simeq 4.56$ mm: the theoretical estimation, Eq. 6.29, underestimates the measured attenuation by a approximately a factor two.

6.3.2 Analysis of high frequency experiments

In the high frequency regime, around $f = 0.5$ MHz, the theoretical wavelength is $\lambda_d \sim 0.4$ mm in the dry case and $\lambda_w \sim 0.7$ mm in the wet case: in both configurations, the wavelength is smaller than the size of the particles, $\lambda < R_0$. As a consequence, the long wavelength approximation is not fulfilled and the EMT is not reliable: the comparison with experimental velocity is pointless. However, extending the long wavelength estimations, $V_p \simeq 200$ ms^{-1} and $V_w \simeq 340$ ms^{-1}, we find again a fair agreement in the dry case, $c_d \simeq 250$ ms^{-1}, and a more cautious one in the wet case, $c_w \simeq 275$ ms^{-1}.

Concerning the attenuation lengths, we find theoretically

$$l_s^{th} \simeq 1 \text{ mm}, \tag{6.32}$$
$$l_H^{th} \simeq 4 \text{ mm}, \tag{6.33}$$
$$l_{ehd}^{th} \simeq 1 \text{ mm}. \tag{6.34}$$

where l_s^{th} is estimated from the geometrical limit of the scattering given by Eq. 6.21, according to the short wavelength approximation. From Eq. 6.22 and Eq. 6.23, the overall attenuation lengths in the dry case and in the wet cases are

$$l_d^{th} = 0.8 \text{ mm}, \tag{6.35}$$
$$l_w^{th} = 0.5 \text{ mm}. \tag{6.36}$$

In this frequency range, the attenuation due to the scattering becomes important: l_d^{th} and l_w^{th} have similar magnitudes. In contrary to the low frequency case, the estimations given by Eq. 6.35 and Eq. 6.36 here overestimates the experimental data, which are about $l_d \simeq 1.8$ mm and $l_w \simeq 2.6$ mm. However, the order of magnitude is correctly estimated.

6.4 Conclusions

In this chapter we presented a preliminary experimental study concerning ultrasonic wave propagation in dry and wet three-dimensional granular media. We measured both the wave speed and the attenuation length at low and high frequencies and at low and high amplitudes. Up to a certain extent, all our measurement provides somehow correct order of magnitudes but still lack precision and consistency in some cases.

In the dry case, the measured wave speed at low amplitude provides a satisfactory agreement with the theoretical estimation from the effective medium theory. In the wet case, the effective medium theory combined with an elastohydrodynamic description of the contact dynamics fairly reproduces the measured wave speed. As observed with signals at high amplitudes, the attenuation length provides a correct order of magnitude between theory and experiment.

We analyzed also the attenuation length for signals in a high frequency band, where the wavelength is equal to, if not smaller than, the size of the particles. Here, the theoretical estimations provide also a correct order of magnitude between theory and experiment. Our observations suggest that the attenuation at high frequency is dominated by the scattering.

Chapter 7

General conclusion and perpectives

This thesis dealt with wave propagation in dry and wet granular media, with the aim of relating the features at the microscopic scale of the grains and at the macroscopic scale of the acoustic wavelength. In a first place, we presented an experimental study devoted to probe how elastic waves propagate in laboratory scaled one-dimensional dry granular media. These media stand for an equivalent of the force chains, which are the quasi one-dimensional paths of strongest contacts in three-dimensional granular packing, along which elastic waves are known to propagate. Practically, our samples are alignments of centimetric spherical particles aligned on a support; these alignments were set under static compression. Our measurements and our analysis, based on the microscopic description of the dynamics of the grains, revealed the effect of an elastic coupling between the particles and an elasto-frictional on-site potential between the particles and the supports. The on-site potential induces a zero frequency band gap in the transfer function of the medium: the transmission of vibrations at low frequency is impeded. The model of such a local interplay via a tangential stiffness between the spheres and the cylindrical supports renders all the details of the measured dispersion relation.

In a second place, we dealt with wave propagation in wet one-dimensional granular media. Wet media were obtained by adding a small drop of viscous fluid at the contacts between every particle. Our observations demonstrated that wet particles interact via a complex elastohydrodynamic (EHD) mechanism, which relies on the ability of the interstitial fluid to elastically deform the particles. The EHD interplay confers remarkable and non-trivial features upon waves, such as a significant increase of the propagation speed compared to the dry case. We derived a model that quantitatively matches our observations on the wave speed, while the agreement of the attenuation was only qualitative.

In a third place, we checked the reliability of our analysis to depict wave propagation in real granular media, such as the wet sand. We performed preliminary ultrasonic wave

transmission experiments in dry and wet random close packing of millimetric particles. In the dry case, our results agree with a well-known effective medium theory (EMT) in the long wavelength approximation. The EMT model combined with an EHD mechanism fairly reproduces most of our experimental observations concerning wave speed and attenuation in wet media. As a whole, our achievements likely contribute to a better understanding of the mechanisms relying on wave propagation in dry and wet granular media.

As a perspective, more experimental and analytic studies should be undertaken to improve the estimation and the understanding of the attenuation in both one-dimensional and three-dimensional granular media, especially in the dry case. In granular alignments, the attenuation was directly correlated to the loss angle, which in turn, was quantified by the knowledge of the complex Young's modulus of the spheres. By performing experimental manipulation on the chain composed of the spheres with different bulk characteristic, one would gain a better insight in this mechanism.

In turn, in three-dimensional configurations, an additional mechanism of attenuation is due to the scattering of waves on every particles, quantified here by an independent scattering approximation. The independent scattering approximation holds for weak concentrations of scatters only. In perspective one could consider a more appropriate model to describe our experimental configuration.

Concerning the preliminary experiments performed in three-dimensional granular media, we only probed one value of viscosity and one confinement pressure; our observations are promising and analyzing the response of wet granular packing within a broader range of parameters would be necessary. Still, additional protocols to quantify the influence of the coordination number and the compacity on the wave speed and attenuation, both in dry and wet configurations would be of interest. The later could be done for instance by considering fluids with different surface tensions and over a broader range of confinement pressure.

Finally in the three dimensional media, the very last experiment have been performed at high frequency from the comparison between signals transmitted through two and three layers of particles only; considering thicker samples may also help reaching a better accuracy of the measurements. In any case, this will likely require larger excitation to overcome the very strong dissipation observed in both dry and wet configurations.

Bibliography

[1] H. M. Jaeger, S. R. Nagel, and R. P. Behringer, "The physics of granular materials," *Physics Today*, vol. 49, p. 32, 1996.

[2] Y. Forterre and O. Pouliquen, "Flows of dense granular media," *Annual Review of Fluid Mechanics*, vol. 40, p. 1, 2008.

[3] C. Liu and S. Nagel, "Sound in sand," *Physical Review Letters*, vol. 68, p. 2301, 1992.

[4] C. Liu and R. Sidnay, "Sound in a granular material: Disorder and nonlinearity," *Physical Review B*, vol. 48, p. 15646, 1993.

[5] C.-h. Liu, "Spatial patterns of sound propagation in sand," *Phys. Rev. B*, vol. 50, pp. 782–794, Jul 1994.

[6] X. Jia and B. Velicky, "Ultrasound propagation in externally stressed granular media," *Physical Review Letters*, vol. 82, p. 1863, 1999.

[7] G. Mavko, T. Mukerji, and J. Dvorkin, *The Rock Physics Handbook: Tools for Seismic Analysis of Porous Media*. Cambridge: Cambridge University Press, 2010.

[8] H. A. Makse, N. Gland, D. L. Johnson, and L. Schwartz, "Granular packings: Nonlinear elasticity, sound propagation, and collective relaxation dynamics," *Physical Review E*, vol. 70, p. 061302, 2004.

[9] D. Domenico, "Elastic properties of unconsolidated porous sand reservoirs," *Geophysics*, vol. 42, p. 1339, 1977.

[10] T. Brunet, *Etude de milieux granulaires secs et mouillés a l'aide des ondes ultrasonores*. PhD thesis, Université de Marne La Vallée, 2006.

[11] S. Job, F. Santibanez, F. Tapia, and F. Melo, "Nonlinear waves in dry and wet hertzian granular chains," *Ultrasonics*, vol. 48, p. 506, 2008.

[12] S. Job, F. Melo, A. Sokolow, and S. Sen, "How hertzian solitary waves interact with boundaries in a 1D granular medium," *Physical Review Letters*, vol. 94, p. 178002, 2005.

[13] F. Melo, S. Job, F. Santibanez, and F. Tapia, "Experimental evidence of shock mitigation in a hertzian tapered chain," *Physical Review E*, vol. 73, p. 041305, 2006.

[14] C. Daraio, V. F. Nesterenko, E. B. Herbold, and S. Jin, "Energy trapping and shock disintegration in a composite granular medium," *Physical Review Letters*, vol. 96, no. 5, p. 058002, 2006.

[15] S. Job, F. Santibanez, F. Tapia, and F. Melo, "Wave localization in strongly nonlinear hertzian chains with mass defect," *Physical Review E*, vol. 80, p. 025602, 2009.

[16] N. Boechler, G. Theocharis, S. Job, P. G. Kevrekidis, M. A. Porter, and C. Daraio, "Discrete breathers in one-dimensional diatomic granular crystals," *Physical Review Letters*, vol. 104, p. 244302, 2010.

[17] G. Theocharis, N. Boechler, P. G. Kevrekidis, S. Job, M. A. Porter, and C. Daraio, "Intrinsic energy localization through discrete gap breathers in one-dimensional diatomic granular crystals," *Physical Review E*, vol. 82, p. 056604, 2010.

[18] F. Li, L. Zhao, T. Z., L. Yu, and J. Yang, "Visualization of solitary waves via laser doppler vibrometry for heavy impurity identification in a granular chain," *Smart Materials and Structures*, vol. 22, p. 035016, 2013.

[19] J. Yang, M. Gonzalez, E. Kim, C. Agbasi, and M. Sutton, "Attenuation of solitary waves and localization of breathers in 1d granular crystals visualized via high speed photography," *Experimental Mechanics*, vol. 54, p. 1043, 2014.

[20] N. Boechler, G. Theocharis, and C. Daraio, "Bifurcation-based acoustic switching and rectification," *Nature Materials*, vol. 10, p. 665, 2011.

[21] C. M. Donahue, P. W. J. Anzel, L. Bonanomi, T. A. Keller, and C. Daraio, "Experimental realization of a nonlinear acoustic lens with a tunable focus," *Applied Physics Letters*, vol. 104, p. 014103, 2014.

[22] N. Boechler, J. Eliason, A. Kumar, A. Maznev, K. Nelson, and N. Fang, "Interaction of a contact resonance of microspheres with surface acoustic waves," *Physical Review Letters*, vol. 111, 2013.

[23] M. Hiraiwa, M. Abi Ghanem, S. Wallen, A. Khanolkar, A. A. Maznev, and N. Boechler, "Complex contact-based dynamics of microsphere monolayers revealed by resonant attenuation of surface acoustic waves." 2015 in press.

[24] J. K. Eliason, A. Vega-Flick, M. Hiraiwa, A. Khanolkar, T. Gan, N. Boechler, N. Fang, K. A. Nelson, and A. A. Maznev, "Resonant attenuation of surface acoustic waves by a microgranular metamaterial," *Applied Physics Letters*, vol. 061907, p. 108, 2016.

[25] S. Leroy, *Les forces de surface dynamiques pour l'investigation mécanique des surfaces molles.* PhD thesis, Université Claude Bernard Lyon I, 2010.

[26] S. Leroy and E. Charlaix, "Hydrodynamic interactions for the measurement of thin film elastic properties," *Journal of Fluid Mechanics*, vol. 674, p. 389, 2011.

[27] S. Leroy, A. Steinberger, C. Cottin-Bizonne, F. Restagno, L. Léger, and E. Charlaix, "Hydrodynamic interaction between a spherical particle and an elastic surface: A gentle probe for soft thin films," *Physical Review Letters*, vol. 108, p. 264501, 2012.

[28] R. Villey, *Nanorhéologie des liquides confinés : application á la nanomécanique des couches minces.* PhD thesis, UniversitéClaude Bernard Lyon I, 2013.

[29] P. A. Deymier, ed., *Acoustic Metamaterials and Phononic Crystals.* Berlin: Springer, 2013.

[30] E. Yablonovitch, "Inhibited spontaneous emission in solid-state physics and electronics," *Physical Review Letters*, vol. 58, p. 2059, 1987.

[31] T. Quang, M. Woldeyohannes, S. John, and G. S. Agarwal, "Coherent control of spontaneous emission near a photonic band edge: A single-atom optical memory device," *Physical Review Letters*, vol. 79, p. 5238, 1997.

[32] S. John, "Electromagnetic absorption in a disordered medium near a photon mobility edge," *Physical Review Letters*, vol. 53, p. 2169, 1984.

[33] S. John, "Strong localization of photons in certain disordered dielectric superlattices," *Physical Review Letters*, vol. 58, p. 2486, 1987.

[34] S. Y. Lin, J. G. Fleming, D. L. Hetherington, B. K. Smith, R. Biswas, K. M. Ho, M. M. Sigalas, W. Zubrzycki, S. R. Kurtz, and J. Bur, "A three-dimensional photonic crystal operating at infrared wavelengths," *Nature*, vol. 394, p. 251, 1998.

[35] R. Martinez-Sala, J. Sancho, J. V. Sanchez, V. Gomez, J. Llinares, and F. Meseguer, "Sound attenuation by sculpture," *Nature*, vol. 378, p. 241, 1995.

[36] Z. Liu, X. Zhang, Y. Mao, Y. Y. Zhu, Z. Yang, C. T. Chan, and P. Sheng, "Locally resonant sonic materials," *Science*, vol. 289, p. 1734, 2000.

[37] V. Narayanamurti, H. L. Stormer, M. A. Chin, A. C. Gossard, and W. Wiegmann, "Selective transmission of high-frequency phonons by a superlattice: The dielectric phonon filter," *Physical Review Letters*, vol. 43, p. 2012, 1979.

[38] M. Sigalas and E. Economou, "Band structure of elastic waves in two-dimensional systems," *Solid State Communications*, vol. 86, p. 141, 1993.

[39] M. Sigalas and E. Economou, "Elastic and acoustic wave band structure," *Journal of Sound and Vibration*, vol. 158, p. 377, 1992.

[40] F. R. Montero de Espinosa, E. Jiménez, and M. Torres, "Ultrasonic band gap in a periodic two-dimensional composite," *Physical Review Letters*, vol. 80, p. 1208, 1998.

[41] S. Benchabane, A. Khelif, J.-Y. Rauch, L. Robert, and V. Laude, "Evidence for complete surface wave band gap in a piezoelectric phononic crysta," *Physical Review E*, vol. 73, p. 065601, 2006.

[42] A. Khelif, P. A. Deymier, B. Djafari-Rouhani, J. O. Vasseur, and L. Dobrzynski, "Two-dimensional phononic crystal with tunable narrow pass band: Application to a waveguide with selective frequency," *Journal of Applied Physics*, vol. 94, p. 1308, 2003.

[43] R. M. Nedderman, *Statics and Kinematic of Granular materials*. Cambridge: Cambridge University Press, 1992.

[44] H. M. Jaeger, "Sand, jams and jets," *Physics World*, vol. 18, p. 34, 2005.

[45] J. Duran, *Sables, poudres et grains*. Paris: Eyrolles, 1997.

[46] P. Richard, M. Nicodemi, R. Delannay, P. Ribiére, and D. Bideau, "Slow relaxation and compaction of granular systems," *Nature Materials*, vol. 4, p. 121, 2005.

[47] B. Andreotti, Y. Forterre, and O. Pouliquen, *Les milieux granulaires*. Les Ulis: EDP Sciences, 2011.

[48] L. Mester, *The new physical-mechanical theory of granular materials*. Hungary: Homonnai Kiado, 2009.

[49] L. Landau and E. Lifshitz, *Theorie de l'elasticite*. Moscou: MIR, 1967.

[50] K. L. Johnson, *Contact Mechanics*. Cambridge: Cambridge University Press, 1985.

[51] V. L. Poppov, *Contact Mechanics and Friction*. Berlin: Springer, 2010.

[52] K. L. Johnson, K. Kendall, and A. D. Roberts, "Surface energy and the contact of elastic solids," in *Proceedings of the Royal Society of London. Series A, Mathematical and Physical*, 1971.

[53] B. V. Derjaguin, V. Muller, and Y. P. Toporov, "Effect of contact deformations on the adhesion of particles," *Journal of Colloid and Interface Science*, vol. 53, p. 314, 1975.

[54] D. Tabor, "Surface forces and surface interactions," *Journal of Colloid and Interface Science*, vol. 58, p. 2, 1977.

[55] G. Barnocky and R. H. Davis, "Elastohydrodynamic collision and rebound of spheres: Experimental verification," *Physics of Fluids*, vol. 31, p. 1324, 1988.

[56] R. H. Davis, A. Rager, and B. Good, "Elastohydrodynamic rebound of spheres from coated surfaces," *Journal of Fluid Mechanics*, vol. 468, p. 107, 2002.

[57] A. M. Ardekani, D. D. Joseph, D. Dunn-Rankin, and R. H. Rangel, "Particle-wall collision in a viscoelastic fluid," *Journal of Fluid Mechanics*, vol. 633, p. 475, 2009.

[58] G. Joseph and M. L. Hunt, "Oblique particle-wall collisions in a liquid," *Journal of Fluid Mechanics*, vol. 510, p. 71, 2004.

[59] F.-L. Yang and M. L. Hunt, "Dynamics of particle-particle collisions in a viscous liquid," *Physics of Fluids*, vol. 18, p. 121506, 2006.

[60] C. M. Donahue, C. M. Hrenya, and R. H. Davis, "Stokes cradle: Newton cradle with liquid coating," *Physical Review Letters*, vol. 105, p. 034501, 2010.

[61] C. M. Donahue, C. M. Hrenya, R. H. Davis, K. J. Nakagawa, A. P. Zelinskaya, and G. G. Joseph, "Stokes cradle: normal three-body collisions between wetted particles," *Journal of Fluid Mechanics*, vol. 650, p. 479, 2010.

[62] C. M. Donahue, C. M. Hrenya, R. H. Davis, K. J. Nakagawa, A. P. Zelinskaya, and G. G. Joseph, "Stokes cradle: Normal three-body collisions between wetted particles," *Journal of Fluid Mechanics*, vol. 650, p. 479, 2010.

[63] J. S. Marshall, "Viscous damping force during head-on collision of two spherical particles," *Physics of fluids*, vol. 23, p. 013305, 2011.

[64] J. Uddin, J. O. Marston, and S. T. Thoroddsen, "Squeeze flow of a carreau fluid during sphere impact," *Physics of Fluids*, vol. 24, p. 073104, 2012.

[65] R. H. Davis, J. M. Serayssol, and E. Hinch, "The elastohydrodynamic collision of two spheres," *Journal of Fluid Mechanics*, vol. 163, p. 479, 1986.

[66] B. Hamrock, *Fundamentals of Fluid Film Lubrification*. New York: McGraw-Hill, 1994.

[67] M. Mani, A. Gopinath, and L. Mahadevan, "How things get stuck: Kinetics, elastohydrodynamics, and soft adhesion," *Physical Review Letters*, vol. 108, p. 226104, 2012.

[68] U. Landman, W. D. Luedtke, and J. Gao, "Atomic-scale issues in tribology: Interfacial junctions and nano-elastohydrodynamics," *Langmuir*, vol. 12, p. 4514, 1996.

[69] N. Fillot, T. Doki-Thonon, and W. Habchi, "The full-system approach for elastohydrodynamic lubrication," in *Excerpt from the Proceedings of the COMSOL Conference 2009 Milan*, 2009.

[70] J. M. Skotheim and L. Mahadevan, "Soft lubrication: The elastohydrodynamics of nonconforming and conforming contacts," *Physics of Fluids*, vol. 17, p. 092101, 2005.

[71] G. Barnocky and R. H. Davis, "The influence of pressure-dependent density and viscosity on the elastohydrodynamic collision and rebound of two spheres," *Journal of Fluid Mechanics*, vol. 209, p. 501, 1989.

[72] O. Vinogradova and F. Feuillebois, "Interaction of elastic bodies via surface forces. 1. power-law attraction," *Langmuir*, vol. 18, p. 5126, 2002.

[73] B. O. Jacobson, *Rheology and Elastohydrodynamic Lubrications*. New York: Elsevier, 1991.

[74] E. E. Brodsky and H. Kanamori, "Elastohydrodynamic lubrication of faults," *Papers on Seismology*, vol. 106, p. 16357, 2001.

[75] E. Charlaix and J. Crassous, "Adhesion forces between wetted solid surfaces," *The Journal of Chemical Physics*, vol. 122, p. 184701, 2005.

[76] A. Steinberger, C. Cottin-Bizonne, P. Kleimann, and E. Charlaix, "Nanoscale flow on a bubble mattress: Effect of surface elasticity," *Physical Review Letters*, vol. 100, p. 134501, 2008.

[77] M. C. Audry, S. Ramos, and E. Charlaix, "Adhesion between highly rough alumina surfaces: An atomic force microscope study," *Journal of Colloid and Interface Science*, vol. 331, p. 371, 2009.

[78] L. Bocquet and E. Charlaix, "Nanofluidics, from bulk to interfaces," *Chemical Society Reviews*, vol. 39, p. 1073, 2010.

[79] C. Cottin-Bizonne, A. Steinberger, B. Cross, O. Raccurt, and E. Charlaix, "Nanohydrodynamics: The intrinsic flow boundary condition on smooth surfaces," *Langmuir*, vol. 24, p. 1165, 2008.

[80] J. Crassous, M. Ciccotti, and E. Charlaix, "Capillary force between wetted nanometric contacts and its application to atomic force microscopy," *Langmuir*, vol. 27, p. 3468, 2011.

[81] R. Villey, E. Martinot, C. Cottin-Bizonne, M. Phaner-Goutorbe, L. Léger, F. Restagno, and E. Charlaix, "Effect of surface elasticity on the rheology of nanometric liquids," *Physical Review Letters*, vol. 111, p. 215701, 2013.

[82] R. Villey, A. Piednoir, P. Sharma, C. Cottin-Bizonne, B. Cross, M. Phaner-Goutorbe, and E. Charlaix, "Capacitive detection of buried interfaces by a dynamic surface force apparatus," *Review of Scientific Instruments*, vol. 84, no. 8, 2013.

[83] D. Mueth, H. Jaeger, and S. Nagel, "Force distribution in a granular medium," *Physical Review E*, vol. 57, p. 3167, 1998.

[84] R. B. Heywood, *Designing by Photoelasticity*. London: Chapman and Hall Ltd., 1952.

[85] R. Holt, "Lecture notes," 2004.

[86] D. Giancoli, *Physique générale: Ondes, optique et physique moderne.* Montreal: Centre Educative et Culturel inc., 1993.

[87] D. Howell and R. P. Behringer, "Stress fluctuations in a 2D granular couette experiment: A continuous transition," *Physical Review Letters*, vol. 82, p. 5241, 1999.

[88] F. Radjai, M. Jean, J. Moreau, and S. Roux, "Force distributions in dense two-dimensional granular systems," *Physical Review Letters*, vol. 77, p. 274, 1996.

[89] J. Geng, D. Howell, E. Longhi, and R. P. Behringer, "Footprints in sand: The response of a granular material to local perturbations," *Physical Review Letters*, vol. 87, p. 035506, 2001.

[90] V. Tournat and V. E. Gusev, "Nonlinear effects for coda-type elastic waves in stressed granular media," *Physical Review E*, vol. 80, p. 011306, 2009.

[91] X. Jia, T. Brunet, and J. Laurent, "Elastic weakening of a dense granular pack by acoustic fluidization: Slipping, compaction, and aging," *Physical Review E*, vol. 84, p. 020301, 2011.

[92] S. Kiesgen de Richter, V. Zaitsev, P. Richard, R. Delannay, G. Le Caer, and V. Tournat, "Experimental evidence of ageing and slow restoration of the weak-contact configuration in tilted 3D granular packings," *Journal of Statistical Mechanics*, vol. 2010, p. 11023, 2010.

[93] D. Espindola, B. Galaz, and F. Melo, "Ultrasound induces aging in granular materials," *Physical Review Letters*, vol. 109, p. 158301, 2012.

[94] C. Inserra, V. Tournat, and V. Gusev, "Characterization of granular compaction by nonlinear acoustic resonance method," *Applied Physics Letters*, vol. 92, p. 191916, 2008.

[95] V. F. Nesterenko, *Dynamics of Heterogenous Materials.* New York: Springer, 2001.

[96] C. Coste and B. Gilles, "On the validity of hertz contact law for granular material acoustics," *The European Physical Journal B*, vol. 7, p. 155, 1999.

[97] P. G. de Gennes, "Static compression of a granular medium: the soft shell model," *Europhysics Letters*, vol. 35, p. 145, 1996.

[98] J. Goddard, "Nonlinear elasticity and pressure-dependent wave speeds in granular media," in *Proceedings of the Royal Society of London. Series A, Mathematical and Physic*, 1990.

[99] P. G. de Gennes, "Lectures of the college de france held at ecole centrale de lyon 1997.".

[100] C. Coste, E. Falcon, and S. Fauve, "Solitary waves in a chain of beads under hertz contact," *Phys. Rev. E*, vol. 56, p. 6104, 1997.

[101] J. Duffy and R. D. Mindlin, "Stress-strain relations and vibrations of a granular medium," *Journal of Applied Mechanics*, vol. 24, p. 585, 1957.

[102] P. J. Digby, "The effective elastic moduli of porous granular rocks," *Journal of Applied Mechanics*, vol. 48, p. 803, 1981.

[103] K. Walton, "The effective elastic moduli of a random packing of spheres," *Journal of the Mechanics and Physics of Solids*, vol. 35, p. 213, 1987.

[104] A. Norris and D. L. Johnson, "Nonlinear elasticity of granular media," *Journal of Applied Mechanics*, vol. 64, p. 39, 1997.

[105] W. K. Winkler, "Contact stiffness in granular porous materials: Comparison between theory and experiment," *Geophysical Research Letters*, vol. 10, p. 1073, 1983.

[106] C. S. O'Hern, L. E. Silbert, A. J. Liu, and S. R. Nagel, "Jamming at zero temperature and zero applied stress: The epitome of disorder," *Phys. Rev. E*, vol. 68, p. 011306, Jul 2003.

[107] S. Griffiths, A. Rescaglio, and F. Melo, "Ultrasound propagation in wet and airless non-consolidated granular materials," *Ultrasonics*, vol. 50, p. 139, 2009.

[108] X. Jia, "Codalike multiple scattering of elastic waves in dense granular media," *Physical Review Letters*, vol. 93, p. 154303, 2004.

[109] J. S. Bendat, *Random Data,*. Hoboken: Wiley-Interscience, 1986.

[110] F. J. Fahy, *Sound and Structural Vibration: Radiation, Transmission and Response*. San Diego: Academic Press Inc, 1987.

[111] Blustar Silicon, *Rhodorsil Oils 47 Technical information*.

[112] A. Tourin, *Diffusion multiple et renversement du temps des ondes ultrasonores*. PhD thesis, Universite Paris VII, 1999.

[113] P. Sheng, *Wave Scattering, Localization, and Mesoscopic Phenomena*. Berlin: Springer, 2006.

[114] A. Lagendijka and B. A. van Tiggelen, "Resonant multiple scattering of light," *Physics Reports*, vol. 270, p. 143, 1996.

université PARIS-SACLAY
ÉCOLE DOCTORALE
Sciences mécaniques et énergétiques, matériaux et géosciences (SMEMAG)

Title : Waves in granular media: from microscopic scale to macroscopic scale

Keywords : Granular media, acoustic waves, fluid, rheology, contact dynamics

Abstract: This thesis deals with the study of mechanical wave propagation in dry or wet granular media, with the aim of relating the phenomena at the microscopic scale (particles dynamics, interaction potentials between grains, rheology of the interstitial fluid) to the features at the macroscopic scale (dispersion relation, wave speed and attenuation in the long wavelength approximation). The systems under study are either large one-dimensional granular media, as the analogs of the paths of the most compressed grains (the force chains) in real granular packings, or the real granular media themselves. In a first place, we study experimentally the wave transmission through alignments of dry centimetric spheres, which we model via the Hertz potential. We show that the elasto-frictional coupling between the grains and a substrate (the spheres' support) induces an on-site elastic potential, which in turn induces a band gap at zero frequency in the transfer function. In a second place, we show that the presence of an infinitesimal amount of viscous fluid at the contact between every particle induces an elasto-hydrodynamic (EHD) interaction. The later affects the attenuation of waves in addition to a significant increase of the wave speed, which in this case both non-trivially depend on the elasticity of the particles, on the viscosity of the fluid and on the frequency. In a third place, we check the reliability of our analysis to describe ultrasonic wave propagation in real granular materials such as dry or wet sand; our particles are here millimetric spheres. In the dry configuration, our results are consistent with an effective medium theory (EMT) which relies on the Hertz-Mindlin interaction in the long wavelength approximation. In the wet configuration, the EMT model combined with an EHD mechanism fairly reproduces our preliminary observations.

Titre : Ondes dans les milieux granulaires : de l'échelle microscopique à l'échelle macroscopique

Mots clés : Milieux granulaires, ondes acoustiques, fluide, rhéologie, dynamique du contact

Résumé : Cette thèse porte sur l'étude de la propagation d'ondes mécaniques dans des milieux granulaires secs ou mouillés, avec pour objectif de relier les phénomènes de l'échelle microscopique (dynamique des grains, potentiels d'interactions entre particules, rhéologie du fluide interstitiel) aux propriétés de l'échelle macroscopique (relation de dispersion, vitesse et atténuation des ondes dans l'approximation des grandes longueurs d'ondes). Les systèmes étudiés sont soit des milieux granulaires unidimensionnels de grande taille, analogues des chemins de plus forts contacts entre particules (les chaînes de force) dans les empilements de grains réels, soit les milieux granulaires réels eux-mêmes. Dans un premier temps, nous étudions expérimentalement la transmission d'ondes au travers d'un alignement de sphères centimétriques sèches, que nous modélisons via le potentiel de Hertz. Nous montrons que le couplage élasto-frictionnel entre les grains et un substrat (le support des sphères) engendre un potentiel élastique local, qui induit à son tour une bande interdite a fréquence nulle dans la fonction de transfert. Dans un deuxième temps, nous montrons que la présence d'une quantité infime de fluide visqueux au contact entre chaque particule induit une interaction élasto-hydrodynamique (EHD). Ce dernier induit une modification de l'atténuation des ondes et une augmentation très significative de la vitesse de propagation, qui dans ce cas dépendent de manière non-triviale de l'élasticité des particules, de la viscosité du fluide et de la fréquence. Dans un troisième temps, nous vérifions la fiabilité de notre analyse pour décrire la propagation d'ondes ultrasonores dans des milieux granulaires réels, tel que le sable mouillé ou non ; les particules sont ici des sphères millimétriques. Dans le cas sec, nos résultats sont en accord avec un modèle connu de milieux effectifs (EMT) qui relève de l'interaction de Hertz-Mindlin dans l'approximation des grandes longueurs d'ondes. Dans le cas mouille, le modèle EMT combiné à un mécanisme EHD reproduit de manière acceptable nos observations préliminaires.

Université Paris-Saclay
Espace Technologique / Immeuble Discovery
Route de l'Orme aux Merisiers RD 128 / 91190 Saint-Aubin, France